American Mineralogist, Volume 103, pages 1362–1400, 2018

Questioning the biogenicity of Neoproterozoic superheavy pyrite by SIMS

Huan Cui[1,2,*,†], Kouki Kitajima[1,2], Michael J. Spicuzza[1,2], John H. Fournelle[1], Adam Denny[2], Akizumi Ishida[1,2,3], Feifei Zhang[4], and John W. Valley[1,2]

[1]NASA Astrobiology Institute, University of Wisconsin, Madison, Wisconsin 53706, U.S.A.
[2]Department of Geoscience, University of Wisconsin, Madison, Wisconsin 53706, U.S.A.
[3]Department of Earth Science, Tohoku University, Sendai, Miyagi Prefecture 980-8577, Japan
[4]School of Earth and Space Exploration, Arizona State University, Tempe, Arizona 85287, U.S.A.

Abstract

The Neoproterozoic sulfur isotope ($\delta^{34}S$) record is characterized by anomalously high $\delta^{34}S_{pyrite}$ values. Many $\delta^{34}S_{pyrite}$ values are higher than the contemporaneous $\delta^{34}S_{sulfate}$ (i.e., $\delta^{34}S_{pyrite} > \delta^{34}S_{sulfate}$), showing reversed fractionation. This phenomenon has been reported from the Neoproterozoic post-glacial strata globally and is called "Neoproterozoic superheavy pyrite." The commonly assumed biogenic genesis of superheavy pyrite conflicts with current understanding of the marine sulfur cycle. Various models have been proposed to interpret this phenomenon, including extremely low concentrations of sulfate in seawaters or pore waters, or the existence of a geographically isolated and geochemically stratified ocean. Implicit and fundamental in all these published models is the assumption of a biogenic origin for pyrite genesis, which hypothesizes that the superheavy pyrite is syngenetic (in the water column) or early diagenetic (in shallow marine sediments) in origin and formed via microbial sulfate reduction (MSR). In this study, the Cryogenian Datangpo Formation in South China, which preserves some of the highest $\delta^{34}S_{pyrite}$ values up to +70‰, is studied by secondary ion mass spectrometry (SIMS) at unprecedented spatial resolutions (2 μm). Based on textures and the new sulfur isotope results, we propose that the Datangpo superheavy pyrite formed via thermochemical sulfate reduction (TSR) in hydrothermal fluids during late burial diagenesis and, therefore, lacks a biogeochemical connection to the Neoproterozoic sulfur cycle. Our study demonstrates that SEM-SIMS is an effective approach to assess the genesis of sedimentary pyrite using combined SEM petrography and micrometer-scale $\delta^{34}S$ measurements by SIMS. The possibility that pervasive TSR has overprinted the primary $\delta^{34}S_{pyrite}$ signals during late diagenesis in other localities may necessitate the reappraisal of some of the $\delta^{34}S_{pyrite}$ profiles associated with superheavy pyrite throughout Earth's history.

Keywords: Microbial sulfate reduction (MSR), thermochemical sulfate reduction (TSR), secondary ion mass spectrometry (SIMS), scanning electron microscopy (SEM), sulfur isotopes, framboidal pyrite; Isotopes, Minerals, and Petrology: Honoring John Valley

Introduction

The Neoproterozoic Era (1000–541 Ma) marks a transitional period in Earth's history that is characterized by a considerable rise in atmospheric oxygen, a gradual transformation in ocean redox conditions, and the rise of animal life (Halverson and Shields-Zhou 2011; Narbonne et al. 2012; Shields-Zhou et al. 2012; Xiao 2014). Notably, the Cryogenian Period (ca. 720–635 Ma) witnessed two episodes of global-scale low-latitude glaciation: the Sturtian glaciation (717–660 Ma) and the Marinoan glaciation (>639–635 Ma) (Hoffman et al. 1998, 2017; Rooney et al. 2015). These glaciations have been widely regarded as among the most profound ice ages in Earth's history. Sedimentological and paleomagnetic studies suggest that glaciers during the Cryogenian glaciations may have approached the equatorial latitudes, forming a "Snowball Earth" (Kirschvink 1992; Hoffman et al. 1998; Hoffman and Schrag 2002). Although the Neoproterozoic fossil record shows an Ediacaran (635–541 Ma) emergence of early animal life (Xiao et al. 2016), molecular clock studies suggest that the origin of the animal phyla may have occurred in early Neoproterozoic (Runnegar 1982; Peterson et al. 2004). Therefore, a precise biogeochemical reconstruction of the Neoproterozoic Era is critical to understanding the environmental context of early animal life evolution.

A remarkable feature of the Neoproterozoic chemostratigraphy is the anomalously high pyrite sulfur isotope ($\delta^{34}S_{pyrite}$) values, many of which are higher than the inferred contemporaneous seawater $\delta^{34}S_{sulfate}$ values (i.e., $\delta^{34}S_{pyrite} > \delta^{34}S_{sulfate}$) that are reconstructed from coexisting sulfate phases (e.g., anhydrite, carbonate-associated sulfate) (Fig. 1; Appendix[1] 1). These pyrites are commonly known as "superheavy pyrite" (Liu et al. 2006; Ries et al. 2009; Fike et al. 2015). The biogeochemical origin and palaeoenvironmental implications of the Neoproterozoic superheavy pyrite have puzzled geochemists for decades (Hayes et al. 1992; Fike et al. 2015). In marine sulfur cycles, $\delta^{34}S_{pyrite}$ signals can never be higher than coexisting $\delta^{34}S_{sulfate}$ signals (Canfield 2001a; Böttcher 2011; Canfield and Farquhar 2012), therefore the occurrence of superheavy pyrite challenges the canonical

* Present address: Earth System Science (ESS) & Analytical, Environmental and Geo-Chemistry (AMGC), Vrije Universiteit Brussel (VUB), Brussels, Belgium. Email: Huan.Cui@wisc.edu, Huan.Cui@vub.ac.be
† Special collection papers can be found online at http://www.minsocam.org/MSA/AmMin/special-collections.html.

0003-004X/18/0009–1362$05.00/DOI: http://doi.org/10.2138/am-2018-6489

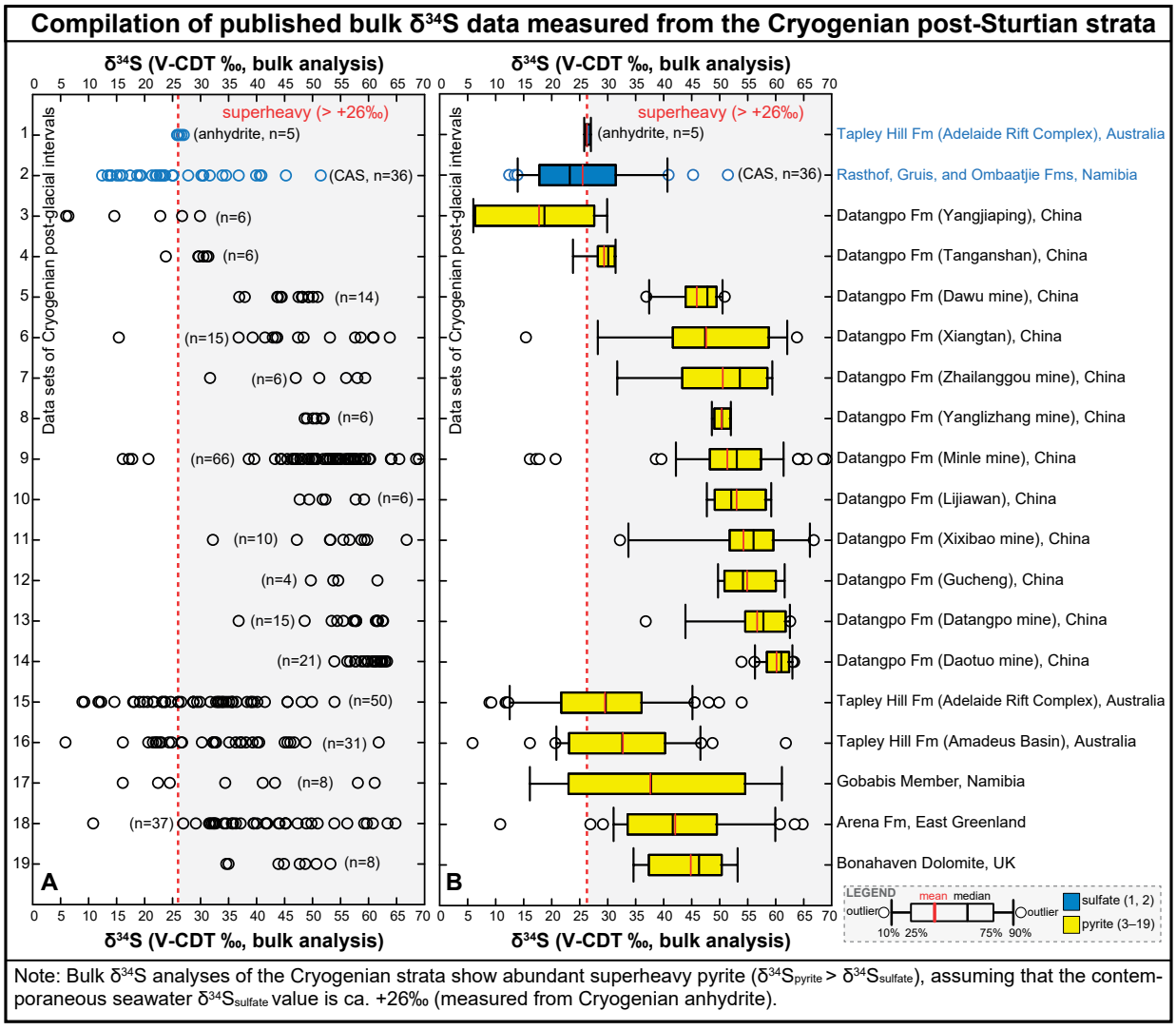

FIGURE 1. Compilation of published $\delta^{34}S$ data measured from the Cryogenian post-glacial strata in China, U.K., Namibia, and Australia. X -axis represents $\delta^{34}S$ values (V-CDT, ‰). Y-axis represents different published data sets. (**a**) Individual data points of all the data sets. Numbers in parentheses representing the amount of data. (**b**) Box plots of corresponding data in **a**. Red line and black line within each box showing the mean value and the median value, respectively. Data sets 1 and 2 (blue) representing $\delta^{34}S_{sulfate}$ data measured from anhydrite and carbonate-associated sulfate (CAS), respectively. Data sets 3–19 (yellow in **b**) representing $\delta^{34}S_{pyrite}$ data. Red dash line represents Cryogenian seawater $\delta^{34}S_{sulfate}$ values based on data set 1. All plotted data were generated by conventional bulk analysis. Note that many $\delta^{34}S_{pyrite}$ data (up to +70‰) are much higher than the contemporaneous $\delta^{34}S_{sulfate}$ value (ca. +26‰, red dash line), commonly known as superheavy pyrite signals (i.e., $\delta^{34}S_{pyrite} > \delta^{34}S_{sulfate}$). Data source: (1) Tapley Hill Formation (Adelaide Rift Complex), Australia (Gorjan et al. 2000); (2) Rasthof, Gruis, and Ombaatjie formations of the Otavi Group, Namibia (Hurtgen et al. 2002); (3–14) Datangpo Formation in South China, including localities at (3) Yangjiaping, Hunan Province (Li et al. 2012), (4) Tanganshan, Hunan Province (Liu et al. 2006), (5) Dawu mine, Songtao County, Guizhou Province (Zhou et al. 2007; Wu et al. 2016), (6) Xiangtan, Hunan Province (Li et al. 1999a; Liu et al. 2006), (7) Zhailanggou mine, Songtao County, Guizhou Province (Chen et al. 2008), (8) Yanglizhang mine, Songtao County, Guizhou Province (Zhou et al. 2007), (9) Minle mine, Huayuan County, Hunan Province (Tang 1990; Li et al. 1999a; Tang and Liu 1999; Feng et al. 2010; Li et al. 2012; Wu et al. 2016), (10) Lijiawan, Songtao County, Guizhou Province (Wang et al. 2016), (11) Xixibao mine, Songtao County, Guizhou Province (Zhang et al. 2013; Wang et al. 2016), (12) Gucheng, Hubei Province (Wu et al. 2016), (13) Datangpo mine, Songtao County, Guizhou Province (Li et al. 1999a; Zhou et al. 2007; Wu et al. 2016), (14) Daotuo mine, Songtao County, Guizhou Province (Zhu et al. 2013; Wang et al. 2016); (15) Tapley Hill Formation in the Adelaide Rift Complex, Australia (Gorjan et al. 2000); (16) Tapley Hill Formation in the Amadeus Basin, Australia (Gorjan et al. 2000); (17) Gobabis Member, Namibia (Gorjan et al. 2003); (18) Arena Formation, East Greenland (Scheller et al. 2018); (19) Bonahaven Dolomite Formation, U.K. (Parnell and Boyce 2017). All the compiled data are available in the online Appendix[1] 1.

understanding of the sulfur isotope systems.

Multiple studies have reported anomalously high $\delta^{34}S$ values in the Cryogenian Period (Fig. 1; Appendix[1] 1), including the Datangpo Formation in South China (Wu et al. 2016 and references therein), the Tapley Hill Formation in Australia (Hayes et al. 1992; Gorjan et al. 2000), the Court and Rasthof formations in Namibia (Hurtgen et al. 2002; Gorjan et al. 2003), the Bonahaven Dolomite Formation in Scotland (Parnell and Boyce 2017), and the Arena Formation in East Greenland (Scheller et al. 2018). Notably, reported superheavy pyrites in these formations all overlie the Sturtian glacial diamictite, leading to the speculation of a potential linkage between the superheavy pyrite and the Sturtian glaciation (Gorjan et al. 2000; Hurtgen et al. 2002).

Largely based on the post-glacial occurrence of the superheavy pyrites, a tantalizing hypothesis links the genesis of superheavy pyrite to a Snowball Earth glaciation (Gorjan et al. 2000; Hurtgen et al. 2002). In this scenario, the ocean during the Sturtian glaciation was covered with a thick ice sheet, therefore terrestrial sulfate input by riverine fluxes was significantly reduced or shut off. Continuous pyrite burial via microbial sulfate reduction (MSR) in the subglacial ocean drove seawater $\delta^{34}S_{sulfate}$ to extremely high values. During deglaciation, the high-$\delta^{34}S_{sulfate}$ water mass generated and maintained during the Snowball Earth upwelled onto continental shelf environments, causing the precipitation of superheavy pyrite in post-glacial successions at a global scale.

The above hypothesis is attractive in that it links the genesis of superheavy pyrites to the Sturtian glaciation. If correct, then extremely high seawater $\delta^{34}S_{sulfate}$ values hypothesized in the terminal Sturtian oceans are expected to be reflected in syngenetic or early authigenic pyrite in diamictite intervals assuming a certain fractionation between $\delta^{34}S_{sulfate}$ and $\delta^{34}S_{sulfide}$. Insofar as pyrite authigenesis could represent a broad spectrum of conditions from syndepositional to postdepositional, pyrites can be remarkably zoned or heterogeneous. Therefore, conventional greater than millimeter-scale $\delta^{34}S_{pyrite}$ analysis of mineral concen-

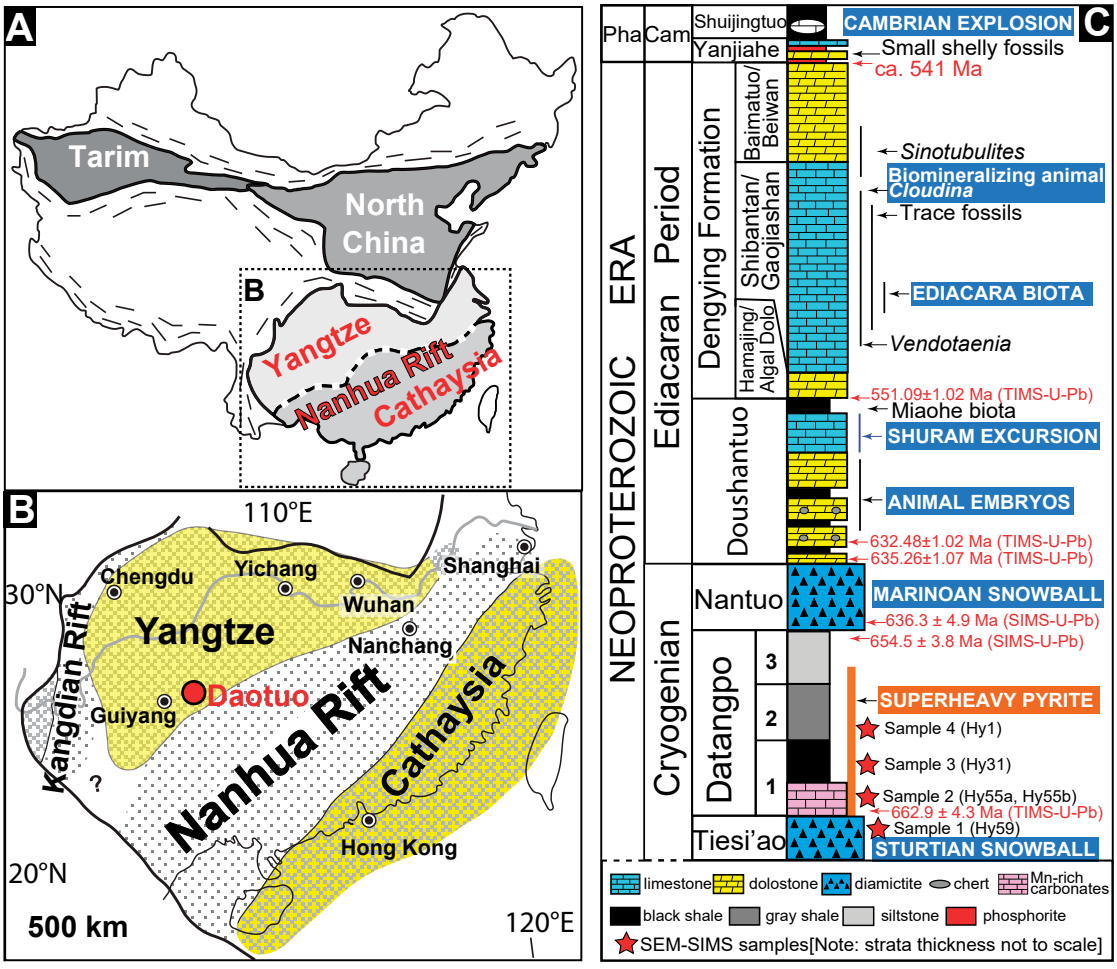

FIGURE 2. (**a**) Tectonic map of China. (**b**) Reconstructed Yangtze and Cathaysia blocks with the Nanhua rift in between (Li et al. 1999b; Jiang et al. 2003; Wang and Li 2003; Zhang et al. 2008). Red dot indicates the location of the studied Daotuo mine at Songtao, eastern Guizhou Province. (**c**) Simplified litho-, bio-, and chrono-stratigraphy of the Neoproterozoic strata in South China. Source of the lithology and fossil record (Jiang et al. 2007, 2011; McFadden et al. 2008; Cai et al. 2010; Chen et al. 2013, 2014; Cui 2015, 2016b, 2017). Source of the radiometric ages (Zhou et al. 2004; Condon et al. 2005; Zhang et al. 2008; Schmitz 2012; Chen et al. 2015). Superheavy pyrite has been widely reported from the post-glacial Datangpo Formation (see text). Thickness is not to scale. Cam = Cambrian; Pha = Phanerozoic.

trates extracted from bulk samples is not sufficient to constrain the $\delta^{34}S_{sulfate}$ signals of contemporaneous seawater. To test this hypothesis, it is critical to analyze the $\delta^{34}S_{pyrite}$ values in situ at the micrometer scale.

The focus of this study is the Cryogenian strata in South China (Fig. 2). Superheavy pyrite has been widely reported from the Cryogenian Datangpo Formation in South China with anomalously high $\delta^{34}S_{pyrite}$ values up to ca. +70‰ (Liu et al. 2006, 2012; Wu et al. 2016). The post-Sturtian seawater $\delta^{34}S_{sulfate}$ value is estimated to be ca. +26‰ based on nodular and "chicken wire" anhydrite in Australia (Gorjan et al. 2000), or no more than ca. +50‰ based on carbonate-associated sulfate (CAS) analysis of the Cryogenian carbonates in Australia, Namibia (Hurtgen et al. 2005) and South China (Lang 2016). Based on these $\delta^{34}S_{sulfate}$ constraints, many of the published $\delta^{34}S_{pyrite}$ values from the Cryogenian Datangpo Formation are much higher than the inferred coeval seawater $\delta^{34}S_{sulfate}$ values (Fig. 1; Appendix[1] 1).

Interrogating the superheavy pyrite

To understand the origin of the superheavy pyrite, two outstanding questions should be addressed. First, how to create and maintain a high-$\delta^{34}S_{sulfate}$ reservoir? Based on current knowledge of sulfur isotope systems, to generate high-$\delta^{34}S_{pyrite}$ values requires a sulfate reservoir with even higher $\delta^{34}S_{sulfate}$. Therefore, the existence of a sulfate reservoir with extremely high-$\delta^{34}S_{sulfate}$ has been invoked in multiple models. Models for such high-$\delta^{34}S_{sulfate}$ reservoirs show a wide spectrum of geological settings: an ice-covered ocean during a hard snowball-Earth glaciation (Gorjan et al. 2000, 2003; Walter et al. 2000; Parnell and Boyce 2017), a restricted basin with limited access to the open ocean (Li et al. 2012), an isolated porewater system (Chen et al. 2008), a sulfate minimum zone in the water column (Logan et al. 1995), a stratified ocean with substantial burial of pyrite in the euxinic deep ocean (Logan et al. 1995; Canfield 2004), or a local euxinic water mass with active emissions of low-$\delta^{34}S_{org}$ organic sulfur (Lang 2016; Lang et al. 2016).

Second, how to reverse sulfur isotope fractionations ($\Delta^{34}S_{sulfate\text{-}sulfide}$) to negative values? During MSR, $\delta^{34}S_{pyrite}$ can approach, but not be higher than, the coexisting $\delta^{34}S_{sulfate}$ signals. Therefore, to produce reversed $\Delta^{34}S_{sulfate\text{-}sulfide}$ values, the sulfur reservoirs of $\delta^{34}S_{sulfate}$ and $\delta^{34}S_{sulfide}$, respectively, have to be decoupled. In other words, two coexisting, but separated, sulfur reservoirs are needed to explain the reversed values of $\Delta^{34}S_{sulfate\text{-}sulfide}$. Such conditions are uncommon in marine environments.

Implicit among most of the published models is the notion that the superheavy pyrite formed via MSR. However, this assumption has not been tested. To test this assumption and reevaluate published models, an integrated approach that combines both basin-scale field observation and micrometer-scale SIMS $\delta^{34}S_{pyrite}$ analysis coupled to scanning electron microscopy (SEM)-based petrography is required. For example, pyrite formed in seawater (i.e., open system) vs. in pore waters (i.e., restricted system) could result in different patterns of $\delta^{34}S_{pyrite}$ at micrometer scale when Rayleigh fractionation occurs. Higher $\delta^{34}S_{pyrite}$ values are expected to be recorded in strongly zoned late-stage overgrowths of pyrite if it forms in an increasingly fractionated pore-water system. In contrast, pyrite formed in the marine water column should record relatively low $\delta^{34}S_{pyrite}$ values without strong heterogeneity in $\delta^{34}S_{pyrite}$ at the micrometer scale. In addition, pyrite formed during early syndepositional diagenesis vs. late burial diagenesis could also be reflected in paragenesis, and revealed by petrography.

In this study, we aim to test published models for the genesis of Neoproterozoic superheavy pyrite in South China using the novel SEM-SIMS approach. Detailed petrographic observations by SEM and in situ micrometer-scale $\delta^{34}S_{pyrite}$ analysis by secondary ion mass spectrometry (SIMS) were performed for the pyrite samples. The SIMS $\delta^{34}S_{pyrite}$ analyses are coupled with detailed petrographic observations by SEM and trace elements by electron-probe microanalysis (EPMA). New data in this study will test if superheavy pyrite formed via microbial sulfate reduction (MSR). Alternatively, we will also test if superheavy pyrite formed via thermochemical sulfate reduction (TSR) during a post-depositional hydrothermal event. This is in strong contrast with the widely accepted assumption, held for decades, of a MSR origin for the Neoproterozoic superheavy pyrite in South China.

Background

Current interpretations of the deep-time $\delta^{34}S$ records apply fractionations of sulfur isotopes between sulfate and sulfide ($\Delta^{34}S_{sulfate\text{-}sulfide} = \delta^{34}S_{sulfate} - \delta^{34}S_{sulfide}$). Before fully investigating the Neoproterozoic superheavy pyrite, a brief review of sulfur isotopes is necessary.

Microbial sulfate reduction (MSR)

MSR is the dominant mechanism that fractionates sulfur isotopes in marine environments. It is often expressed as the following simplified reactions:

$$2CH_2O + SO_4^{2-} \rightarrow 2HCO_3^- + H_2S \quad (1)$$

$$CH_4 + SO_4^{2-} \rightarrow HCO_3^- + HS^- + H_2O. \quad (2)$$

Most MSR occurs at temperatures lower than ~100 °C (Jørgensen et al. 1992). During MSR, sulfate-reducing bacteria reduce sulfate to sulfide and form pyrite with $\delta^{34}S$ values lower than the coexisting sulfate (i.e., $\delta^{34}S_{sulfide} < \delta^{34}S_{sulfate}$) (Kaplan and Rafter 1958; Kaplan and Rittenberg 1964; Canfield 2001a; Böttcher 2011). MSR-induced sulfur isotope fractionation $\Delta^{34}S_{sulfate\text{-}sulfide}$ up to +40‰ has been produced in lab experiments (Canfield 2001b). More recently, experiments with pure cultures of sulfate reducers show a maximal $\Delta^{34}S_{sulfate\text{-}sulfide}$ of +66‰ at sulfate concentrations ($[SO_4^{2-}]$) similar to modern seawater at 28 mM (Sim et al. 2011a). Even larger $\Delta^{34}S_{sulfate\text{-}sulfide}$ values of up to +72‰ have been found in natural samples (Wortmann et al. 2001; Canfield et al. 2010; Sim et al. 2011a).

Sulfate concentrations ($[SO_4^{2-}]$) in solutions can strongly influence the magnitude of $\Delta^{34}S_{sulfate\text{-}sulfide}$. Experimental studies of microbial cultures demonstrate that the degree of MSR-induced sulfur isotope fractionation in both seawater and freshwater can be increasingly suppressed as $[SO_4^{2-}]$ decreases, and $\Delta^{34}S_{sulfate\text{-}sulfide}$ approaches zero when $[SO_4^{2-}]$ is less than 200 μM (Habicht et al. 2002). However, a more recent study based on Lake Matano (Indonesia) suggests large fractionations (>20‰) at sulfate levels below 200 μM (Crowe et al. 2014).

In addition, environmentally controlled experiments suggest

that the magnitude of MSR-induced sulfur isotope fractionation is also related to strain-specific factors (Fike et al. 2015; Bradley et al. 2016), intracellular metabolite levels (Wing and Halevy 2014), and sulfate reduction rate that depends on the availability of organic substrates as electron donors (Canfield et al. 2010; Leavitt et al. 2013; Leavitt 2014; Fike et al. 2015; Gomes and Hurtgen 2015). The magnitude of $\Delta^{34}S_{sulfate\text{-}sulfide}$ is found to be inversely proportional to the cell-specific sulfate reduction rate (csSRR) (Harrison and Thode 1958; Kaplan and Rittenberg 1964; Chambers et al. 1975; Sim et al. 2011a, 2011b, 2012; Leavitt et al. 2013; Fike et al. 2015). This inverse relationship between $\Delta^{34}S_{sulfate\text{-}sulfide}$ and csSRR is consistent with observations in modern marine sediments, particularly in the sulfate–methane transition zone (SMTZ) where MSR rate reaches a maximum in the presence of an upward methane flux and a downward sulfate flux (Jørgensen et al. 2004; Lin et al. 2016b). Additionally, sedimentation rate could also play a role in controlling the expression of $\Delta^{34}S_{sulfate\text{-}sulfide}$. Studies suggest that higher sedimentation rate could cause smaller $\Delta^{34}S_{sulfate\text{-}sulfide}$ and higher $\delta^{34}S_{pyrite}$ values, and conversely, lower sedimentation rate could cause larger $\Delta^{34}S_{sulfate\text{-}sulfide}$ and lower $\delta^{34}S_{pyrite}$ values (Goldhaber and Kaplan 1975; Claypool 2004; Pasquier et al. 2017).

In marine environments, bacterial sulfur disproportionation (BSD) could also play a significant role in fractionating the sulfur isotopes. During BSD, sulfides produced through MSR are re-oxidized to elemental sulfur, and then subsequently disproportionated to sulfate and sulfide, by coupling with the reduction of O_2, NO_3^-, iron or manganese compounds (Canfield and Thamdrup 1994; Canfield and Teske 1996; Canfield 2001a; Fike et al. 2015). Disproportionation reactions can significantly augment the fractionation of sulfur isotopes, resulting in isotopic contrasts between reactant sulfate and product sulfide with $\Delta^{34}S_{sulfate\text{-}sulfide}$ greater than +70‰. The involvement of BSD has been proposed to occur in the rock record of multiple geological intervals (Canfield and Teske 1996; Johnston et al. 2005; Fike et al. 2006; Wu et al. 2015b; Cui et al. 2016b; Kunzmann et al. 2017).

Published studies of MSR-derived pyrite in sedimentary rocks typically show strong heterogeneity in $\delta^{34}S_{pyrite}$ values at micrometer scales (Machel et al. 1997; Kohn et al. 1998; Machel 2001; Wacey et al. 2010; Williford et al. 2011; Lin et al. 2016b; Meyer et al. 2017; Peng et al. 2017; Gomes et al. 2018; Marin-Carbonne et al. 2018). This is largely due to a biogenic nature of MSR and the involvement of Rayleigh fractionation in restricted pore waters (Kohn et al. 1998; McLoughlin et al. 2012; Wacey et al. 2015). As MSR proceeds in pore water environments, the restricted flow of porewaters and Rayleigh fractionation causes progressively lower $\Delta^{34}S_{sulfate\text{-}sulfide}$, higher $\delta^{34}S_{sulfate}$, and consequently higher $\delta^{34}S_{sulfide}$ values (Kaplan and Rafter 1958; Kaplan and Rittenberg 1964; Canfield 2001a).

Rayleigh fractionation of sulfur isotopes can be expressed at both stratigraphic meter-to-kilometer and micrometer scales. (1) Stratigraphically, $\delta^{34}S$ values of both porewater sulfate and authigenic pyrite typically increase with greater burial depth (Goldhaber and Kaplan 1980; Borowski et al. 2000; Canfield 2001a; Fike et al. 2015). (2) At micrometer scales, as pyrite grains continuously grow during diagenesis, the late-stage pyrite overgrowth typically records higher $\delta^{34}S_{pyrite}$ values than the early-stage pyrite (e.g., Raiswell 1982; McKibben and Riciputi 1998; Ferrini et al. 2010; Williford et al. 2011; Fischer et al. 2014; Drake et al. 2015, 2017; Lin et al. 2016b). Both phenomena reflect the occurrence of Rayleigh fractionation in the broad spectrum of the post-depositional process. Therefore, strong heterogeneity in $\delta^{34}S_{pyrite}$ is predicted to be common in MSR-dominated environments.

Taken together, MSR could cause significant fractionation between sulfate and sulfide. The controlling factors of $\Delta^{34}S_{sulfate\text{-}sulfide}$ in marine environments are non-unique. Multiple factors may play a role, including sulfate concentration, MSR rate, organic carbon availability, and sulfide re-oxidation. Rayleigh fractionation of sulfur isotopes in restricted pore waters could cause strong $\delta^{34}S$ heterogeneity at both stratigraphic and mineral scales.

Thermochemical sulfate reduction (TSR)

Thermochemical sulfate reduction is an abiotic process by which sulfate is reduced by organic matter during heating. The temperatures of TSR are typically higher than 110 °C (Goldstein and Aizenshtat 1994; Machel et al. 1995; Worden et al. 1995; Machel 2001; Jiang et al. 2015). The reactants and products of TSR and MSR can be very similar, therefore distinguishing these two sulfate-reduction pathways is not straightforward and often requires multiple lines of evidence (Machel et al. 1995; Machel 2001).

The $\Delta^{34}S_{sulfate\text{-}sulfide}$ induced by TSR remains poorly constrained compared with that of the MSR. Lab experiments show that the TSR rate is strongly dependent on temperatures (Kiyosu 1980; Kiyosu and Krouse 1990). The TSR-induced values of $\Delta^{34}S_{sulfate\text{-}sulfide}$ caused by hydrocarbons at $T > 200$ °C are typically around 25‰ (Ohmoto and Goldhaber 1997). However, disequilibrium $\Delta^{34}S_{sulfate\text{-}sulfide}$ values ranging from +20.8 to –5.0‰ have also been reported in TSR experiments using amino acids (Watanabe et al. 2009). Published lab experiments suggest that the $\Delta^{34}S_{sulfate\text{-}sulfide}$ value at equilibrium is ~40‰ (Friedman and O'Neil 1977) or ~30‰ (Ohmoto and Lasaga 1982; Ohmoto 1986; Ohmoto and Goldhaber 1997; Seal 2006) at the temperature of ~200 °C.

The occurrence of TSR has been widely reported in hydrocarbon reservoirs (Orr 1974, 1977; Machel 1987; Heydari and Moore 1989; Worden et al. 1995; Riciputi et al. 1996; Worden and Smalley 1996; Worden et al. 2000; Cai et al. 2001, 2003, 2004, 2015; Zhu et al. 2007a, 2007b, 2015; Hao et al. 2008; Machel and Buschkuehle 2008; Jiang et al. 2014, 2015; King et al. 2014; Jia et al. 2015; Biehl et al. 2016; Fu et al. 2016; Liu et al. 2016; Olanipekun and Azmy 2018). It was revealed that TSR can play a significant role in enhancing the secondary porosity and permeability of carbonate reservoirs (Jiang et al. 2018).

TSR has also been invoked as an important process in ore deposits (Rye and Ohmoto 1974; Powell and Macqueen 1984; Ghazban et al. 1990; Tompkins et al. 1994; Randell and Anderson 1996; Alonso et al. 1999; Cooke et al. 2000; Peevler et al. 2003; Kelley et al. 2004a, 2004b; Basuki et al. 2008; Gadd et al. 2017; Soœnicka and Lüders 2018). Hydrothermal sulfate-bearing fluids that percolated through preexisting evaporites could react with organic matter and form pyrite deposits.

TSR could also be critical in interpreting the sulfur isotope records of the early Earth. It has been found that TSR could produce anomalous mass-independent fractionation (MIF) sig-

nals of sulfur isotopes ($\Delta^{33}S$ = +0.1 to +2.1‰ and $\Delta^{36}S$ = –1.1 to +1.1‰) by using specific amino acids (Watanabe et al. 2009; Oduro et al. 2011), which may have been largely overlooked in the study of the early Earth (Watanabe et al. 2009; Ohmoto et al. 2014). In a more recent study, $\delta^{34}S_{pyrite}$ signals up to +90‰ have been found in the early Paleoproterozoic succession (2.415 Ga) in South Africa, which have been interpreted as resulting from late fluids during burial metamorphism and late diagenesis (Johnson et al. 2013).

In summary, the occurrence of TSR has been widely reported from hydrocarbon reservoirs and ore deposits. TSR has also been invoked in the study of sulfur isotope signals of the deep-time records. The TSR-induced $\Delta^{34}S_{sulfate\text{-}sulfide}$ is relatively less constrained than that of the MSR, but $\Delta^{34}S_{sulfate\text{-}sulfide}$ is dependent on temperatures with smaller fractionations in higher temperatures.

Geological settings

Stratigraphy and paleogeography

The focus of this study is the Cryogenian Tiesi'ao and Datangpo formations in South China (Figs. 2a–2c). The Tiesi'ao and Datangpo formations have been widely regarded as a glacial-postglacial transition in South China. The Tiesi'ao Formation is a glacial diamictite interval of the Sturtian glaciation. The overlying Datangpo Formation is typically subdivided into three members by local mining companies, which are, in ascending order, Member 1 black shale with basal Mn-rich carbonate intervals, Member 2 gray shale, and Member 3 siltstone (Fig. 2c) (Xu et al. 1990; Zhou et al. 2004; Qin et al. 2013; Zhu et al. 2013; Xie et al. 2014; Wu et al. 2016). The Mn-rich carbonate interval in the basal Datangpo Formation has been proposed to be the Sturtian "cap carbonate" (Yu et al. 2017) and is the main target for Mn mining in South China (Wu et al. 2016).

Paleogeographic reconstructions in previous studies reveal that a southeast facing (present direction) passive margin on the Yangtze block was developed during the breakup of the Rodinia supercontinent (Figs. 2a and 2b**)** (Jiang et al. 2003; Wang and Li 2003; Hoffman and Li 2009; Li et al. 2013). Therefore a rift basin was formed in South China during the Cryogenian Period (Fig. 2b). The Datangpo Formation is mainly distributed in the slope and basinal facies (Xu et al. 1990; Xiao et al. 2014; Wu et al. 2016).

Age constraints

The ages of the Neoproterozoic strata in South China are relatively well constrained. Based on a TIMS U–Pb age of 662.9 ± 4.3 Ma (Zhou et al. 2004) and a SIMS U–Pb age of 667.3 ± 9. 9 Ma (Yin et al. 2006) analyzed from zircons in the tuff beds within the Mn-rich carbonate interval of the basal Datangpo Formation (Fig. 2c), the Tiesi'ao diamictite and Mn-rich carbonate couplet is constrained to be of the Sturtian age (Zhou et al. 2004; Yin et al. 2006).

Stratigraphically upward, the Datangpo Formation is overlain by the Cryogenian Nantuo diamictite, and then the Ediacaran Doushantuo (635–551 Ma) and Dengying (551–541 Ma) formations. A SIMS U–Pb age of 654.5 ± 3.8 Ma from an ash bed immediately below the Nantuo Formation provides a maximum age for the upper boundary of the Datangpo Formation (Zhang et al. 2008). Based on a TIMS U–Pb age of 635.2 ± 0.6 Ma analyzed from a tuff bed within the cap dolostone right above the Nantuo diamictite, the Nantuo Formation is constrained to be a Marinoan counterpart (Condon et al. 2005). The ages from South China and other basins suggest that the Cryogenian glaciations are synchronous at a global scale (Calver et al. 2013; Lan et al. 2015a, 2015b; Rooney et al. 2015; Song et al. 2017).

Distribution of the superheavy pyrite

Superheavy pyrites with bulk $\delta^{34}S$ values up to ca. +70‰ have been reported in the postglacial Datangpo Formation (Fig. 1) (Wang et al. 1985, 2016; Tang 1990; Li et al. 1996, 1999a; Chu et al. 1998, 2001, 2003; Tang and Liu 1999; Yang et al. 2002; Liu et al. 2006; Zhou et al. 2007; Chen et al. 2008; Feng et al. 2010; Li et al. 2012; Zhang et al. 2013, 2014; Zhu et al. 2013; Wu et al. 2015a, 2016). A comprehensive compilation of the distributions of the Datangpo superheavy pyrite at a basin scale reveals a close association with ancient faults (see Fig. 12 of Wu et al. 2016). Similarly, the Datangpo manganese deposits are also associated with ancient faults (Qin et al. 2013; Zhou et al. 2013). Field studies of the Datangpo Formation show abundant textures that suggest pervasive overprint by hydrothermal fluids triggered by tectonic events. These textures include faulting, host rock breccia, sharp-sided quartz veins, calcite, gypsum, and barite infillings and veins (Xu et al. 1990; Chen and Chen 1992; He et al. 2013a, 2013b; Zhang et al. 2013; Pan et al. 2016).

Samples

Most chemostratigraphic studies analyze $\delta^{34}S_{pyrite}$ from milligram-size aliquots of powder obtained at greater than millimeter scale by crushing or drilling samples. These procedures homogenize samples that may be zoned or heterogeneous at micrometer-to-millimeter scale. In contrast, the SIMS analysis of this study sputtered 2 μm diameter pits (~1 μm deep) in situ from polished surfaces that had been imaged by SEM, representing samples over a million times smaller than in conventional analysis (less than nanogram vs. greater than milligram scale). By SIMS, it is only practical to examine a relatively small number of hand samples, but SEM examination makes it possible to select the representative or critical regions and a large amount of data can be efficiently obtained at this scale. The information density per sample can be extraordinarily high by SIMS yielding information that is inaccessible by other means (Eldridge et al. 1989; Valley and Kita 2009; Williford et al. 2016; Cui et al. 2018). Thus, the best-preserved, most-representative samples were selected for detailed analysis in this study.

The studied drill core (ZK1105, drilled in September 2015) is composed of the Cryogenian Tiesi'ao Formation and Datangpo Formation at the Daotuo mine (28°07′04″N, 108°52′26″E), Songtao County, eastern Guizhou Province in South China (Fig. 2b). The Daotuo mine represents the largest known Mn ore reserve (up to 142 Mt in carbonates) in China (Qin et al. 2013; Zhu et al. 2013; Wu et al. 2016), and records bulk $\delta^{34}S_{pyrite}$ values as high as ca. +70‰ (Fig. 1) (Zhu et al. 2013; Wu et al. 2016), providing a good opportunity for the study of superheavy pyrite and Mn metallogenesis.

Four samples were selected from the ZK1105 drill core for detailed SEM-SIMS $\delta^{34}S_{pyrite}$ study (Figs. 2c, 3, and 4). Sample 1 (drill core Hy59) is a diamictite specimen from the uppermost Tiesi'ao Formation. Sample 2 (drill core Hy55) is an Mn-rich

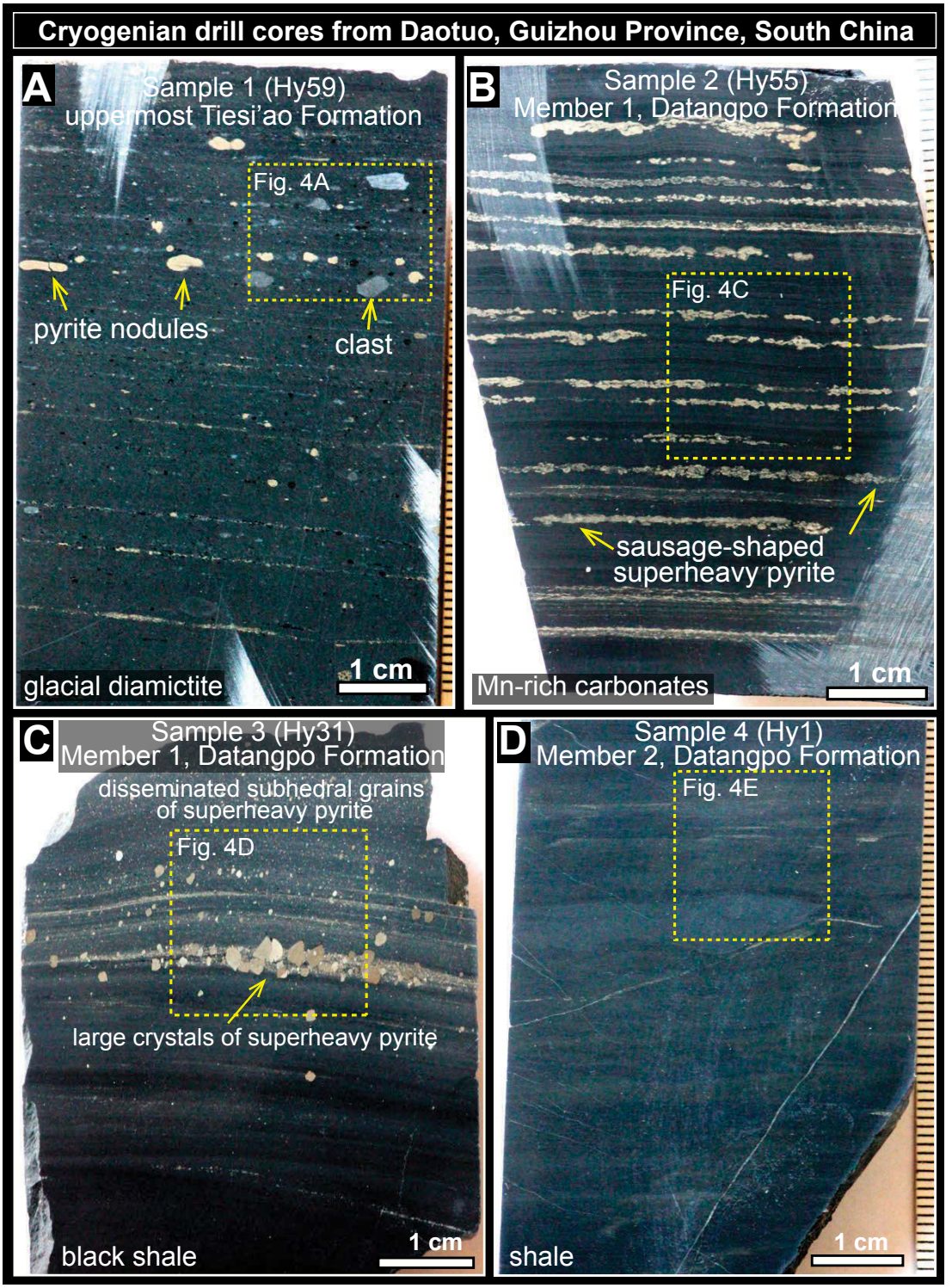

FIGURE 3. Four drill-core samples collected at the Daotuo mine, Guizhou Province, South China. Marked zones of the surfaces were prepared as SIMS mounts for further studies. (**a**) Sample 1 (Hy59, glacial diamictite) from the uppermost Tiesi'ao Formation. (**b**) Sample 2 (Hy55, Mn-rich carbonates) from the Member 1 of the Datangpo Formation. (**c**) Sample 3 (Hy31, shale) from the Member 1 of the Datangpo Formation. (**d**) Sample 4 (Hy1, shale) from the Member 2 of the Datangpo Formation. All the drill cores are 4.5 cm in diameter.

carbonate specimen from the lower Member 1 of the Datangpo Formation. Sample 3 (drill core Hy31) is black shale from the upper Member 1 of the Datangpo Formation. Sample 4 (drill core Hy1) is from lower Member 2 of the Datangpo Formation. These four samples cover the main lithologies (diamictite, Mn-rich carbonates, and shale) and pyrite morphology (including pyrite framboids, pyrite nodules, pyrite cements, and euhedral to subhedral pyrite grains) (Fig. 4). Individual pyrite grains were imaged by SEM with backscattered electrons (BSE) and secondary electrons (SE) prior to SIMS analysis. Mineral chemistry was verified by SEM energy-dispersive spectrometry (EDS) and electron-probe microanalysis (EPMA).

METHODS

SIMS analysis

Samples in this study were analyzed by a CAMECA IMS 1280 at the WiscSIMS (Wisconsin Secondary Ion Mass Spectrometry) Lab, Department of Geoscience, University of Wisconsin–Madison. The analyses include three SIMS sessions. During session 1 (October 18–19, 2016) and session 3 (June 8, 2017), two sulfur isotopes (^{32}S, ^{34}S) were measured with a 2 µm diameter beam size. During session 2 (May 22, 2017), three sulfur isotopes (^{32}S, ^{33}S, ^{34}S) were measured with a 10 µm diameter beam size.

The UWPy-1 standard (pyrite from the Balmat Mine, New York, $\delta^{34}S = 16.04 \pm 0.18‰$, $\Delta^{33}S = -0.003 \pm 0.009‰$, 2 SD, V-CDT) (Ushikubo et al. 2014) was used to calibrate analyses of pyrite. Sulfur isotope ratios are reported in standard per mil (‰) notation relative to V-CDT, calculated as $\delta^{34}S_{unknown} = [(^{34}S/^{32}S)_{unknown}/(^{34}S/^{32}S)_{VCDT} - 1] \times 1000$. Measured ratios of $^{34}S/^{32}S$, were divided by the

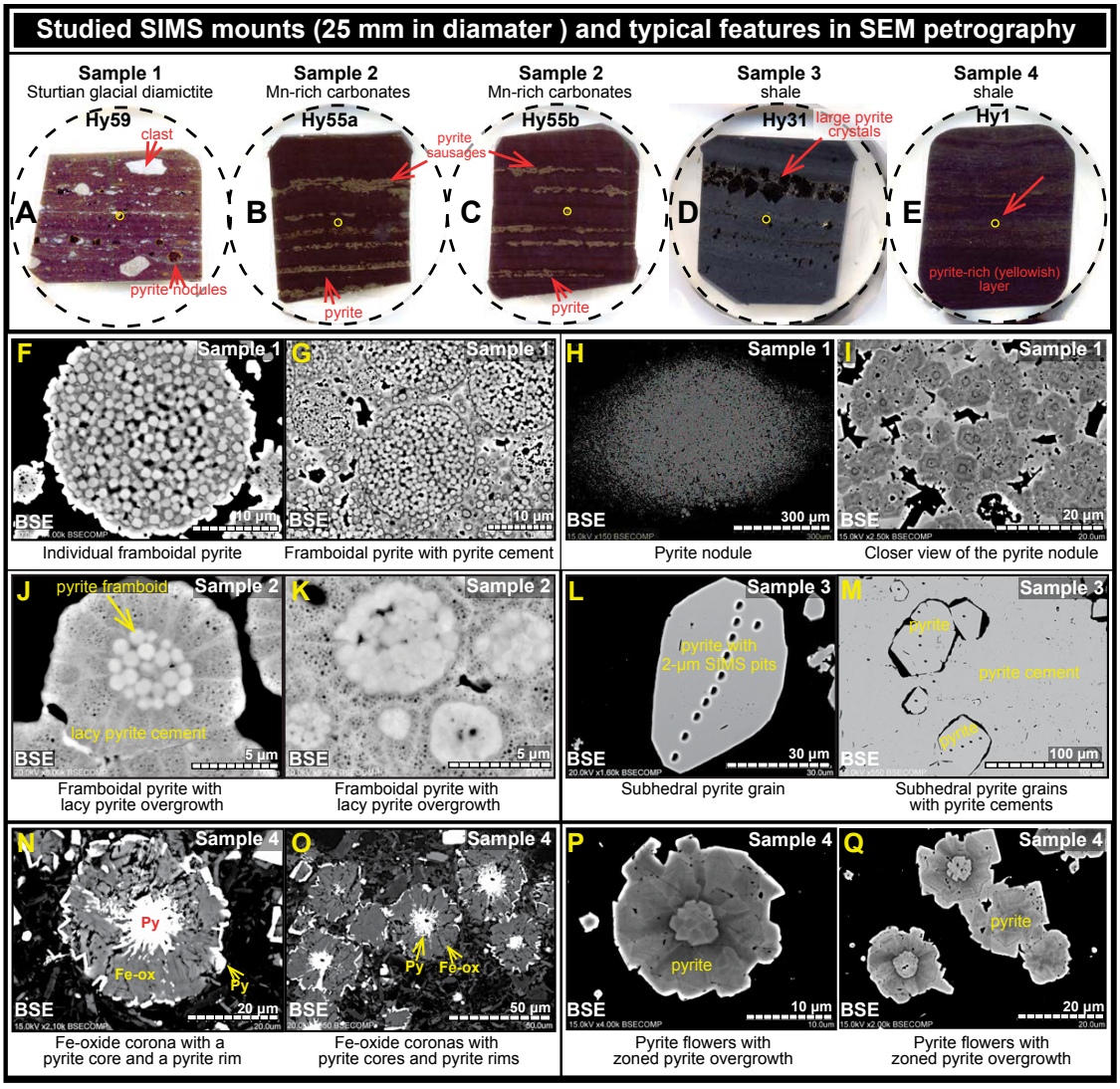

FIGURE 4. Studied SIMS mounts and typical petrographic features of each sample. (**a–e**) 25 mm-diameter SIMS mounts with in-house pyrite standard UWPy-1 (marked as yellow circles) mounted in the center of each mount. (**f–q**) Typical features by SEM-BSE. **f–i** Sample 1 (Hy59); **j–k** Sample 2 (Hy55); **l–m** Sample 3 (Hy31); and **n–q** Sample 4 (Hy1). (**f**) Individual pyrite framboid in Sample 1. (**g**) Framboidal pyrite with pyrite cement in Sample 1. (**h**) A large pyrite nodule in Sample 1. (**i**) A magnified view of the individual zoned pyrite crystals within the pyrite nodule in Sample 1. (**j** and **k**) Framboidal pyrite with lacy pyrite overgrowth in Sample 2. (**l**) Subhedral pyrite grain in Sample 3. (**m**) Subhedral pyrite grains with pyrite cements in Sample 3. (**n** and **o**) "Fe-oxide coronas" with pyrite cores and pyrite rims. Py: pyrite; Fe-ox: Fe oxide. Small black spots in **l**, **m**, and **o** showing SIMS pits. (**p** and **q**) "Pyrite flowers" in Sample 4 showing framboidal pyrite cores and zoned pyrite overgrowth. Abbreviations: BSE = backscattered electron; SE = secondary electron. For more detailed SEM images of the studied samples, see online Appendices 2–5.

TABLE 1. Summary of SEM-SIMS results in this study of Cryogenian pyrite from Daotuo, South China

SIMS samples	Sample 1 (Hy59)	Sample 2 (Hy55)
Stratigraphic position	Uppermost Tiesi'ao Fm	Basal Mb 1, Datangpo Fm
Lithology	Terminal-Sturtian glacial diamictite	Post-Sturtian Mn-rich carbonates
SEM-SIMS results	Figs. 5–8; Appendix 2	Figs. 9–14; Appendix 3
Pyrite morphology and grain size	Framboidal pyrite: up to ~30 µm; Pyrite nodules: ~1 to ~2 mm	Framboidal pyrite: up to 7 µm; Lacy pyrite overgrowth: micro- to centimeter scale, showing lacy textures, metasomatic corrosion boundaries, and relatively darker color (compared with the framboids) under BSE
Number of SIMS analyses (n)	Framboidal pyrite: n = 76; Pyrite cements outside; Framboids: n = 4 Pyrite nodules: n = 10	Framboidal pyrite: n = 5; Lacy pyrite overgrowth: n = 15; Mixture between framboids and overgrowth: n = 8
Range of SIMS $\delta^{34}S$ values ‰ V-CDT	Pyrite nodules: +9.8 to +52.2‰; Pyrite framboids: +11.2 to +28.3‰; Pyrite cements outside framboids: +22.7 to +36.7‰	Lacy pyrite overgrowth: +56.3 to +60.4‰; Mixture of framboids and overgrowth: +56.8 to +58.3‰; Pyrite framboids: +56.3 to +57.4‰
Mean $\delta^{34}S$ ‰ V-CDT	Pyrite nodules: +26.5‰; Pyrite framboids: +16.4‰; Pyrite cements outside framboids: +30.9‰	Lacy pyrite overgrowth: +57.8‰; Mixture of framboids and overgrowth: +57.4‰; Pyrite framboids: +56.9‰
Intra-grain $\delta^{34}S$ pattern	No systematic increasing or decreasing $\delta^{34}S$ trend	Not available
$\delta^{34}S$ patterns on micrometer scales	Heterogeneous, mostly not superheavy	Homogeneous, superheavy
Mean $^{32}S^{1}H/^{32}S$	Pyrite nodules: 8.7E-3; Pyrite framboids: 1.2E-2; Pyrite cements outside framboids: 1.0E-2	Lacy pyrite overgrowth: 1.6E-2; Mixture of framboids and overgrowth: 1.5E-2; Pyrite framboids: 1.3E-2
Paragenesis	Framboidal pyrite: syngenetic (water column) to early diagenesis; Pyrite nodules: early to late diagenesis	Framboidal pyrite: late diagenesis (petrographically replacing rhodochrosite and illite); Lacy pyrite overgrowth: postdating framboids
Interpretation in this study	Biogenic, microbial sulfate reduction	Abiogenic, thermochemical sulfate reduction

Note: For the detailed petrographic context of all the geochemical data, the reader is referred to the online appendices (Appendices[1] 2–5).

(Table extends onto next page.)

V-CDT value of $^{34}S/^{32}S$ = 1/22.6436 (Ding et al. 2001), and were calculated as "raw" δ-values $\delta^{34}S_{raw}$ before converting to the V-CDT scale based on eight analyses of UWPy-1 that bracket each group of 10–15 sample analyses. All the data can be found in the online appendices (Appendices 2–6).

SIMS sessions 1 and 3 (^{32}S, ^{34}S analysis; 2 µm beam size). Measurements of $^{34}S/^{32}S$ were made using a $^{133}Cs^{+}$ primary ion beam with an intensity of ~30 pA in session 3, which was focused to approximately 2 × 1 µm at the surface of the sample. The secondary $^{32}S^{-}$, $^{34}S^{-}$, and $^{32}S^{1}H^{-}$ ions were simultaneously collected by detectors L'2, FC2, and C, respectively, using three Faraday cups. The secondary ion intensity of $^{32}S^{-}$ was ~6×10^{7} cps and ~2.2×10^{7} cps for in sessions 1 and 3, respectively. $^{32}S^{1}H^{-}$ was analyzed to evaluate the effect of hydrogen that might be in the form of organic matter on the SIMS results. An electron flood gun in combination with a gold coat (~40 nm) was used for charge compensation. The total analytical time per spot was about 4 min including pre-sputtering (60 s), automatic centering of the secondary ion beam in the field aperture (90 s), and analysis (80 s). The baseline noise level of the Faraday cups was monitored during pre-sputtering. The spot to spot precision of $\delta^{34}S_{raw}$ values based on all bracketing analyses of 2 µm spots on standard UWPy-1 is ±0.91‰ and ±0.87‰, respectively, in session 1 and session 3 (2SD, Appendix[1] 7).

SIMS session 2 (^{32}S, ^{33}S, ^{34}S analysis; 10 µm beam size). During session 2, the secondary ion intensity was ~1.4×10^{9} cps for $^{32}S^{-}$. The ions ^{32}S, ^{33}S, ^{34}S were simultaneously analyzed by detector L'2, C, FC2, respectively, using three Faraday cups. Mass resolving power (M/ΔM, measured at 10% peak height) was set to ~5000. Analysis time consisted of 30 s for pre-sputtering, 80 s for centering of secondary ions in the field aperture, and 80 s for analysis. $^{32}S^{1}H^{-}$ was analyzed by detector C at the end of each spot analysis. The ratio of the $^{32}S^{1}H^{-}$ tail at the $^{33}S^{-}$ peak position relative to the $^{32}S^{1}H^{-}$ peak ($^{32}S^{1}H_{tail}/^{32}S^{1}H_{peak}$) was determined (6.95E-6) at the beginning of the session, which was used to correct the contribution of the $^{32}S^{1}H^{-}$ tail signal to the $^{33}S^{-}$ peak during each spot analysis. $^{32}S^{1}H^{-}$was measured by using a deflector (DSP2X, which is located after the magnet) and detector C at end of each analysis. The contribution of $^{32}S^{1}H^{-}$ to the $^{33}S^{-}$ peak in all the spots (9.7×10^{-4} ‰ at most, 6.6×10^{-4} ‰ on average) is negligible. The $\Delta^{33}S$ values were calculated as $\Delta^{33}S_{unknown} = \delta^{33}S_{unknown} - 10^{3} \times [(1 + \delta^{34}S_{unknown}/10^{3})^{0.515} - 1]$. The spot to spot precision of $\delta^{34}S$ and $\Delta^{33}S$ (values based on all bracketing analyses of 10 µm spots on standard UWPy-1) is ±0.18‰ and ±0.06‰, respectively (2 SD, Appendix[1] 7).

Gold-coat removal and SEM imaging

After SIMS analysis, the gold coating was removed from samples by chemical dissolution of gold using a saturated solution of potassium iodide (Jones et al. 2012). The gold-removing solution is a 0.02 mol/L solution of iodine in ethaline. Ethaline is prepared as a 1:2 molar mixture of choline chloride ($C_5H_{14}ClNO$) and ethylene glycol ($C_2H_6O_2$). The rinse solutions are potassium iodide solution and deionized water, respectively. The potassium iodide solution is prepared by adding potassium iodide (KI) to water until saturation. Samples were placed in the gold-removing solution on a hot plate at ~60 °C for 10 to 15 min, and then rinsed by a potassium iodide saturated solution. The samples were rinsed again with deionized water before further analysis.

SEM imaging was performed in the Ray and Mary Wilcox Scanning Electron Microscopy Laboratory, Department of Geoscience, University of Wisconsin–Madison. BSE images of carbon-coated samples were acquired with a Hitachi S3400 VP SEM with EDS using a Thermo-Fisher thin window detector. Each pit was investigated by SEM for possible irregularities. SEM images were acquired using an accelerating voltage of 15 or 20 keV at a working distance of 10 mm. All the SIMS pits were imaged by SEM and are shown with corresponding $\delta^{34}S_{pyrite}$ values in the online appendices (Appendices[1] 2–5).

EPMA analysis

EPMA analysis was conducted in the Eugene Cameron Electron Microbeam Lab, Department of Geoscience, University of Wisconsin–Madison. EPMA was performed with the CAMECA SXFive field emission electron probe, operated at 20 kV and 50 nA, and either a focused beam or a 3–4 µm defocused beam, using wavelength-dispersive crystal spectrometers (Appendix[1] 8). Counting times were 10 s on peak, and a total of 10 s on backgrounds, for all elements except those noted in the following listing. Al*K*α (20 s) and Si*K*α (20 s) were acquired on a large TAP crystal; As*K*α (20 s) and Se*K*α (20 s) on LIF; S*K*α and Ca*K*α (27 s) on large PET; Fe*K*α, Mn*K*α, and Co*K*α on LIF; and Ni*K*α, Cu*K*α, and Zn*K*α on large LIF. Standards used were Balmat pyrite (Fe, S), NBS glass K412 (Si, Al, Ca), arsenopyrite (As), and freshly polished metals for the balance. PHA modes used were integral except for Al and Si, which were differential mode. Software used was "Probe" for EPMA (Donovan et al. 2018). Off-peak backgrounds were acquired, and matrix correction was conducted by using the Armstrong/Love Scott algorithm (Armstrong 1988). Minimum detection levels are shown in Appendix[1] 8.

RESULTS

All the SIMS results in this study are shown with the petrographic context in online Appendices 2–5 and tabulated in online Appendix[1] 7. SIMS analyses of each spot that were off the correct target, with large internal error (2 SE > 2‰),

TABLE 1. —*EXTENDED*

SIMS samples	Sample 3 (Hy31)	Sample 4 (Hy1)
Stratigraphic position	Mb 1, Datangpo Fm	Mb 2, Datangpo Fm
Lithology	Post-Sturtian black shale	Post-Sturtian shale
SEM-SIMS results	Figs. 15–17; Appendix 4	Figs. 18–21; Appendix 5
Pyrite morphology and grain size	Subhedral pyrite: mostly 2 to 100 µm; Large pyrite with cemented individual pyrite grains: up to ~2 mm	Superheavy pyrite flowers (~15 µm in diameter): framboidal pyrite cores (~5 µm in diameter) with zoned pyrite overgrowth of ~5 µm in thickness; Fe-oxide coronas with pyrite rim (~35 µm in diameter) and pyrite cores (~10 µm in diameter)
Number of SIMS analyses (n)	Subhedral pyrite grains: n = 85; Later-stage pyrite cement: n = 23	Superheavy pyrite flowers: n = 25; Pyrite within Fe-oxide coronas: n = 21
Range of SIMS $\delta^{34}S$ values ‰ V-CDT	Individual pyrite grains: +60.3 to +71.2‰; Pyrite cements: +60.2 to +64.8‰	Superheavy pyrite flowers: +59.9 to +62.8‰; Pyrite cores withinFe-oxide coronas: +16.6 to +32.7‰
Mean $\delta^{34}S$ ‰ V-CDT	Individual pyrite grains: +66.3‰; Pyrite cements: +62.0‰	Superheavy pyrite flowers: +61.6‰; Pyrite cores within Fe-oxide coronas: +22.2‰
Intra-grain $\delta^{34}S$ pattern	Systematic decreasing $\delta^{34}S$ trend from core to edge of each individual grain	Not available
$\delta^{34}S$ patterns on micrometer scales	Individual pyrite grains: heterogeneous (in the range of ~10‰), superheavy; Pyrite cements: homogeneous, superheavy	Superheavy pyrite flowers: homogeneous, superheavy; Pyrite cores within Fe-oxide coronas: heterogeneous (in the range of ~16‰), not superheavy
Mean $^{32}S^{1}H/^{32}S$	Individual pyrite grains: 7.0E-4; Pyrite cements: 8.5E-4	Superheavy pyrite flowers: 9.7E-3; Pyrite cores within Fe-oxide coronas: 1.3E-2
Paragenesis	Disseminated subhedral pyrite: interpreted to be formed during late diagenesis; Pyrite cements: postdating individual pyrite grains	Superheavy pyrite flowers: late diagenesis; Pyrite cores within Fe-oxide coronas: syngenetic (water column) to early diagenesis
Interpretation in this study	Abiogenic, thermochemical sulfate reduction	Superheavy pyrite flowers: abiogenic, thermochemical sulfate reduction; Pyrite cores within Fe-oxide coronas: biogenic, microbial sulfate reduction

or with yield values (^{32}S count rate divided by primary beam intensity, Mcps/pA) that are beyond the range from 90 to 110% of the mean yield values for UWPy-1 are considered unreliable. A total of 258 SIMS analyses (6 data points are unreliable) were made during session 1, including 182 analyses of unknown samples and 76 analyses of the UWPy-1 standard. A total of 18 SIMS analyses (0 data filtered) were made during session 2, including 10 analyses of unknown samples and 8 analyses of the UWPy-1 standard. A total of 138 analyses (10 data filtered) were made during session 3, including 87 analyses of the unknown samples and 41 analyses of the UWPy-1 standard.

Integrated SEM–SIMS results of the studied samples show distinct patterns in pyrite paragenesis, S isotope ratios and spatial distributions at micrometer scale (Table 1; Figs. 4–23; Appendices[1] 2–5). These results are described below.

Sample 1 (Hy59, glacial diamictite)

SEM petrography. The pyrite phases in Sample 1 typically show two types of texture: pyrite framboids (up to 30 µm in diameter) (Figs. 4f, 4g, and 5–7; Appendix[1] 2) and pyrite nodules (Fig. 4h, 4i, and 8; Appendix[1] 2). (1) The pyrite framboids are mostly assemblages of smaller pyrite microcrystals (Figs. 4f, 4g, and 5–7). Sometimes, pyrite microcrystals may also occur outside the pyrite framboids as individual microcrystals surrounded by pyrite cement (Figs. 4g and 7a). BSE investigations at high magnification reveal that individual pyrite microcrystals are typically defined by a darker (lower average atomic number) rim (Fig. 5; Appendix[1] 2). The shape and size of the pyrite microcrystals are similar within individual framboids, but may vary among different framboids. Octahedral, subhedral, and rounded pyrite microcrystals have all been observed within different pyrite framboids (Fig. 5; Appendix[1] 2). (2) The pyrite nodules are mostly at millimeter scale, and consist of multiple zoned pyrite crystals at micrometer scales (Figs. 4h, 4i, and 8; Appendix[1] 2).

SIMS results. A total of 90 spots were analyzed by SIMS in different textures, including framboidal pyrite (n = 76), pyrite cements outside framboids (n = 4), and pyrite nodules (n = 10) (Appendix[1] 2). The $\delta^{34}S$ values measured from pyrite nodules range from +9.8 to +52.2‰. The $\delta^{34}S$ values measured from pyrite framboids range from +11.2 to +28.3‰. Pyrite cements outside the framboids show $\delta^{34}S$ ranging from +22.7 to +36.7‰ (Table 1; Figs. 22 and 23). Generally, the pyrite cements outside the framboids (+30.9‰ in average) have much higher $\delta^{34}S$ values than was measured within pyrite framboids (+16.4‰ on average) (Figs. 7a, 22, and 23).

Data evaluation. SEM investigation of Sample 1 shows that both the framboidal pyrite and the pyrite nodules are very heterogeneous at micrometer scale (Figs. 4f–4i and 5–8; Appendix[1] 2). The SIMS spots within the framboids may have covered both pyrite microcrystals that are smaller than the 2 µm beam spot and pyrite cements between the microcrystals (Fig. 5). Similarly, closer views of the pyrite crystals within nodules show zoned pyrite overgrowths (Figs. 4i and 8c–8j; Appendix[1] 2). Therefore, the measured $\delta^{34}S$ data from SIMS spots that include multiple phases should represent an averaged value of pyrite formed in different phases.

Sample 2 (Hy55, Mn-rich carbonates)

SEM petrography. Sample 2 is mainly composed of laminated Mn-rich carbonate layers and siliciclastic-rich layers (Figs. 9–14). The Mn-rich carbonate layers are mostly granular rhodochrosite [$MnCO_3$] (Fig. 10) and often show nodule- or sausage-shaped textures (Figs. 9 and 12; Appendix[1] 3). Trace

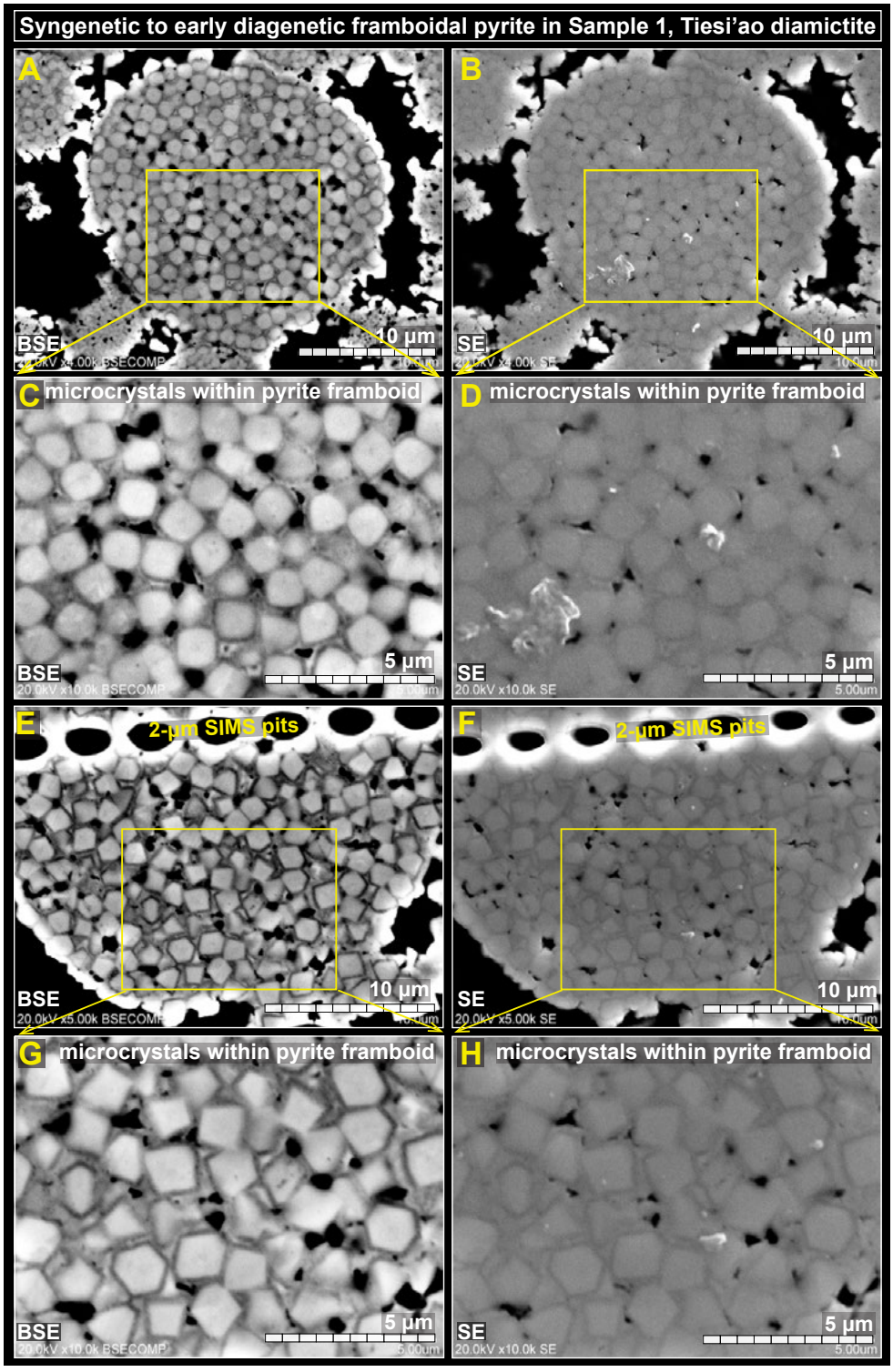

FIGURE 5. SEM petrography of the pyrite framboids in Sample 1. Images **c–d** and **g–h** show magnified views of marked areas in **a–b** and **e–f**, respectively. Note that the pyrite microcrystals within the framboids are typically surrounded by darker rims (possibly rich in inclusions or porosity) and pyrite cements. Abbreviations: BSE = backscattered electron; SE = secondary electron. For more detailed SEM images of the studied samples, see online Appendix[1] 2.

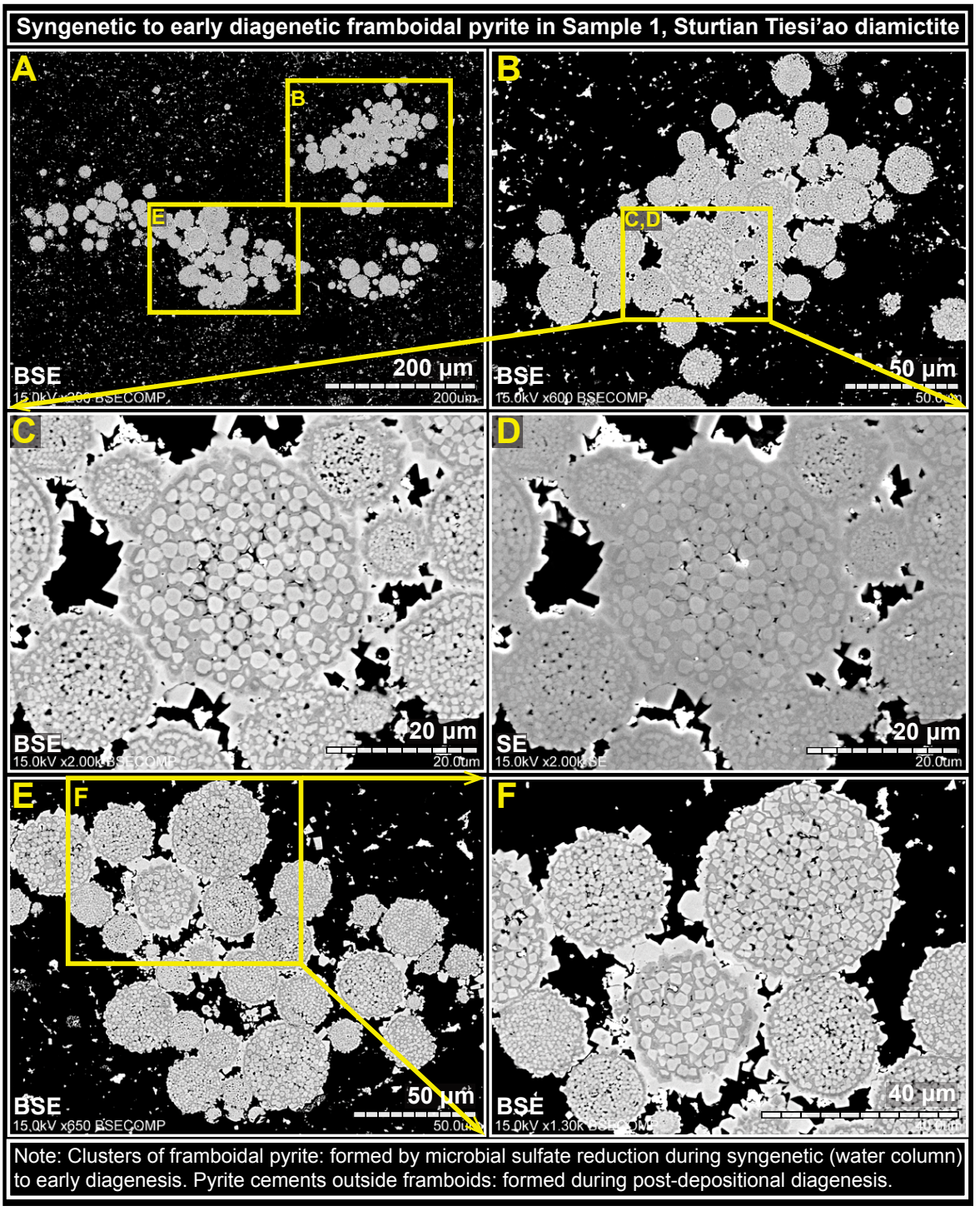

FIGURE 6. (**a**–**f**) SEM images showing clusters of framboidal pyrite in Sample 1. Magnified views are marked by yellow dash boxes. Note that many of the pyrite framboids are cemented by later-stage pyrite. Based on the petrography and $\delta^{34}S$ evidence, the framboidal pyrite in Sample 1 is interpreted to be syngenetic to early diagenetic in origin. See the main text for further discussion. Abbreviations: BSE = backscattered electron; SE = secondary electron. For more detailed SEM images, see online Appendix[1] 2.

amounts of euhedral kutnohorite [$CaMn(CO_3)_2$] were also found. Lath-shaped illite crystals are abundant in Sample 2 (Figs. 12 and 13; Appendix[1] 3). The pyrite in Sample 2 shows intermittent sausage-shaped textures (Figs. 9a–9f) that occur within the Mn-rich carbonate layers and preferentially replace the pre-existing carbonates (Figs. 9–13; Appendix[1] 3). The nodule- or

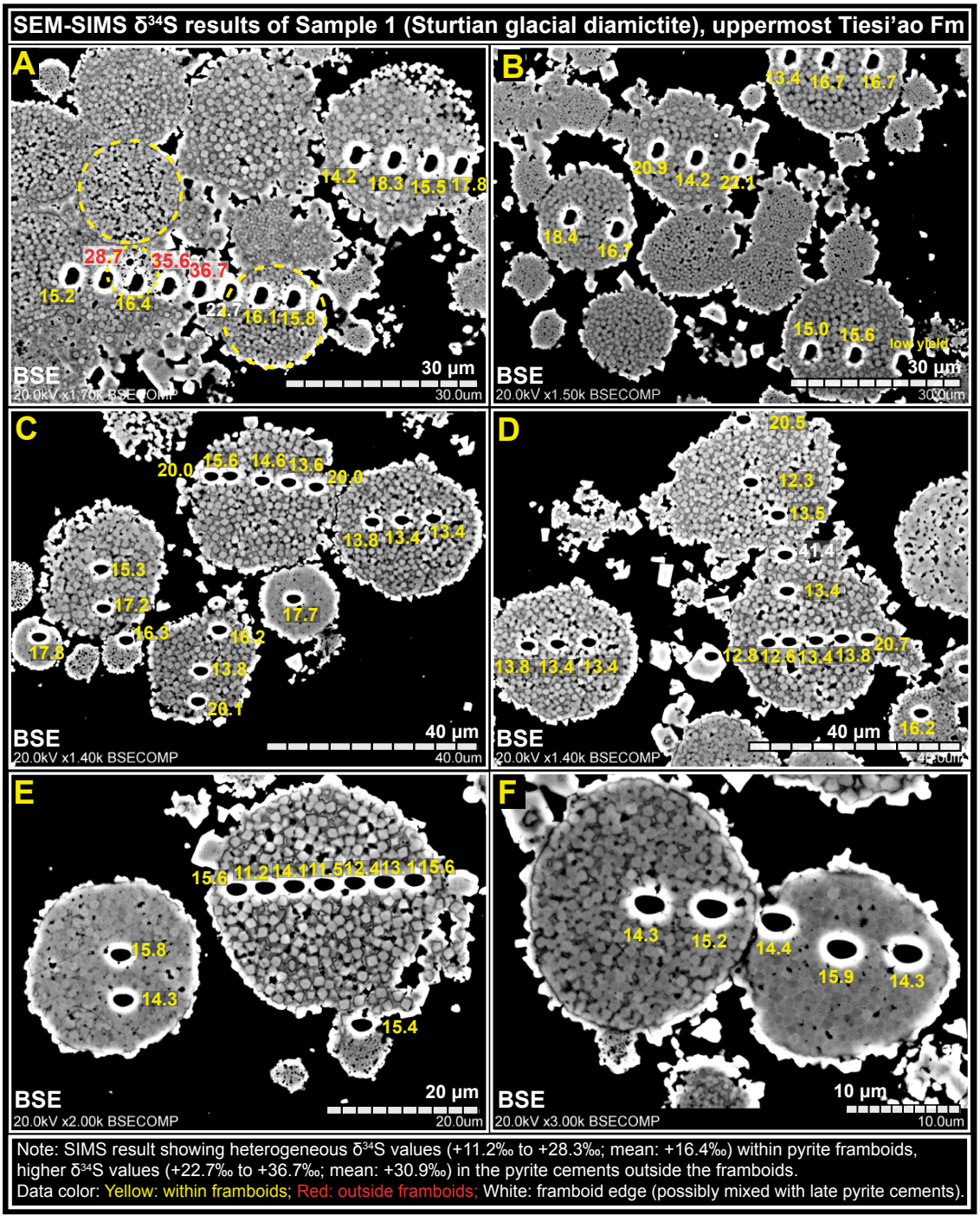

FIGURE 7. Backscattered electron (BSE) images and SIMS $\delta^{34}S$ results of framboidal pyrite in Sample 1. SIMS $\delta^{34}S$ data presented in different colors based on petrographic textures. Yellow = within framboids; red = outside framboids; white = framboid edge. Detailed views of image **a** can be found in Slides 25–32 of the online Appendix[1] 2. Note that the $\delta^{34}S$ data measured from the pyrite cements outside the framboids (red or white) are significantly higher than those measured within the pyrite framboids (yellow). For more detailed SEM-SIMS results of this sample, see online Appendix[1] 2.

sausage-shaped texture of pyrite is largely inherited from that of the hosting Mn-rich carbonates (Appendix[1] 3).

Under BSE (typically with decreased color brightness), pyrite in Sample 2 shows at least two textures: individual pyrite framboids and lacy pyrite overgrowth/cements (Figs. 11, 12l, 13, and 14). In contrast with the framboidal pyrite in Sample 1 that shows a wide range in size (up to 30 μm in diameter), all the pyrite framboids in Sample 2 are smaller than 7 μm in

diameter (Appendix[1] 3).

The pyrite framboids and the lacy pyrite "veins" within an overgrowth are typically brighter (higher average atomic number) than the pyrite overgrowth under BSE (Figs. 11a, 11i, 13h, 13g, 13l, and 14; Appendix[1] 3). The detailed causes of this zoning are still unclear, but preliminary EPMA shows that the darker pyrite overgrowths yield lower analytical totals than the brighter pyrite framboids and lacy pyrite veins (Appendix[1] 8), suggesting that porosity or C/N-rich inclusions may have played a role in causing this effect.

Paragenesis. Detailed SEM investigation allows reconstruction of the paragenesis of different minerals in Sample 2. Multiple lines of evidence suggest that pyrite in this sample postdates rhodochrosite and illite. Supporting evidence includes: (1) petrographic overviews showing that pyrite grains in this sample are nodule- or sausage-shaped and preserved exclusively within rhodochrosite lamina (Fig. 9); (2) rhodochrosite granules with ring-shaped pyrite cements (Fig. 10); (3) pyrite with abundant inclusions of granular rhodochrosite (Fig. 11); (4) magnified views showing that pyrite in Sample 2, either individual pyrite framboids (Figs. 13a–13d) or framboidal pyrite with lacy pyrite overgrowths (Figs. 13e–13l), are replacing both rhodochrosite and illite. More detailed petrographic evidence is available in the online Appendix[1] 3. Taken together, these textures indicate that pyrite in this sample is relatively late, postdating the mineralization of rhodochrosite and illite.

SIMS results. Both disseminated pyrite framboids and lacy pyrite overgrowth have been analyzed for $\delta^{34}S$ by SIMS. In total, 28 spots were analyzed in Sample 2 (Appendix[1] 3). The range of SIMS $\delta^{34}S$ values is from +56.3 to +60.4‰. These values are remarkably homogeneous regardless of heterogeneous textures under BSE (Figs. 14, 22, and 23; Table 1).

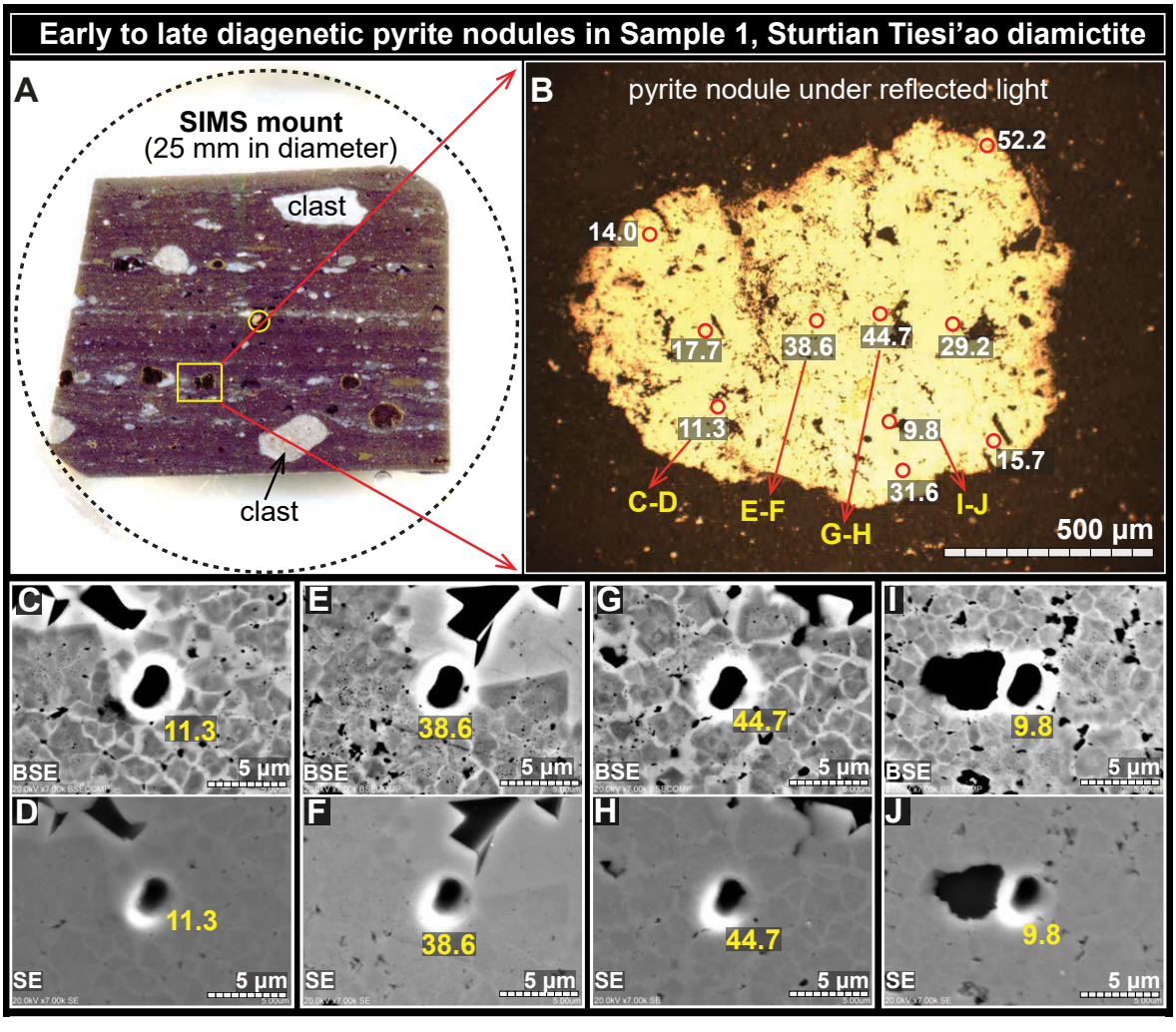

FIGURE 8. Pyrite nodules in Sample 1. (**a**) 25 mm-diameter SIMS mount of Sample 1 with in-house pyrite standard UWPy-1 (marked as yellow circle) mounted in the center. (**b**) A studied pyrite nodule under reflected light. SIMS $\delta^{34}S$ values showing heterogeneous values. Note that the symbols (red circles) are much larger than the actual SIMS spots (2 μm in diameter). (**c–d, e–f, g–h,** and **i–j**) Coupled BSE–SE images of the analyzed spots. The spots are all shown in the center. Note that the pyrite nodule is very heterogeneous under BSE, representing progressive pyrite mineralization during a spectrum of diagenesis. Abbreviations: BSE = backscattered electron; SE = secondary electron. For more detailed SEM-SIMS results of this sample, see online Appendix[1] 2.

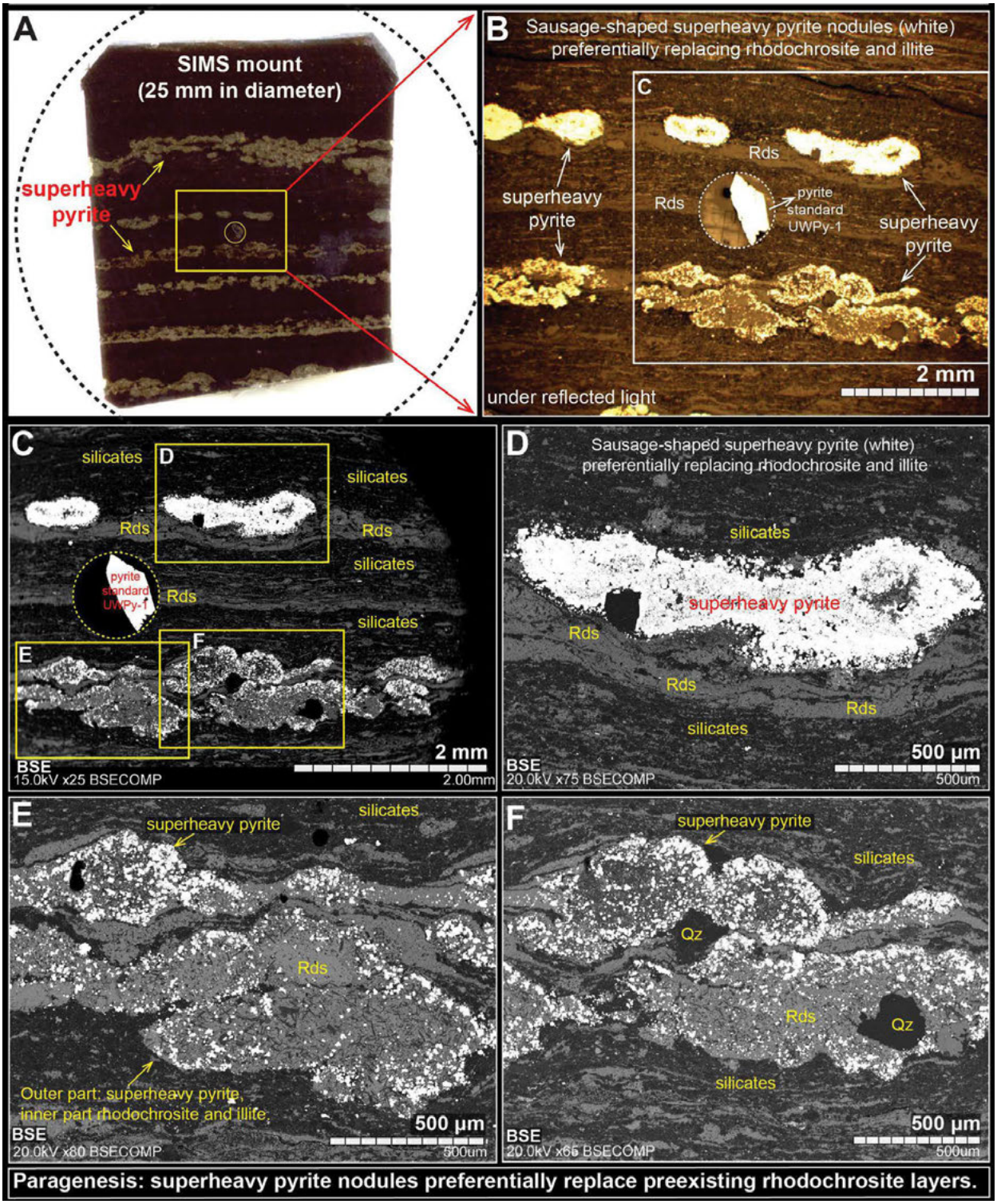

FIGURE 9. Petrographic observations of Sample 2. (**a**) SIMS mount of Sample 2 showing abundant sausage-shaped pyrite nodules within Mn-rich carbonates. (**b** and **c**) Sausage-shaped superheavy pyrite aggregates partially replacing rhodochrosite. Image **b** taken under reflected light; Image **c** taken with BSE. Note that some sausage-shaped textures have superheavy pyrite around margins and relict rhodochrosite in the center. (**d–f**) Magnified BSE views of the sausage-shaped textures. Note that superheavy pyrite in **e** and **f** is partially replacing the preexisting rhodochrosite (Rds) lamina, with superheavy pyrite concentrated at the margins and rhodochrosite in the core of the sausages. For more detailed petrographic images of this sample, see online Appendix[1] 3.

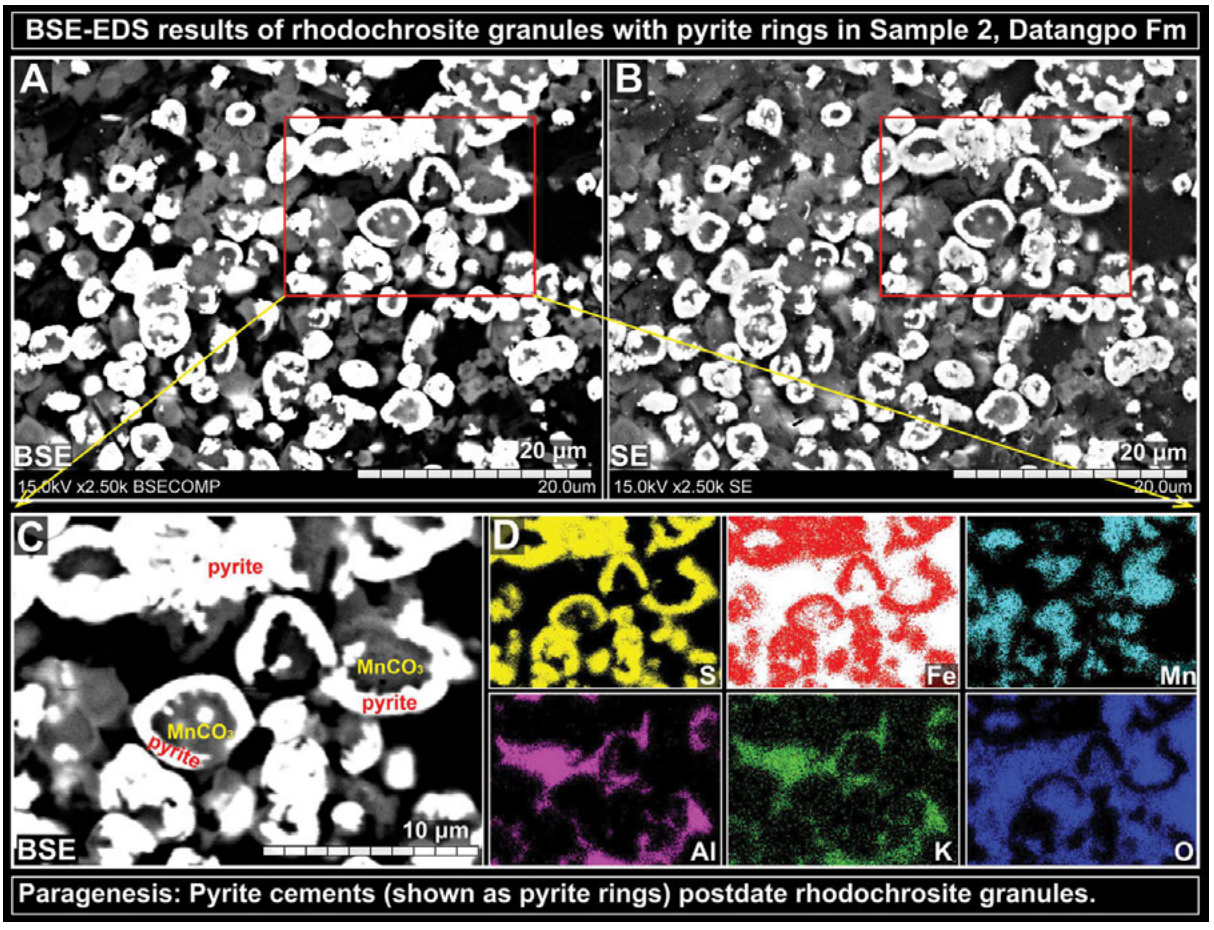

FIGURE 10. SEM-EDS results of rhodochrosite granules with pyrite rings in Sample 2. (**a** and **b**) Matched views under BSE and SE, respectively. (**c**) Magnified BSE view of marked zones in **a** and **b**. (**d**) ESD elemental mapping of the view in **c**. Black or white background colors in the EDS images represent zero detection. For more petrographic images of this sample, see online Appendix[1] 3. Abbreviations: BSE = backscattered electron; SE = secondary electron; EDS = energy-dispersive X-ray spectrometry. For more petrographic images of this sample, see online Appendix[1] 3.

Sample 3 (Hy31, black shale)

SEM petrography. In Sample 3, no framboidal pyrite was found. Instead, pyrite mostly shows disseminated subhedral grains ranging from 20 to 100 μm in size (Figs. 15 and 16; Appendix[1] 4). It is notable that some pyrite grains are relatively large (up to 2 mm), composed of multiple micrometer-size pyrite sub-grains cemented by later-stage pyrite (Fig. 17; Appendix[1] 4). The micrometer-size pyrite sub-grains mimic the disseminated pyrite in the shale matrix, suggesting that pyrite sub-grains were formed earlier, and were then cemented by pervasive pyrite cement.

SIMS results. A total of 108 spots were measured by SIMS from Sample 3 (Appendix[1] 4), including both micrometer-size sub-grains (n = 85; Figs. 16 and 17) and millimeter-size pyrite cements (n = 23; Fig. 17). The range of the SIMS $\delta^{34}S$ values of individual pyrite sub-grains is from +60.3 to +71.2‰, with an average value of +66.3‰ (Figs. 16, 17, 22, and 23). The pyrite cements show homogeneous $\delta^{34}S$ values ranging from +60.2 to +64.8‰ (Figs. 17, 22, and 23). Notably, the micrometer-scale SIMS $\delta^{34}S$ analysis reveals a consistently decreasing $\delta^{34}S$ trend from the core (ca. +70‰) to the edge (ca. +60‰) of individual pyrite grains (Figs. 16 and 17; Appendix[1] 4).

Sample 4 (Hy1, shale)

SEM petrography. Two pyrite textures are found in Sample 4 (Fig. 18–21; Appendix[1] 5). The first type of pyrite, named "pyrite flowers" here, is characterized by framboidal pyrite cores with a zoned pyrite overgrowth (Figs. 18c and 19). The second texture is characterized by "Fe-oxide coronas" with pyrite cores and thin pyrite rims (Figs. 18d, 20, and 21). The pyrite cores inside the "Fe-oxide coronas" typically show framboidal textures in the center with fibrous textures in the outer surface (Figs. 18d, 20, and 21), which was likely marcasite initially (e.g., Zhang et al. 2014; Lin et al. 2016a).

SIMS results. Both pyrite textures have been analyzed by SIMS in this study. A total of 25 spots were analyzed in the "pyrite flowers" and 21 spots were analyzed in the pyrite cores of the "Fe-oxide coronas" (Fig. 19; Appendix[1] 5). For the first time, a bimodal distribution of $\delta^{34}S$ values is found within a single sample at centimeter-scale (Figs. 22 and 23). SIMS $\delta^{34}S$ results of the "pyrite flowers" show remarkably homogeneous and high values ranging from +59.9 to +62.8‰, regardless of zoned textures under BSE (Figs. 18c, 19, 22, and 23; Appendix[1] 5). In contrast, the pyrite cores within the "Fe-oxide coronas" show a much wider range with much lower $\delta^{34}S$ values, ranging

from ca. +16.6 to ca. +32.7‰ with an average value of +22.2‰ (Figs. 18d and 20–23; Appendix[1] 5).

Pyrite $^{32}S^{1}H/^{32}S$ values

During SIMS analysis, mass $^{33}(^{32}S^{1}H^{-})$ was also measured to check the irregularity of each spot. The mean value of $^{32}S^{1}H/^{32}S$ in UWPy-1 is 4.6E-4 during the three sessions. Among the studied four samples, only pyrite analyses of Sample 3 show similar level (mean: 7.4E-4) of $^{32}S^{1}H/^{32}S$. Notably, pyrite analyses of Samples 1, 2, and 4 show $^{32}S^{1}H/^{32}S$ values that are around two orders of magnitude higher than those of the UWPy-1 standard indicating the presence of a second hydrogen-bearing phase (Appendix[1] 6).

Except for the $\delta^{34}S$ values analyzed from a single pyrite nodule in Sample 1 that show a weak correlation with the $^{32}S^{1}H/^{32}S$ values, most of the measured $\delta^{34}S$ values in this study do not show apparent correlation with corresponding $^{32}S^{1}H/^{32}S$ values (Appendix[1] 6). For example, $\delta^{34}S$ data measured from Sample 4 show a bimodal distribution (mean $\delta^{34}S$ of superheavy pyrite flowers: +61.6‰; mean $\delta^{34}S$ of pyrite cores within Fe-oxide coronas: +22.2‰), but all these data are coupled with $^{32}S^{1}H/^{32}S$ values (mean $^{32}S^{1}H/^{32}S$ of superheavy pyrite flowers: 9.7E-3; mean $^{32}S^{1}H/^{32}S$ of pyrite cores within Fe-oxide coronas: 1.3E-2) that are around two orders of magnitude higher than the mean $^{32}S^{1}H/^{32}S$ values of the UWPy-1 standard. It is also notable that among superheavy pyrites, $^{32}S^{1}H/^{32}S$ values can be very different. For example, superheavy pyrites in Samples 2 and 4 show $^{32}S^{1}H/^{32}S$ values that are two orders of magnitude higher than the mean $^{32}S^{1}H/^{32}S$ values of the UWPy-1 standard, while superheavy pyrite in Sample 3 show $^{32}S^{1}H/^{32}S$ values that are similar to those measured from UWPy-1.

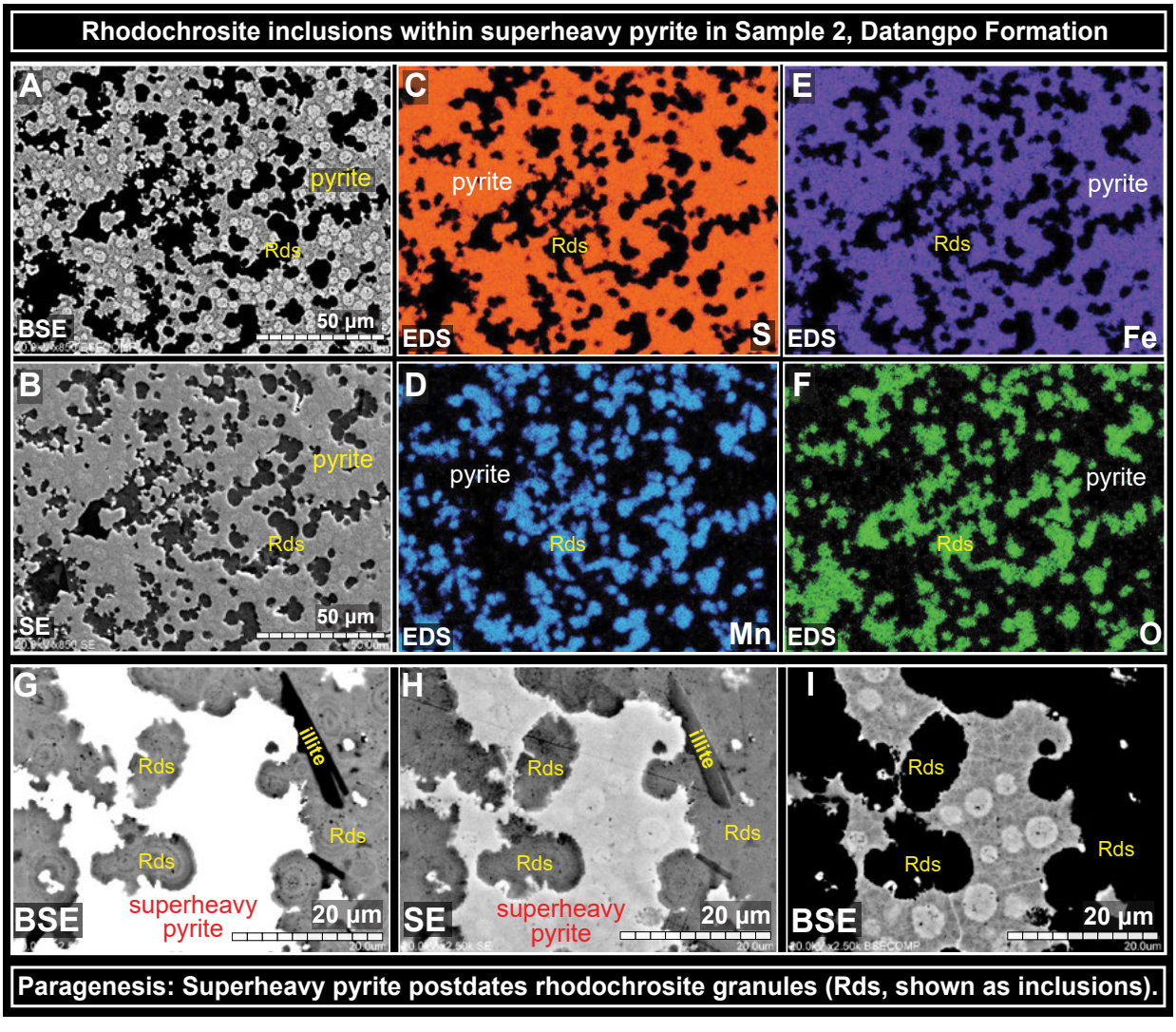

Figure 11. SEM-EDS views of rhodochrosite inclusions within the superheavy pyrite in Sample 2. (**a–f** and **g–i)** Matched views of SEM and elemental maps by EDS. Black background in EDS element maps represents zero detection. The BSE images of superheavy pyrite are made with decreased color contrast (**a** and **i)** to show heterogeneous textures with pyrite framboids (brighter under BSE) and lacy pyrite overgrowths (darker under BSE). Note metasomatic corrosion textures and the massive rhodochrosite inclusions that are not yet replaced by superheavy pyrite, suggesting superheavy pyrite postdates rhodochrosite. Abbreviations: BSE = backscattered electron; SE = secondary electron. For more detailed SEM-EDS images of this sample, see online Appendix[1] 3.

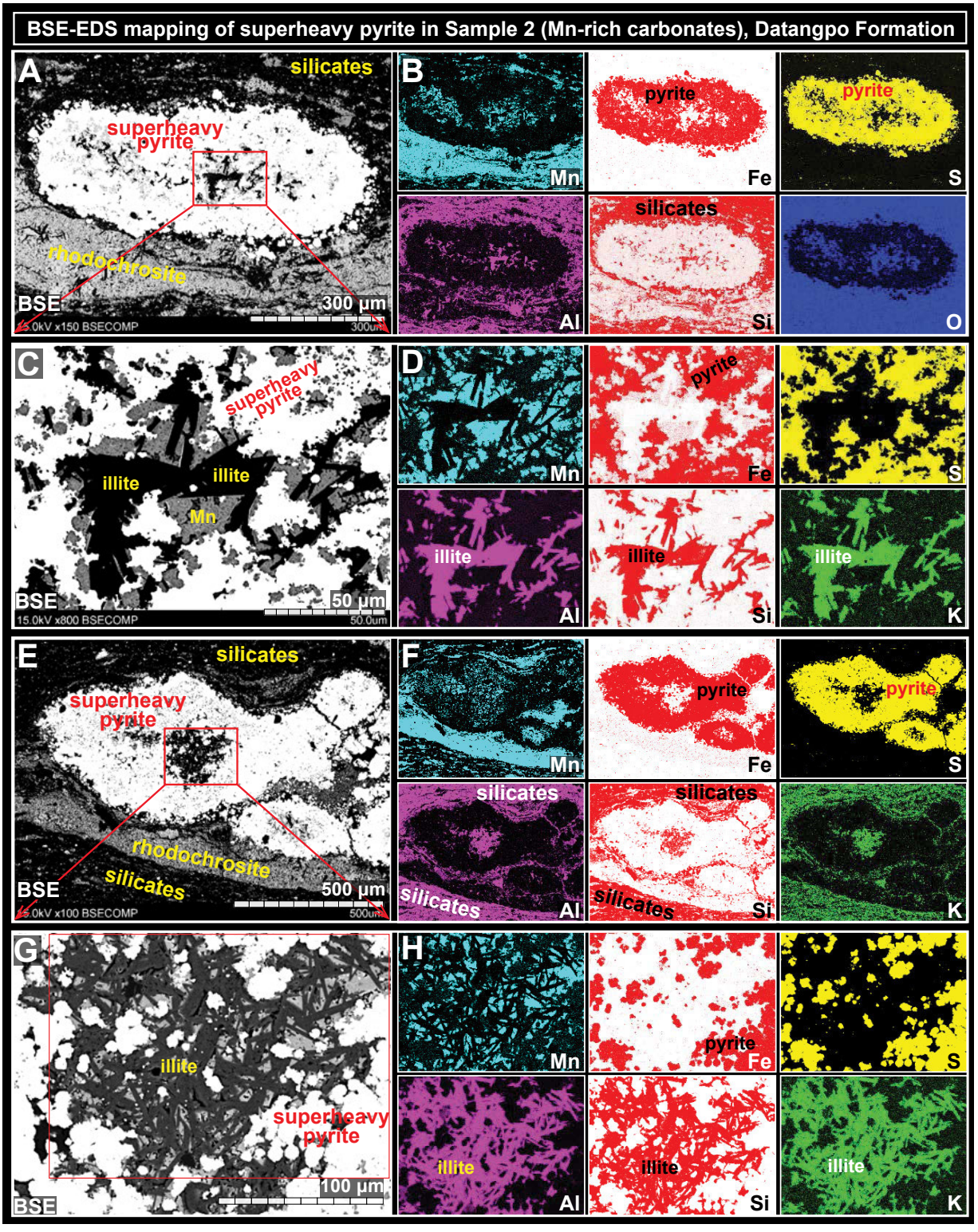

FIGURE 12A. SEM-EDS results of superheavy pyrite in Sample 2. Images **a–b**, **c–d**, **e–f**, **g–h**, and **k/l–m** showing pairs of matched views of BSE and EDS, respectively. Black or white background colors in EDS images represent zero detection. Abbreviations: BSE = backscattered electron; EDS = energy-dispersive X-ray spectrometry.

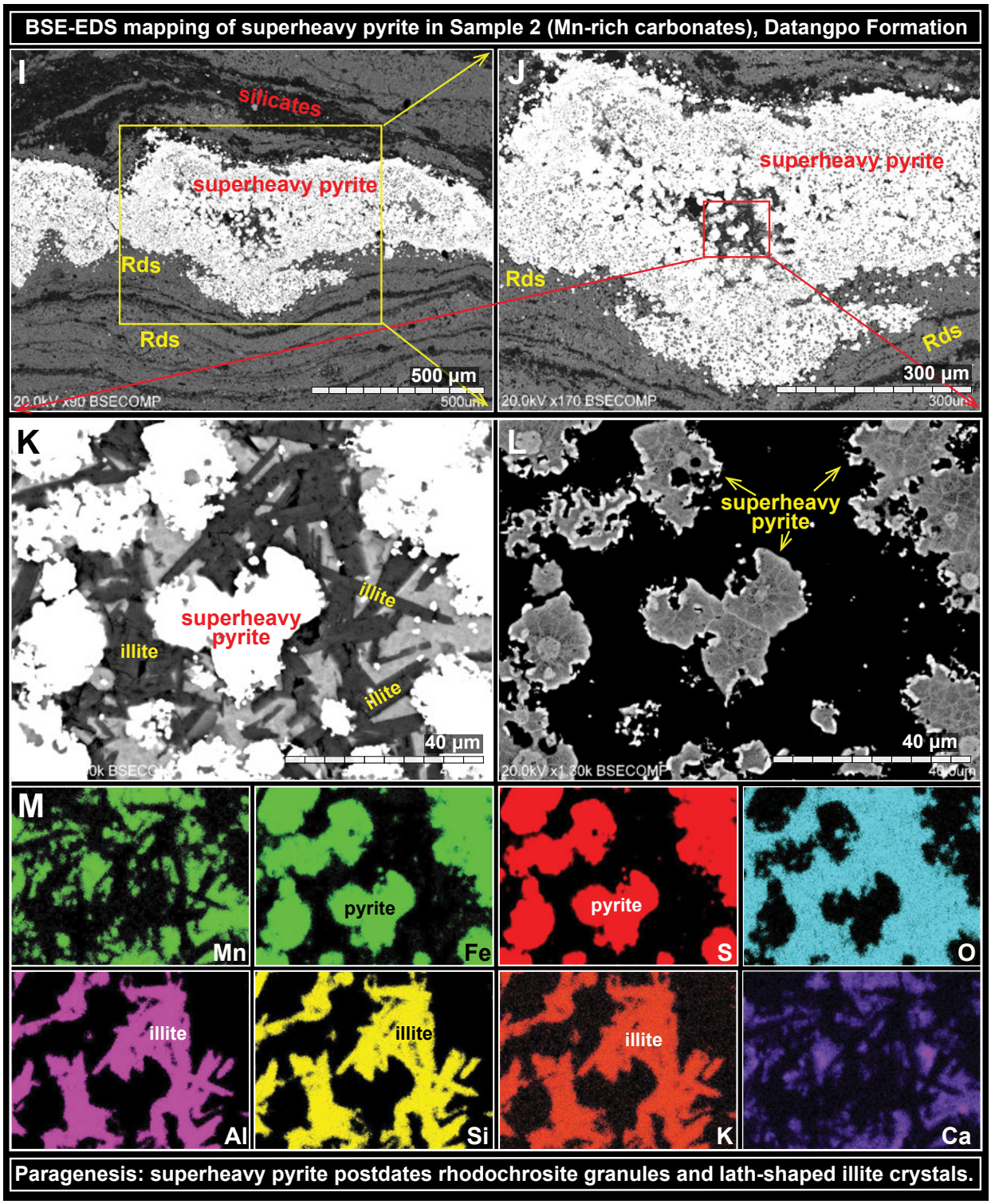

FIGURE 12B. Note that superheavy pyrite in Sample 2 showing the replacement of preexisting rhodochrosite (Rds) and lath-shaped illite crystals. For more detailed SEM-EDS images of this sample, see online Appendix[1] 3.

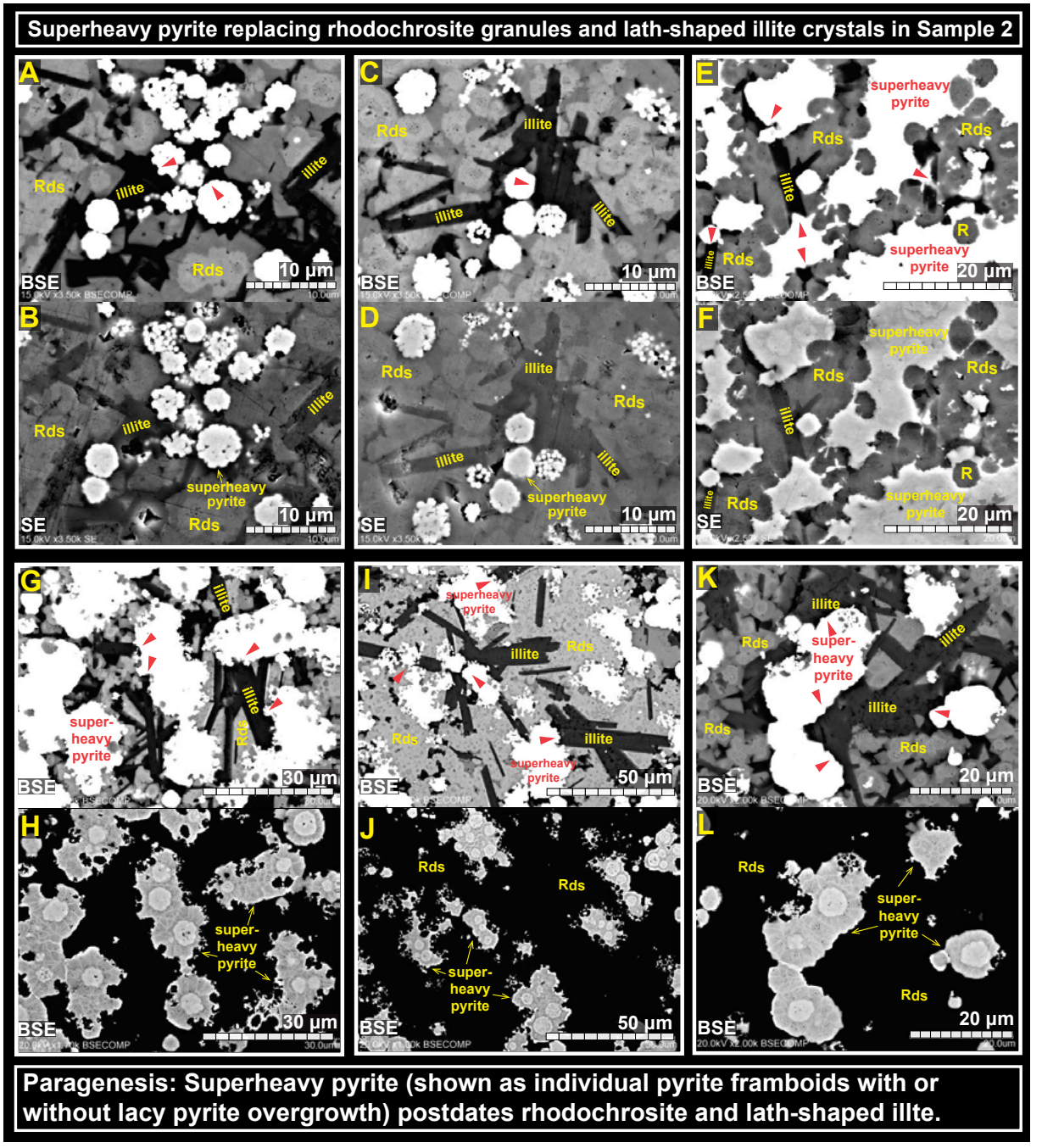

FIGURE 13. Backscattered electron (BSE) images of Sample 2 showing the replacement (marked by red arrows) of preexisting rhodochrosite granules and lath-shaped illite crystals by superheavy pyrite. Images **a–b**, **c–d**, and **e–f** showing individual pairs of BSE and SE images of the matched views, respectively. Images **g–h**, **i–j**, and **k–l** showing BSE images of the same view but in different color contrast. (**a–d**) Individual pyrite framboids (without lacy pyrite overgrowth) replacing rhodochrosite and illite. (**e–l**) Pyrite framboids with lacy pyrite overgrowth replacing rhodochrosite and illite. Note the irregular pyrite boundary showing metasomatic corrosion textures. Rhodochrosite (Rds or R) inclusions in **e** and **f** also suggest that superheavy pyrite postdate rhodochrosite. Abbreviations used: BSE = backscattered electron; SE = secondary electron. For more detailed SEM descriptions of this sample, see online Appendix[1] 3.

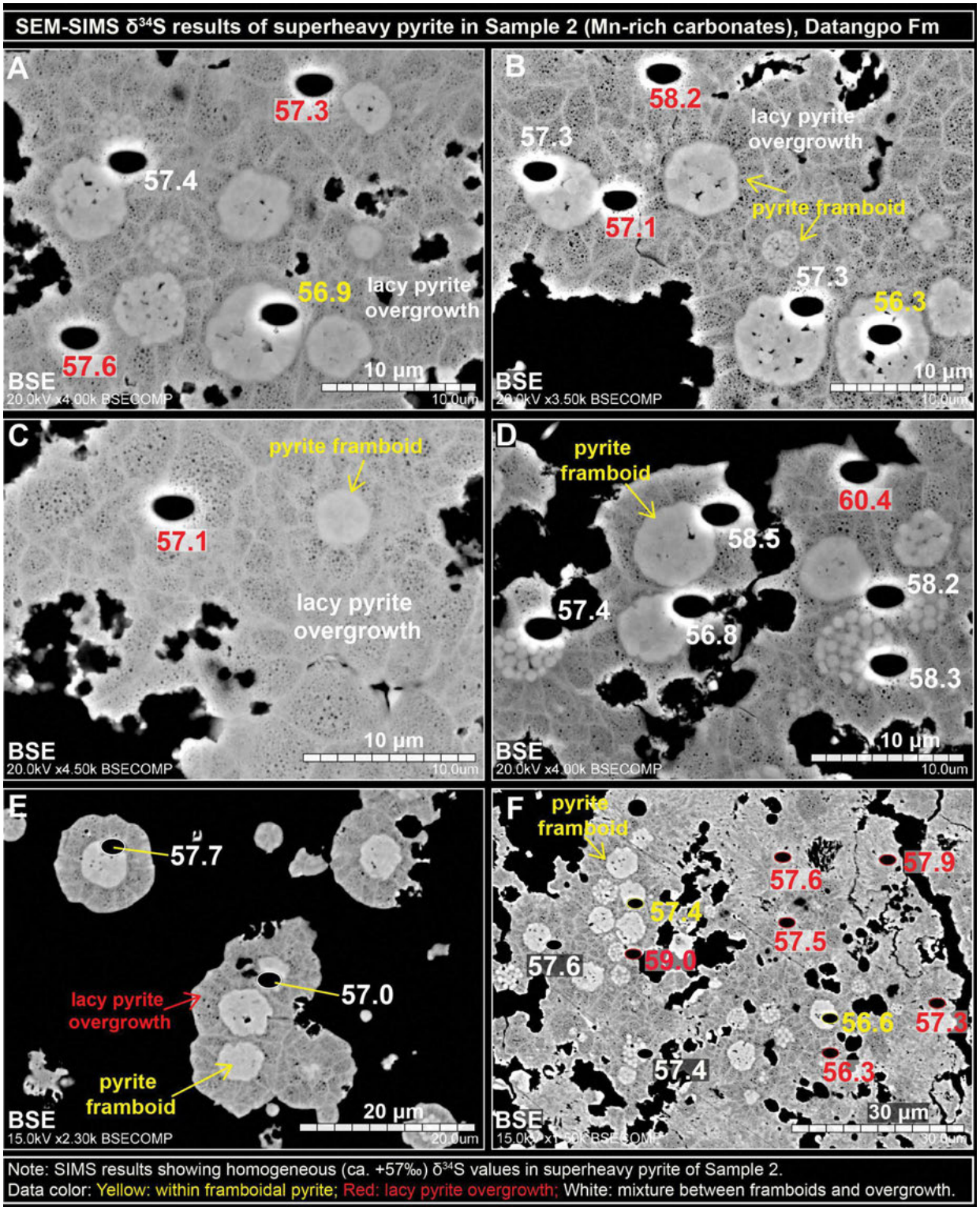

FIGURE 14. BSE images with 2 μm SIMS pits in superheavy pyrite in Sample 2. SIMS $\delta^{34}S$ data (‰ V-CDT) presented in different colors based on different textures. Yellow = within framboids; red = lacy pyrite overgrowth; white = mixture between pyrite framboids and pyrite overgrowth. Superheavy pyrite in this sample shows heterogeneous textures with pyrite framboids (brighter under BSE) and lacy pyrite overgrowth (darker under BSE) and metasomatic corrosion textures. Note the remarkably homogeneous $\delta^{34}S$ data regardless of heterogeneous petrographic textures. For more detailed SEM-SIMS data of this sample, see online Appendix[1] 3.

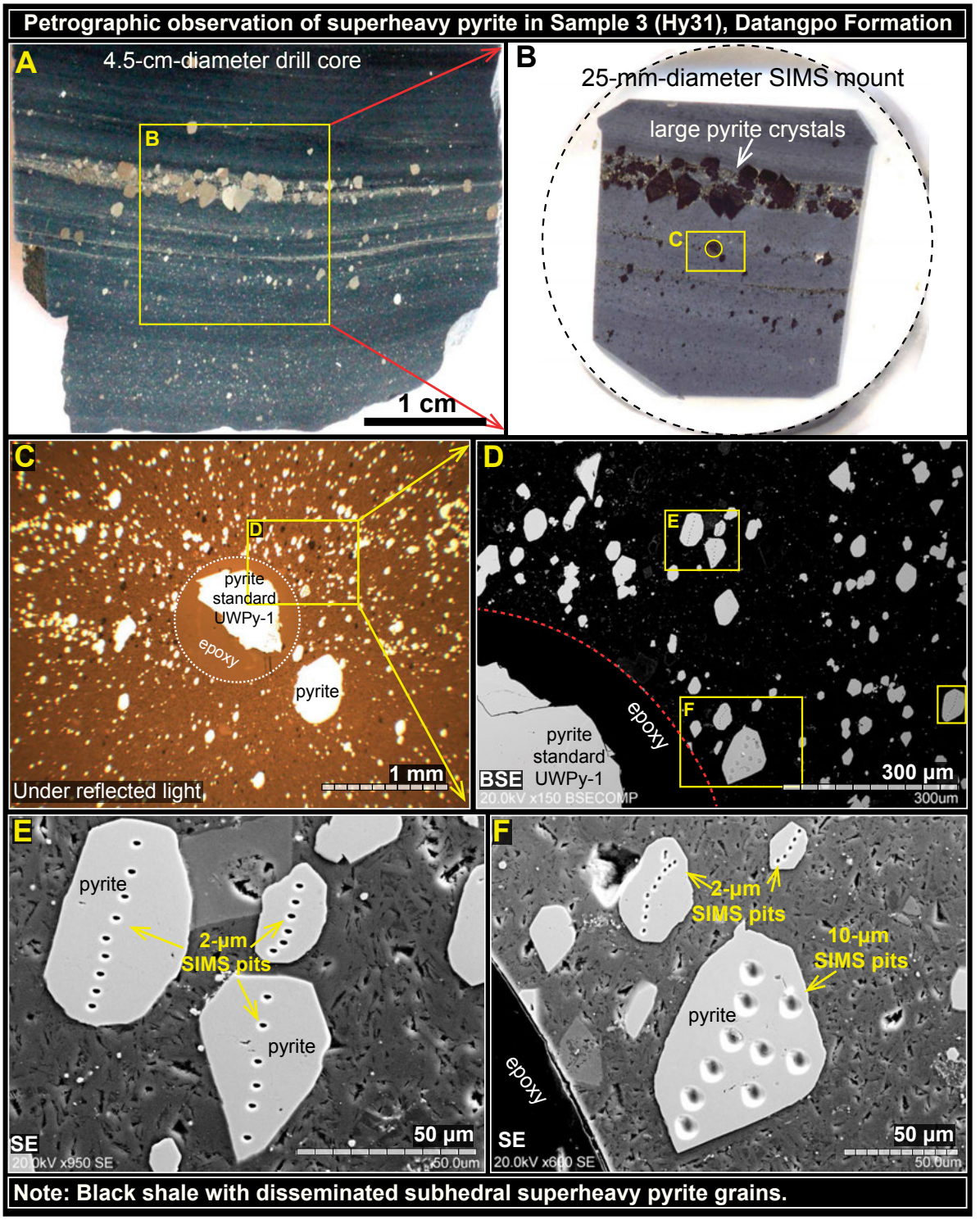

FIGURE 15. Petrographic observations of Sample 3. (**a**) A drill core section of Sample 3 showing abundant subhedral pyrite. (**b**) SIMS mount of Sample 3. (**c**) A magnified view of Sample 3 under reflection light (RL) showing disseminated subhedral pyrite grains in shale. (**d**) BSE image of the marked area in **c**. Analyzed pyrite grains in this study are marked by yellow dash boxes. Magnified views of these marked pyrite grains can be found in Figure 16 and the online Appendix[1] 4. (**e** and **f**) SE images of the analyzed domains in **d**. SIMS pits of either 2 or 10 μm in diameter are shown on the analyzed pyrite grains. Abbreviations: BSE = backscattered electron; SE = secondary electron. For more detailed SEM descriptions of this sample, see online Appendix[1] 4.

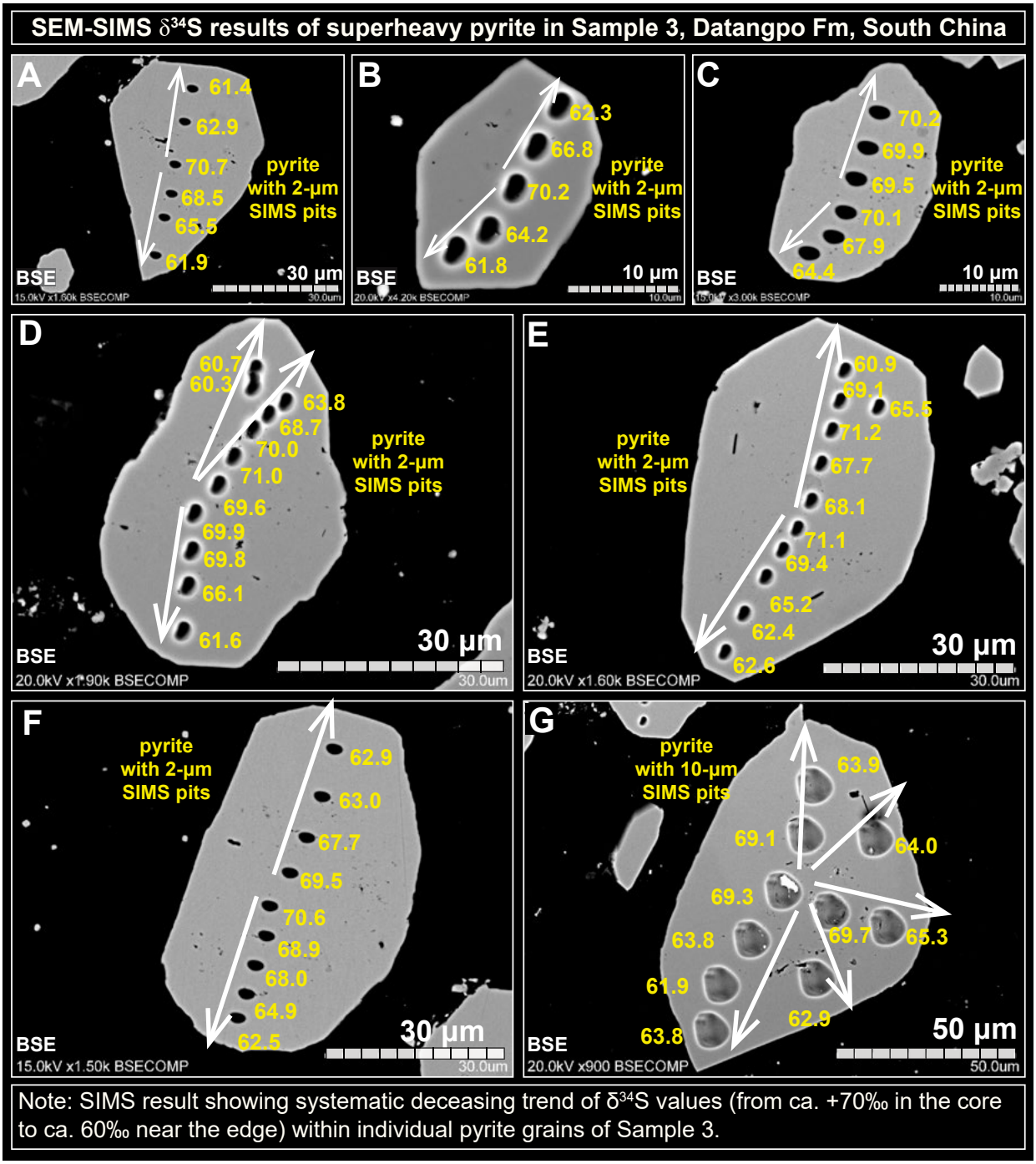

FIGURE 16. SEM-SIMS results of Sample 3. Note the consistent decreasing trend (white arrows) of $\delta^{34}S$ values from the core (ca. +70‰) to the edge (ca. +61‰) of the individual pyrite grains. For more detailed SEM-SIMS results of this sample, see online Appendix[1] 4.

Integrated SEM-SIMS results show that the $^{32}S^{1}H/^{32}S$ values correlate with the pyrite textures under BSE. Pyrites in Samples 1, 2, and 4 show strong heterogeneity in brightness under BSE and have relatively high $^{32}S^{1}H/^{32}S$ values, while pyrites in Sample 3 show relatively homogeneous brightness under BSE and have relatively low $^{32}S^{1}H/^{32}S$ values. It is possible that fluid inclusions or organic matter inclusions that are rich in hydrogen (leading to higher $^{32}S^{1}H/^{32}S$ values) within pyrite in Samples 1, 2, and 4 may have played a role in the BSE brightness and $^{32}S^{1}H/^{32}S$ values.

In summary, the $^{32}S^{1}H/^{32}S$ values measured during the SIMS sessions provide valuable information on the studied pyrite.

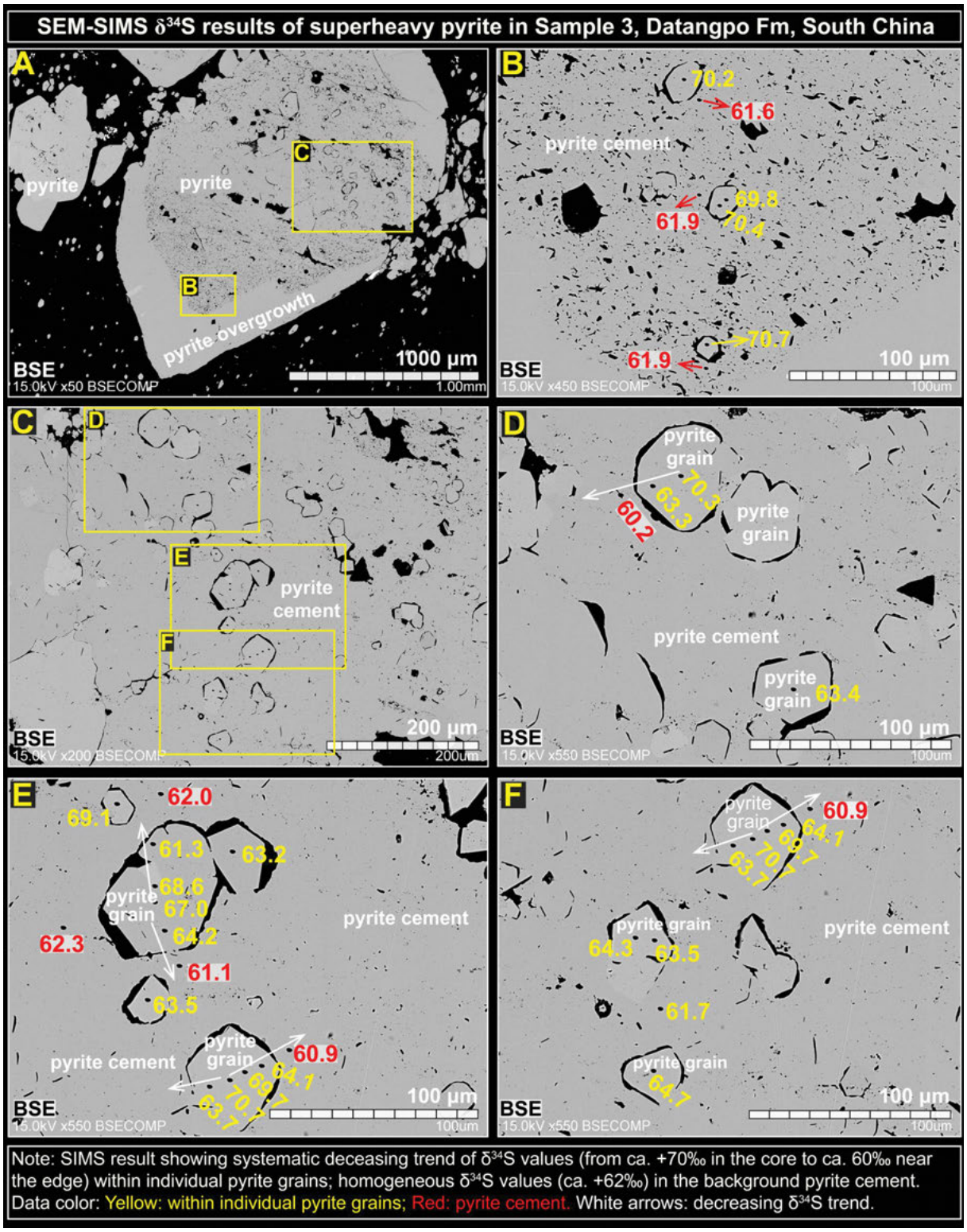

FIGURE 17. SEM-SIMS results of domains in Sample 3. (**a**) Large pyrite grains with multiple smaller pyrite grains cemented inside. (**b–f**) Magnified views of marked areas in **a** and **c** showing individual pyrite grains cemented by later-stage pyrite. SIMS $\delta^{34}S$ data (‰ V-CDT) presented in different colors based on different textures. Yellow = within individual pyrite grains; red = later-stage pyrite cements. White arrows showing consistent deceasing $\delta^{34}S$ trends (ca. +70 to +60‰) from the core to the edge of individual pyrite grains. For more detailed SEM-SIMS data of this sample, see online Appendix[1] 4.

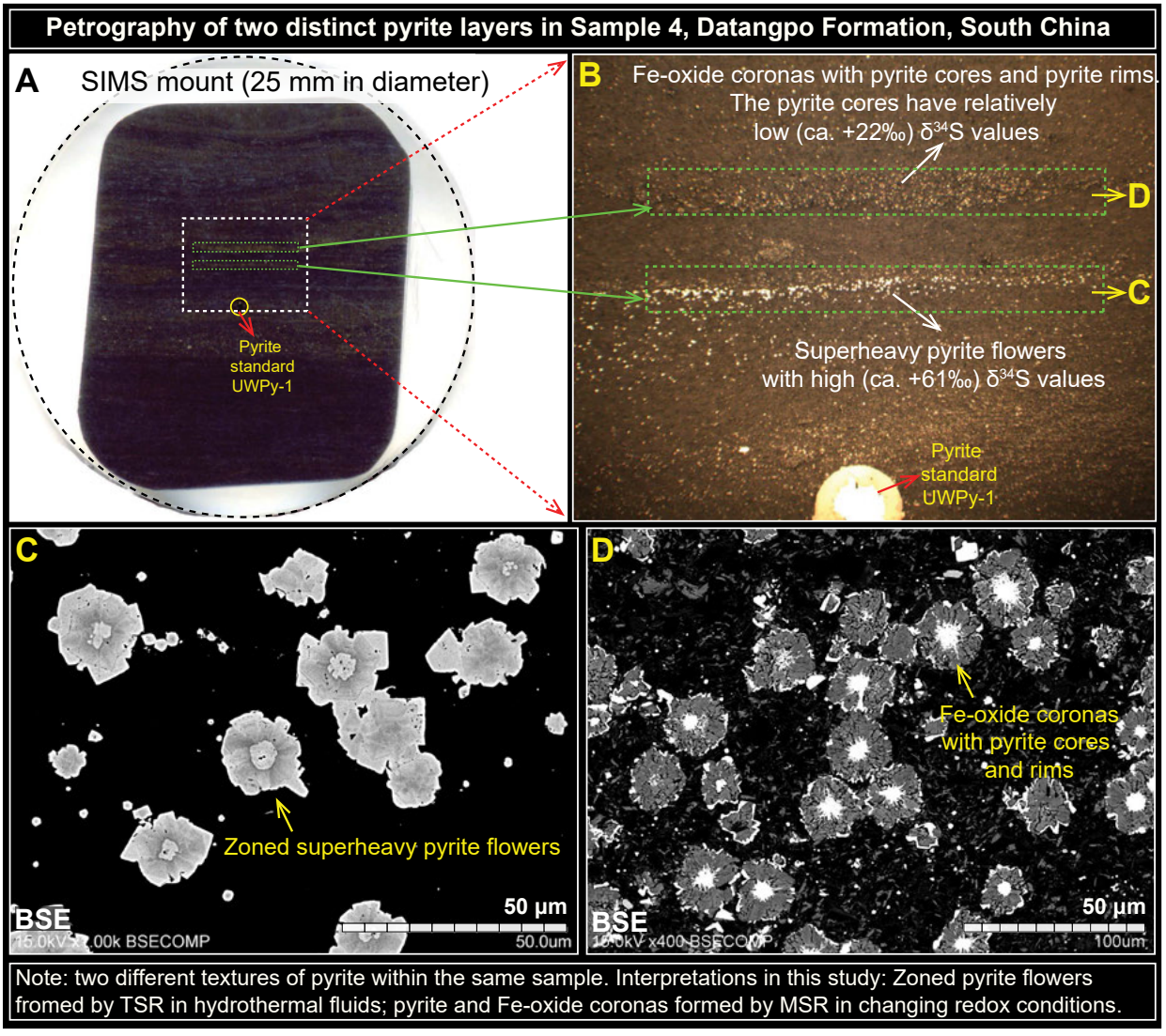

FIGURE 18. Petrographic observations of Sample 4. (**a**) SIMS mount of Sample 4. (**b**) A magnified view of the marked area in **a** showing two distinct layers of pyrite. The SIMS $\delta^{34}S$ data are also shown for convenience. (**c**) A magnified view of pyrite in the lower layer. This layer is characterized by "zoned pyrite flowers" with homogeneous and superheavy $\delta^{34}S$ values. (**d**) A magnified view of pyrite in the upper layer. This layer is characterized by "Fe-oxide coronas" with pyrite cores and pyrite rims. For more detailed SEM-SIMS data from this sample, see online Appendix[1] 5.

No apparent correlation was found between $^{32}S^{1}H/^{32}S$ and $\delta^{34}S$ values. $^{32}S^{1}H/^{32}S$ values show an overall correlation with the pyrite brightness under BSE, which we regard can be explained by the contribution of fluid or organic inclusions mixed within pyrite.

DISCUSSION

A viable model for the genesis of the studied superheavy pyrite should be able to explain sedimentological and geochemical observations at both basin and micrometer scales. We will evaluate multiple models for the superheavy pyrite below.

Superheavy pyrite formed via MSR?

All the previously published biogeochemical models for the superheavy pyrite in South China assume a biogenic origin by MSR (Liu et al. 2006; Chen et al. 2008; Li et al. 2012; Lang et al. 2016; Wu et al. 2016; Wang et al. 2017). This assumption hypothesizes that superheavy pyrite formed in the marine water column or shallow sediments with different degrees of access to seawater sulfate. However, based on detailed SIMS-SEM study, the superheavy pyrite in the Datangpo Formation is found replacing preexisting rhodochrosite and illite (Figs. 9–13), and therefore formed after deep burial.

Supporting evidence for a non-MSR origin of the Datangpo superheavy pyrite also comes from its micrometer-scale $\delta^{34}S$ patterns. Sample 2 shows remarkably homogenous $\delta^{34}S$ values regardless of heterogeneous textures (Fig. 14); Sample 3 shows a decreasing $\delta^{34}S$ trend from the core to the edge of individual pyrite grains (Figs. 16 and 17). These micrometer-scale $\delta^{34}S$ patterns are inconsistent with a MSR origin considering that progressive MSR in restricted pore waters would only increase,

instead of decrease, the pyrite $\delta^{34}S$ values. Therefore, previous models based on a MSR assumption cannot explain the textures or $\delta^{34}S$ values of studied superheavy pyrite either, and a non-MSR model is needed.

Superheavy pyrite formed in a sulfide-rich fluid flow?

It is possible that flow of a reducing hydrothermal fluid that is rich in sulfide, instead of sulfate, may have caused the mineralization of the studied superheavy pyrite. In this scenario, iron that may be available in the sediments reacts with external hydrogen sulfide and forms pyrite in the absence of simultaneous sulfate reduction. The flow of sulfide-rich fluid can be hypothesized to come from an underlying magmatic source. However, multiple lines of evidence suggest that this scenario is unlikely.

First, given the typically near-zero $\delta^{34}S_{sulfide}$ values ($0 \pm 5‰$)

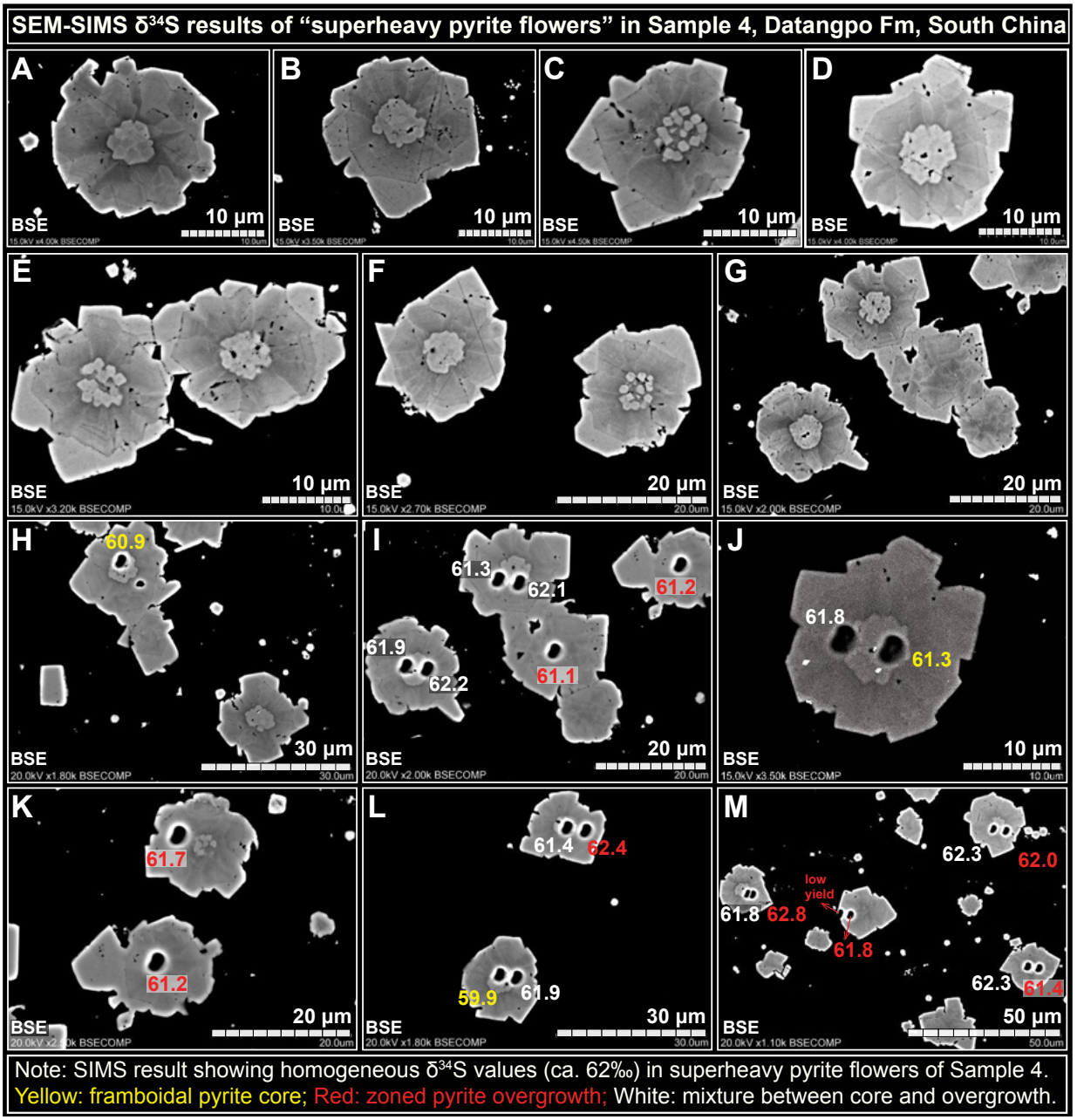

FIGURE 19. Backscattered electron (BSE) images showing SIMS $\delta^{34}S$ pits in "superheavy pyrite flowers" in Sample 4 (Hy1). The "superheavy pyrite flower" is characterized by a small framboidal pyrite core and a zoned pyrite overgrowth. SIMS $\delta^{34}S_{pyrite}$ values (‰ V-CDT) are presented in different colors based on the textures. Yellow = within framboids; red = zoned pyrite overgrowth; white = mixture between pyrite framboids and pyrite overgrowth. Note that the $\delta^{34}S$ data measured from zoned "superheavy pyrite flowers" are remarkably homogeneous. For more detailed SEM-SIMS data from this sample, see online Appendix[1] 5.

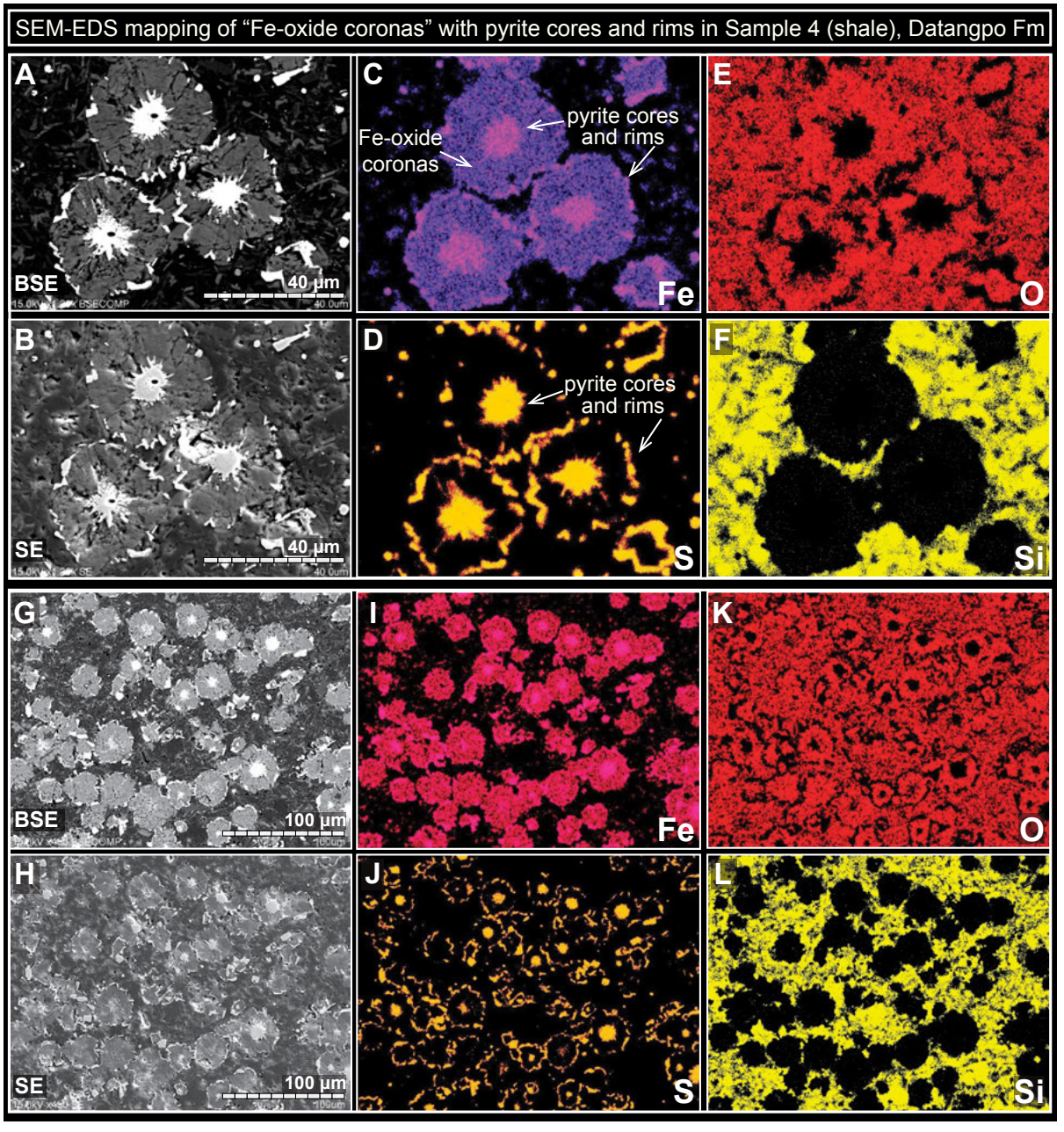

FIGURE 20. Images **a–f** and **g–l** showing SEM-EDS images and chemical maps of Fe, O, S, and Si of matched views in Sample 4. Black background in EDS images represents zero detection. Abbreviations: BSE = backscattered electron; EDS = energy-dispersive X-ray spectrometry. For more detailed SEM-EDS images from this sample, see online Appendix[1] 5.

of magmatic sulfur reservoirs (Marini et al. 2011), it would be extremely difficult for such a sulfur reservoir to generate $\delta^{34}S_{sulfide}$ values as high as +70‰ at a basinal scale in South China.

Second, a sulfide-rich source is inconsistent with the SIMS $\delta^{34}S$ data shown in Sample 3, where decreasing $\delta^{34}S$ trends with a magnitude of ca. 10‰ are consistently registered from core to edge of each individual subhedral pyrite grain (Figs. 16 and 17). A previous study shows that sulfur isotope fractionations between hydrogen sulfide and iron sulfide ($\Delta^{34}S_{FeS\text{-}H_2S}$) are small (~1‰) (Böttcher et al. 1998), in strong contrast with MSR-induced fractionation ($\Delta^{34}S_{sulfate\text{-}sulfide}$). Such small fractionation ($\Delta^{34}S_{FeS\text{-}H_2S}$) cannot readily explain the $\delta^{34}S_{pyrite}$ heterogeneity in Sample 3 revealed by the SIMS data at a micrometer scale (Figs. 16 and 17).

Third, the discovery of barite and gypsum veins or infillings in the Datangpo Formation (Xu et al. 1990; Chen and Chen 1992; He et al. 2013a, 2013b; Zhang et al. 2013; Pan et

al. 2016) indicate the involvement of sulfate-rich, instead of sulfide-rich, fluids. Therefore, based on the above discussion, it is more likely that a non-MSR type sulfate reduction caused the mineralization of the studied superheavy pyrite. We will fully explore this scenario in the next section.

Reinterpretation: Superheavy pyrite formed by thermochemical sulfate reduction

In this study, we propose that the studied superheavy pyrite formed by thermochemical sulfate reduction (TSR) in hydrothermal fluids. This revised interpretation is supported by

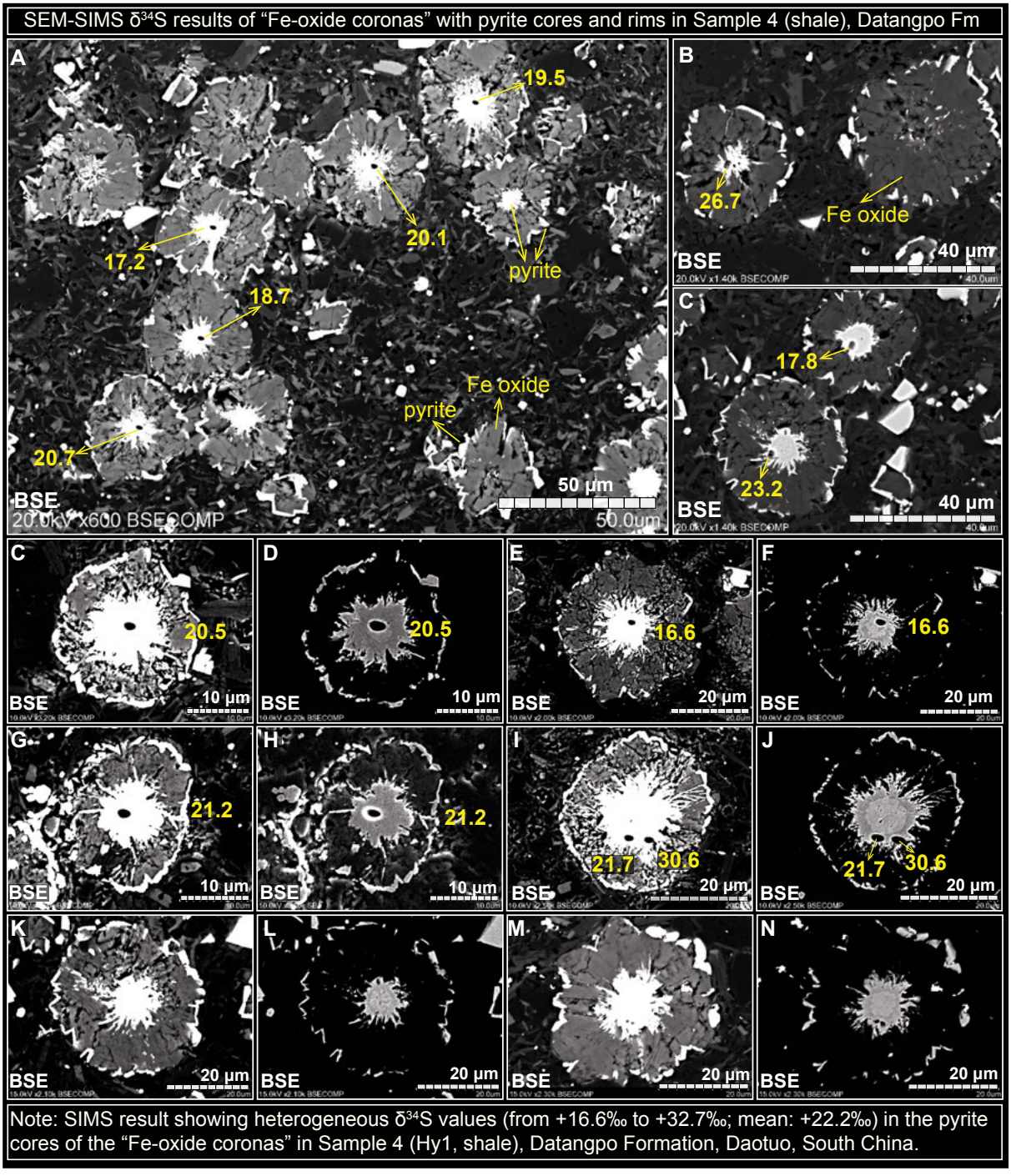

FIGURE 21. Backscattered electron (BSE) images showing SIMS $\delta^{34}S$ pits in pyrite cores inside the Fe-oxide coronas in Sample 4 (Hy1). Images **c–d**, **e–f**, **g–h**, **i–j**, **k–l**, and **m–n** show matched BSE views with different color contrast. The Fe-oxide corona surrounds a framboidal pyrite core with a fibrous surface (likely marcasite initially) and also has a thin pyrite rim. SIMS $\delta^{34}S$ values measured from the pyrite cores range from ca. +16 to +33‰. For more detailed SEM-SIMS data of this sample, see online Appendix[1] 5.

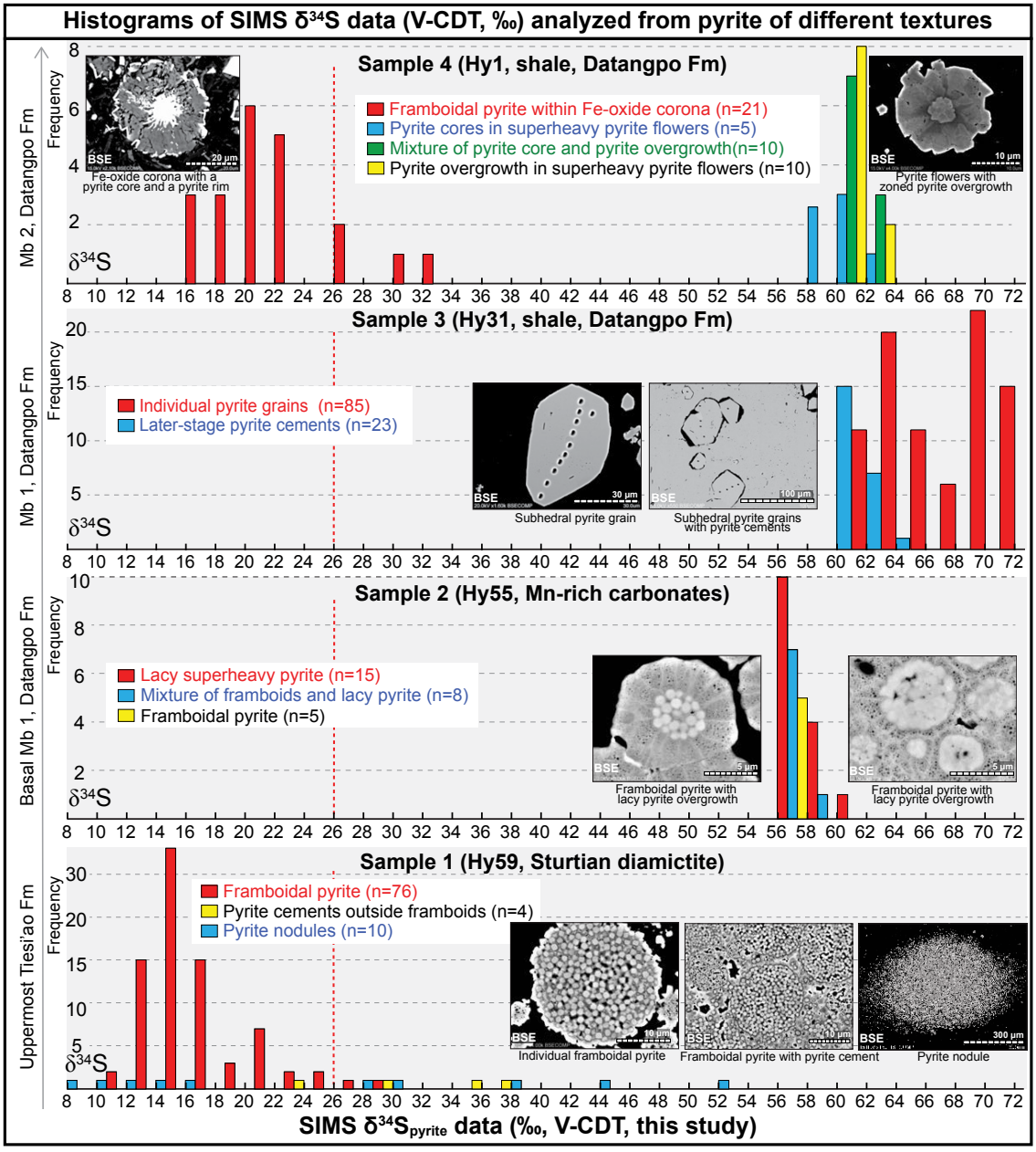

FIGURE 22. Histograms of the SIMS $\delta^{34}S$ values measured in this study. Different pyrite textures showing distinct ranges of $\delta^{34}S$. Red dash line representing the Cryogenian seawater $\delta^{34}S_{sulfate}$ value based on anhydrite analysis (Gorjan et al. 2000). Note the relatively large range of SIMS $\delta^{34}S$ data measured from Sample 1, homogeneous $\delta^{34}S$ values measured from Sample 2, remarkably high $\delta^{34}S$ values measured from Sample 3, and a notable bimodal distribution of the $\delta^{34}S$ values measured from Sample 4. See the main text for detailed discussion of these patterns and their interpreted origins. For corresponding petrographic context of all the plotted data, see online Appendices 2–5.

multiple lines of sedimentological and geochemical evidence as listed below.

Superheavy pyrite associated with ancient faults. In South China, the superheavy pyrite in the Datangpo Formation is found closely associated with ancient faults (Wu et al. 2016). This distinct pattern suggests that the genesis of the Datangpo superheavy pyrite was controlled by external fluids that flowed along the faults. It is possible that an external sulfate-rich hydrothermal fluid intruded the Datangpo Formation along ancient faults, and caused the mineralization of the superheavy pyrite via TSR.

Superheavy pyrite associated with Mn-rich carbonates. In South China, most of the superheavy pyrites were found near or within the Mn-rich carbonate intervals in the basal Datangpo Formation. Detailed petrographic investigation in this study shows preferential replacement of carbonate by superheavy pyrite (Figs. 9–13; Appendix[1] 3). Given that TSR is a process

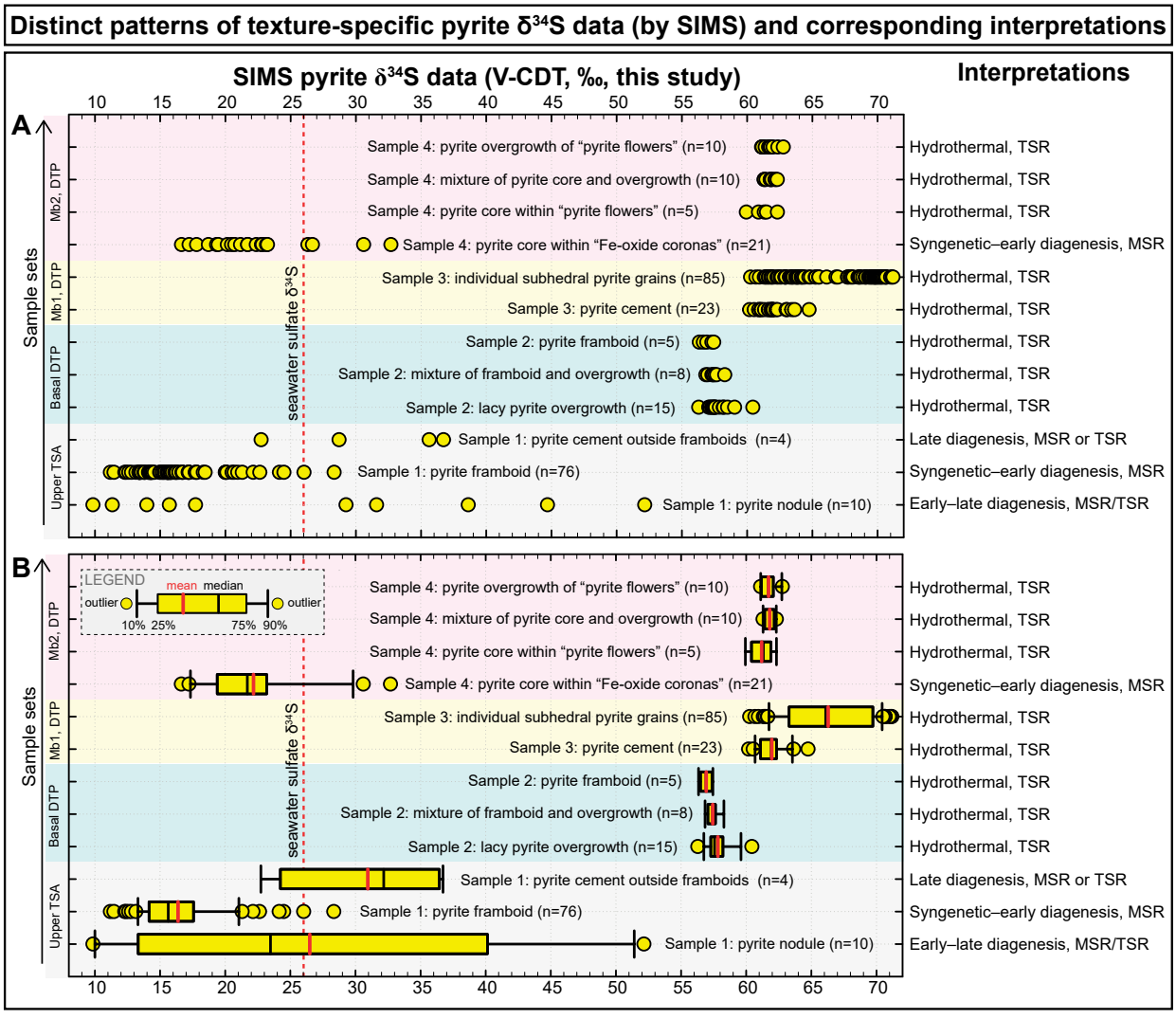

FIGURE 23. (**a**) Individual data points and (**b**) box plots of the SIMS $\delta^{34}S$ values measured in this study. Numbers in parentheses representing the amount of data analyzed by SIMS in this study. Red dash line representing the Cryogenian seawater $\delta^{34}S_{sulfate}$ value based on anhydrite analysis (Gorjan et al. 2000). Interpretations of the $\delta^{34}S$ values of each data set listed on the right-hand side. Abbreviations: MSR = microbial sulfate reduction; TSR = thermochemical sulfate reduction. TSA = Tiesi'ao Formation; DTP = Datangpo Formation. For corresponding petrographic context of all the plotted data, see online Appendices 2–6.

that produces hydrogen sulfide and increases pore-water acidity (Machel et al. 1995; Jiang et al. 2018), carbonate host rocks would be preferentially dissolved and then replaced by pyrite when TSR occurs (Kelley et al. 2004a). This process has also been reported in many other carbonate-dominated strata worldwide (e.g., Krouse et al. 1988; Worden and Smalley 1996; Cai et al. 2001; Biehl et al. 2016; Jiang et al. 2018). Therefore, the reinterpretation of a TSR origin for the studied superheavy pyrite is consistent with the close coupling between superheavy pyrite and Mn-rich carbonates.

Paragenesis. In contrast with MSR that dominantly occurs in the water column or shallow marine sediments (Jørgensen and Kasten 2006; Bowles et al. 2014), TSR usually occurs relatively late, typically in temperatures higher than 100 °C during deep burial diagenesis. Integrated SEM-SIMS results in Sample 2 show pervasive replacement of rhodochrosite and illite by superheavy pyrite (Figs. 9–13; Appendix[1] 3), suggesting that superheavy pyrite is a late diagenetic product. The reinterpretation of a TSR origin for the studied superheavy pyrite is consistent with independent paragenesis revealed by SEM petrography.

Barite and gypsum veins and infillings. Field observations of the Datangpo Formation show abundant textures that suggest pervasive overprint by hydrothermal fluids, including host-rock breccia, quartz veins, calcite, gypsum, and barite infillings and veins (Xu et al. 1990; Chen and Chen 1992; He et al. 2013a, 2013b; Zhang et al. 2013; Pan et al. 2016). The preservation of barite and gypsum veins indicates that the hydrothermal fluids were rich in sulfate, which would trigger TSR to occur given that organic matter is abundant in the Datangpo shale.

Homogeneous $\delta^{34}S$ in heterogeneous pyrite textures. In this study, superheavy pyrite in some samples shows remarkably homogenous $\delta^{34}S_{pyrite}$ values in zoned pyrite grains (Figs. 22 and 23). In Sample 2, the $\delta^{34}S_{pyrite}$ values of 28 SIMS spots in framboidal pyrite and lacy pyrite overgrowth range from +56.3 to +60.4‰ (Fig. 14). In Sample 4, the $\delta^{34}S_{pyrite}$ values of 25 SIMS spots in zoned "pyrite flowers" range from +59.9 to +62.8‰ (Fig. 19). Such homogeneous $\delta^{34}S_{pyrite}$ patterns are difficult to explain by MSR. Typically, MSR-derived pyrite shows considerable $\delta^{34}S$ zoning at micrometer scale due to a biogenic nature of MSR and the effect of Rayleigh fractionation in an increasingly restricted pore water environment (Kohn et al. 1998; Williford et al. 2011). Alternatively, it is likely that these relatively invariant $\delta^{34}S_{pyrite}$ values result from TSR in hydrothermal fluids. The superheavy pyrite of different textures may have precipitated in response to a hydrothermal fluid flow when it intruded into the host rocks.

Decreasing $\delta^{34}S$ trend from core to edge of individual pyrite grains. In this study, micrometer-scale $\delta^{34}S$ analysis reveals decreasing $\delta^{34}S$ trends in core-to-edge traverses of individual pyrite grains from Sample 3 (Figs. 16 and 17). This phenomenon is inconsistent with MSR, which typically leads to an increasing trend at micrometer scales. Alternatively, the core-to-rim traverses in Sample 3 can be explained by TSR when the temperature of the hydrothermal fluid cools. Lab experiments on kinetic sulfur isotope fractionation during TSR have demonstrated that as temperature decreases, $\Delta^{34}S_{sulfate\text{-}sulfide}$ would increase, and consequently $\delta^{34}S_{pyrite}$ would decrease (Kiyosu and Krouse 1990). As a result, a gradient with decreasing $\delta^{34}S_{pyrite}$ values would be recorded in individual TSR-derived pyrite grains.

Varying $\delta^{34}S_{pyrite}$ at a basin scale. Published chemostratigraphic $\delta^{34}S_{pyrite}$ profiles of the Datangpo Formation at different sections in South China show remarkably different values (Fig. 1) (Li et al. 1999a, 2012; Zhou et al. 2013; Zhu et al. 2013; Wu et al. 2015a, 2016; Lang 2016). For example, $\delta^{34}S_{pyrite}$ values in the lower Datangpo Formation at the Yangjiaping section range from +20 to +30‰, while $\delta^{34}S_{pyrite}$ values of the correlative Minle section range from +40 to +65‰ (Li et al. 2012). These different $\delta^{34}S_{pyrite}$ values among different sections have been interpreted to result from a stratified ocean controlled by dynamic influx of sulfate and nutrient (Li et al. 2012). However, sedimentological observations show that most of the high-$\delta^{34}S_{pyrite}$ values are associated with Mn-rich carbonate intervals and ancient faults (e.g., Minle section in Li et al. 2012), while siliciclastic-dominated sections (e.g., Yangjiaping section in Li et al. 2012) lack superheavy pyrite. We interpret this isotope-lithology pattern as resulting from preferential replacement of carbonates by superheavy pyrite via TSR. The occurrence of TSR may have caused a strong bias of superheavy pyrite preservation in carbonate-dominated intervals, and as a result, overprinted the primary $\delta^{34}S_{pyrite}$ signals.

Negative correlation between Fe content and bulk $\delta^{34}S_{pyrite}$ values. Previous studies have reported an overall negative correlation (correlation coefficient, R = –0.83, n = 8) between bulk Fe content and bulk $\delta^{34}S_{pyrite}$ values in the Datangpo Mn-rich carbonates (Fig. 15 of Wu et al. 2016). This phenomenon has been interpreted as resulting from Rayleigh distillation in seawater. However, petrographic observations in this study suggest that the bulk Fe content in the Mn-rich carbonates is mainly post-depositional pyrite replacing preexisting carbonates. Therefore, it is more likely that this overall negative correlation reflects Rayleigh distillation in hydrothermal fluids within deeply buried sediments. If correct, then TSR would be the more likely pathway of sulfate reduction instead of MSR. As TSR progressively occurs with Rayleigh distillation, $\delta^{34}S_{pyrite}$ would evolve to higher values. Therefore, the Rayleigh distillation process would be characterized by a relatively larger amount of pyrite (therefore high bulk Fe content) with relatively low $\delta^{34}S_{pyrite}$ values at the early stage and a relatively smaller amount of pyrite (therefore low bulk Fe content) with high $\delta^{34}S_{pyrite}$ values (i.e., superheavy pyrite) at the very late stage. This process can cause a broad spectrum of $\delta^{34}S_{pyrite}$ values with an overall negative correlation between bulk Fe content and bulk $\delta^{34}S_{pyrite}$ values.

Negative correlation between total organic carbon and total sulfur. An overall negative correlation (correlation coefficient, R = –0.48, n = 29) between total organic carbon (TOC) and total sulfur (TS) was reported in the Datangpo Mn-rich carbonates (Wang et al. 2017). This pattern is in strong contrast with normal marine environments where TOC and TS typically show positive correlations (Berner 1984, 1989; Cao et al. 2016). The negative TOC–TS correlation observed in the Datangpo Formation was interpreted to result from anomalous sulfur cycling during deposition (Wang et al. 2017). Petrographically, the low-TOC samples are mostly carbonates that are rich in superheavy pyrites (therefore high in TS). On the other hand, the high-TOC samples are mostly shales that have less pyrite abundance (therefore lower in TS). The new results of this study show that this overall negative TOC–TC correlation actually results from preferential replacement of carbonates by TSR-derived pyrite, therefore cannot be used to infer marine sulfur cycles.

Temperature data. Studies on vitrinite reflectance of the Datangpo Formation suggest that the Mn-rich carbonate interval experienced a maximum burial temperature of ca. 195 °C (Chen and Chen 1992; Xie et al. 1999). Studies of fluid inclusions in authigenic quartz in the Datangpo Formation yield homogenization temperatures of 173–241 °C, with an average value of 194 °C (Wang et al. 1985). These temperatures are consistent with the scenario that the Datangpo Formation experienced a hydrothermal event.

Based on the current burial depth of the studied Datangpo drill core (Samples 1, 2, 3, and 4 collected at depths of 1303.06, 1299.88, 1289.09, and 1274.14 m, respectively) and the current geothermal gradient of 10–20 °C/km in the studied region (Yuan et al. 2006), assuming the surface temperature is ca. 20 °C, the current burial temperature is likely to be ca. 33–46 °C at the sampled depths. This shows that the Datangpo Formation should have experienced a cooling event from a hydrothermal or maximum burial temperature to the current burial temperature, which is consistent with the micrometer-scale $\delta^{34}S_{sulfide}$ spatial patterns shown in Sample 3.

Source and compositions of the TSR fluids

To allow TSR to occur, sulfate-rich hydrothermal fluids and organic-rich host rocks are both required. Given the high abundance of organic matter in the Datangpo Formation, sulfate-rich hydrothermal fluid is more likely to be the controlling factor. Typically, the fluids for TSR are derived from late dissolution of preexisting sulfate minerals (e.g., gypsum, anhydrite). Therefore,

the deposition of sulfate has to predate the TSR event.

In South China, the oldest gypsum-bearing sedimentary bedding with a basin-scale distribution is the late-Ediacaran Dengying Formation. Distinct textures that point to the deposition of marine evaporites have been widely reported in this formation (Xi 1987; Siegmund and Erdtmann 1994; Lu et al. 2013; Wang et al. 2013; Duda et al. 2015; Cui et al. 2016b). Due to high solubility, evaporites in this formation are mostly shown as calcite pseudomorphs with distinct crystal shapes that are diagnostic of preexisting gypsum (Duda et al. 2015; Cui et al. 2016b). The $\delta^{34}S_{sulfate}$ value of this gypsum-bearing interval has been constrained to be ca. +40‰ based on carbonate associated sulfate (CAS) analysis (Cui 2015; Cui et al. 2016b), which is consistent with the $\delta^{34}S_{sulfate}$ constraints based on CAS analysis of coeval strata in Arctic Siberia (Cui et al. 2016a) and direct $\delta^{34}S_{sulfate}$ analyses of bedded anhydrite strata in Oman (Fike and Grotzinger 2008, 2010; Bergmann 2013). We propose that this could be the source of hydrothermal sulfate for the Datangpo TSR event.

Rayleigh distillation model for superheavy pyrite

To generate superheavy pyrite with $\delta^{34}S_{pyrite}$ as high as +70‰, it is required that the $\delta^{34}S_{sulfate}$ values of an equilibrated TSR solution be higher than +70‰. Figure 24 shows models of sulfide precipitation by batch precipitation in a closed system and by Rayleigh distillation. In these models, an initial $\delta^{34}S_{sulfate}$ value of +40‰ was adopted assuming that the sulfate source of this TSR fluid is the Ediacaran Dengying Formation in South China and an equilibrium value of $\Delta^{34}S_{sulfate\text{-}sulfide} = 40‰$. These calculations show that $\delta^{34}S_{sulfide}$ values above +70‰ can be generated after precipitation of 80% of sulfate in closed system fluids.

It needs to be noted that the above calculation represents a simplified scenario with a constant $\Delta^{34}S_{sulfate\text{-}sulfide}$ of 40‰. Published lab experiments suggest that the $\Delta^{34}S_{sulfate\text{-}sulfide}$ value at equilibrium is ~40‰ (Friedman and O'Neil 1977) or ~30‰ (Ohmoto and Lasaga 1982; Ohmoto 1986; Ohmoto and Goldhaber 1997; Seal 2006) at the temperature of ~200 °C. The $\Delta^{34}S_{sulfate\text{-}sulfide}$ value would be significantly higher at a lower temperature. It is possible that the hydrothermal fluid temperatures vary as TSR occurs. In geological conditions, the precipitation of superheavy pyrite can be a dynamic process with varying $\delta^{34}S_{sulfate}$, temperatures, $\Delta^{34}S_{sulfate\text{-}sulfide}$, and $\delta^{34}S_{pyrite}$ values. Regardless, our model demonstrates that $\delta^{34}S_{sulfate}$ and $\delta^{34}S_{sulfide}$ signals as high as +70‰ can be produced via TSR during the late stage of Rayleigh distillation. This process could occur when hydrothermal fluids flow along ancient faults, during which pyrite with a spectrum of $\delta^{34}S_{pyrite}$ values may have been produced via TSR.

IMPLICATIONS

Rethinking the Neoproterozoic sulfur cycle

The occurrence of the Neoproterozoic superheavy pyrite has led to the speculation of anomalously low sulfate concentrations in the ocean (Hayes et al. 1992; Hurtgen et al. 2002; Canfield 2004; Li et al. 2012; Wu et al. 2016). However, in light of the petrographic and isotopic results in this study, we argue that the studied superheavy pyrite formed in deeply buried sediments by hydrothermal fluids and therefore cannot be used to infer the marine sulfur cycles during deposition. Similar SEM-SIMS studies have not yet been published for other localities. It is possible that the sulfate concentration in the Cryogenian ocean may not be as low as the previous studies suggested.

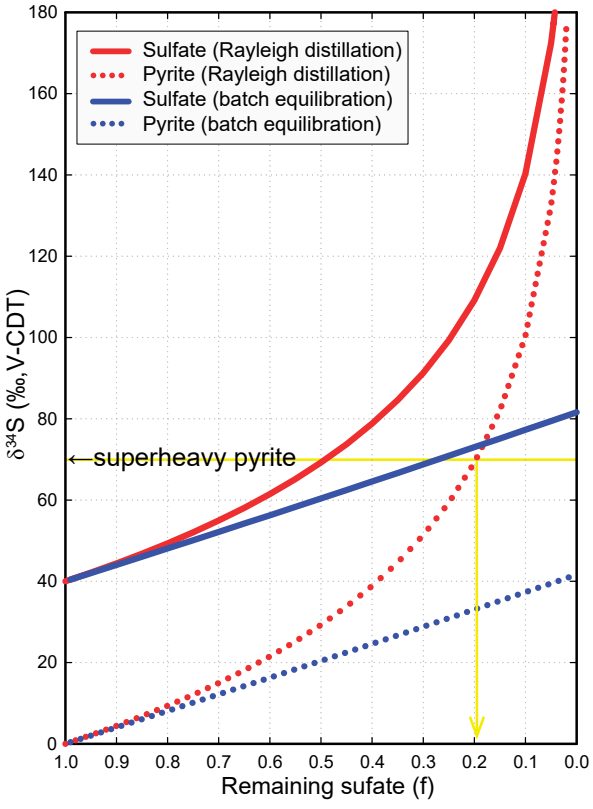

FIGURE 24. Models of $\delta^{34}S_{sulfate}$ and $\delta^{34}S_{sulfide}$ evolution during Rayleigh distillation (red) and batch equilibration (blue) for precipitation of pyrite from sulfate (initial $\delta^{34}S = 40‰$) in a system closed to externally derived fluids or other sources of sulfur. Equations used in calculation are from Canfield (2001a, 2001b). Yellow arrow shows the condition when $\delta^{34}S_{sulfide}$ value achieves +70‰. See the main text for detailed discussion.

Cryogenian superheavy pyrite has been reported from five post-Sturtian successions worldwide: the Datangpo Formation in South China; the Tapley Hill and Aralka formations in Australia; the Court Formation in Namibia; the Bonahaven Dolomite Formation in the U.K.; and the Arena Formation in East Greenland (Fig. 1). In light of our study of the Datangpo Formation in South China, similar investigations are suggested in other localities to assess the nature of the high-$\delta^{34}S$ signals. It needs to be noted that the current time-series $\delta^{34}S$ compilation (Canfield 2001a; Shen et al. 2001; Cui et al. 2016a, 2016b) is based on pyrite that has been regarded as early diagenetic in origin. TSR-derived superheavy pyrite can be much more abundant in geological record than the time-series $\delta^{34}S$ compilation shows.

The new data from South China suggest that at least some Neoproterozoic superheavy pyrite formed by late diagenetic alteration. If this observation applies to other localities, then an emerging question is, why is superheavy pyrite particularly notable in the Neoproterozoic interval? Here, we propose that three potential factors may have played a role in contributing to

the occurrence of the Neoproterozoic superheavy pyrite.

Increased diagenetic potential for TSR. Considering that bedded sulfate evaporites are increasingly deposited during and after the Neoproterozoic (Kah et al. 2004; Halverson and Hurtgen 2007; Kah and Bartley 2011; Cui et al. 2016b), it is likely that the considerable rise in seawater sulfate concentrations during the Neoproterozoic Oxygenation Event promoted evaporite deposition (Shields-Zhou and Och 2011; Och and Shields-Zhou 2012), which consequently enhanced the diagenetic potential for TSR during deep burial. When these evaporites are dissolved by hydrothermal fluids, TSR would occur if organic matter is also available in the host sedimentary strata.

High $\delta^{34}S_{sulfate}$ during the Neoproterozoic. It is notable that time-series $\delta^{34}S_{sulfate}$ values remain high during the Neoproterozoic and reach to the maximum (ca. +40‰) during the late Ediacaran Period (Fike and Grotzinger 2008; Halverson et al. 2009, 2010; Paytan and Gray 2012; Cui et al. 2016a, 2016b). The high $\delta^{34}S_{sulfate}$ signals of the Neoproterozoic seawater may have been recycled after deposition (e.g., post-depositional dissolution of gypsum), facilitating the genesis of superheavy pyrite in the host rocks during a post-depositional TSR event.

Increased tectonic activity. The breakup of the Rodinia supercontinent and progressive formation of the Gondwana supercontinent during the Neoproterozoic Era (Li 2011; Li et al. 2013) may have also played an active role in facilitating TSR in sedimentary strata. The process of continental reconfiguration may have enhanced the activity of hydrothermal fluids, and thus promoted TSR to occur in the Neoproterozoic.

We propose that the above factors may have played a role in facilitating TSR in the Neoproterozoic record in South China and possibly beyond. The Neoproterozoic superheavy pyrites in other localities are suggested to be examined in a similar way to better test the above hypotheses.

Diverse origins of framboidal pyrite

Framboidal pyrite in sedimentary records has been widely regarded as either formed in seawater or during diagenesis via MSR in low-temperature conditions. Framboids often start to grow in the water column, followed by early diagenetic overgrowth in shallow marine sediments (Raiswell 1982; Schallreuter 1984; Wilkin et al. 1996; Wilkin and Barnes 1997; Popa et al. 2004; Schieber 2011). Based on the pioneering work by Wilkin et al. (1996) and then followed by Bond and Wignall (2010), the size distribution of pyrite framboids has been widely used to infer the redox conditions of seawater during deposition. However, more complexities are revealed in the samples of this study showing that origin, texture, size, and isotopic values of framboidal pyrite can be diverse.

First, the size of pyrite framboids can be significantly affected by late-stage pyrite overgrowth. Pyrite framboids can be partially or completely masked by late-stage pyrite overgrowth (Figs. 6, 7, and 11–14), which cannot be detected without SEM imaging. Similar phenomena have also been reported from the Ediacaran samples (Wacey et al. 2015; Liu 2016) and pyrites in modern marine sediments (Lin et al. 2016b, 2017).

Second, both MSR- and TSR-derived framboidal pyrites have been found in the studied samples. These two types of framboid have distinct characteristics in petrography, paragenesis and $\delta^{34}S_{pyrite}$ spatial patterns at micrometer scale. The framboidal pyrite in diamictite Sample 1 shows heterogeneous $\delta^{34}S_{pyrite}$ values (Figs. 7, 22, and 23), and is interpreted to be syngenetic (in water column) or early diagenetic (in shallow marine sediments) in origin and formed by MSR. In contrast, the framboidal pyrite in Samples 2 and 4 records remarkably homogeneous and superheavy $\delta^{34}S_{pyrite}$ values in spite of heterogeneous textures (Figs. 14 and 19), which are interpreted to be formed via TSR by migrating hydrothermal fluids.

Supporting evidence for the existence of framboidal pyrite with a hydrothermal origin also comes from studies on both natural and synthetic pyrite framboids. Framboidal pyrites nucleated in hydrothermal veins or ores have been reported (Rust 1935; Love and Amstutz 1969; Ostwald and England 1979; Scott et al. 2009). Additionally, lab experiments have demonstrated that framboidal pyrite can be synthesized at temperatures as high as 350 °C within a few hours (Sunagawa et al. 1971; Graham and Ohmoto 1994; Ohfuji and Rickard 2005). These studies suggest that framboidal pyrite of a high-temperature origin is possible in both natural and lab environments.

Taken together, framboidal pyrite can be formed in both marine and hydrothermal (>100 °C) conditions. Observations by reflected light microscopy alone are insufficient to detect the origins of pyrite. Detailed SEM petrography and micrometer-scale $\delta^{34}S_{pyrite}$ analysis by SIMS are a powerful approach to interrogate the genesis of framboids.

Concluding remarks

(1) To interrogate the origins of the Neoproterozoic superheavy pyrite (Fig. 1), detailed petrographic and in situ $\delta^{34}S$ analyses (Figs. 3–21, Appendix[1] 2–6) were conducted using scanning electron microscopy and secondary ion mass spectrometry (SEM-SIMS) for pyrite in the Cryogenian Tiesi'ao and Datangpo formations at unprecedented spatial resolution (2 μm spot size). Distinct spatial patterns of $\delta^{34}S_{pyrite}$ values at micrometer scale are found to be correlated with pyrite morphology and genesis (Table 1; Figs. 22 and 23).

(2) Petrographic observations show that the Datangpo superheavy pyrite postdates the mineralization of rhodochrosite and illite (Figs. 9–13; Appendix[1] 3) and thus is late diagenetic in origin. This refutes the long-held belief that these framboids are syngenetic (in water column) or early diagenetic (in shallow marine sediments).

(3) Framboidal pyrites of both marine and hydrothermal origins were found in this study. Framboidal pyrite in the Tiesi'ao diamictite (Sample 1) shows heterogeneous (+11.2 to +28.3‰), relatively low (+16.4‰ in average) $\delta^{34}S_{pyrite}$ values and a relatively wide range of grain sizes (up to 30 μm in diameter) (Figs. 5–7; Appendix[1] 2). In contrast, the framboidal pyrite in Mn-rich carbonates (Sample 2) from the basal Datangpo Formation shows homogeneous (+56.3 to +60.4‰) and superheavy (+57.6‰ average) $\delta^{34}S_{pyrite}$ values and relatively small grain sizes (<7 μm diameter) (Figs. 11–14; Appendix[1] 3). Sample 1 is interpreted to be syngenetic or early diagenetic in origin and formed by microbial sulfate reduction (MSR), while Sample 2 is interpreted to be hydrothermal in origin and formed by thermochemical sulfate reduction (TSR) (Table 1). The use of the size distribution of framboidal pyrite to infer paleo-redox

conditions should be done with caution.

(4) Pyrite in one studied Datangpo shale sample from drill core (Sample 3) shows heterogeneous (+60.3 to +71.2‰) and superheavy (+66.3‰ average) $\delta^{34}S_{pyrite}$ values at micrometer scales (Figs. 16 and 17; Appendix[1] 4). It is notable that a decreasing $\delta^{34}S_{pyrite}$ trend is consistently recorded from the core to the edge of individual pyrite grains in Sample 3 (Figs. 16 and 17; Appendix[1] 4). This is in strong contrast with biogenic pyrite, which typically shows an increasing $\delta^{34}S_{pyrite}$ trend from the core to the edge of individual pyrite grains. It is proposed that the decreasing $\delta^{34}S_{pyrite}$ trend results from TSR with increasing sulfur isotope fractionations between sulfate and sulfide as hydrothermal fluids cool.

(5) Based on multiple lines of sedimentological and geochemical evidence at both basinal- and micrometer-scales, we argue that the superheavy pyrite in the Cryogenian strata in South China formed via thermochemical sulfate reduction (TSR), instead of microbial sulfate reduction (MSR). This is the first time that a post-depositional, hydrothermal origin is proposed for the superheavy pyrite in South China.

(6) We propose that post-depositional TSR plays an influential role in generating high $\delta^{34}S$ values. Consequently, interpretations of the high $\delta^{34}S$ values from the ancient geological record should reconsider the influence that similar post-depositional processes may have in generating superheavy pyrite associated with noteworthy biogeochemical events in the Earth's history. Our study demonstrates that the integrated SEM-SIMS approach to $\delta^{34}S_{pyrite}$ analysis of individual pyrite grains is an effective tool to assess the veracity of sedimentary pyrite in chemostratigraphic studies.

Acknowledgments

This paper is a contribution to the *American Mineralogist* Special Collection "Isotopes, Minerals, And Petrology: Honoring John Valley." The authors thank William Peck, Aaron Cavosie, and Jade Star Lackey for organizing this special collection of papers. The first author H.C. is a former Post-Doc (Jan 2016–May 2018) working with J.W.V. and expresses his gratitude to J.W.V. for mentorship, scholarship, passion, and support. This study could not have been made without the cohesive, inclusive, and positive atmosphere in the WiscSIMS and SEM labs, Department of Geoscience, University of Wisconsin–Madison.

This study is supported by the NASA Astrobiology Institute (NNA13AA94A). The WiscSIMS Lab is supported by NSF (EAR-1355590, EAR-1658823) and the University of Wisconsin–Madison. J.W.V. is also supported by NSF (EAR-1524336) and DOE (DE-FG02-93ER14389). The authors thank Bil Schneider, Tina Hill, and Phil Gopon for assistance in the SEM lab; Brian Hess, Noriko Kita, James Kern, Ian Orland, and Maciej Śliwiński for assistance in sample preparation and SIMS analysis; Huifang Xu for assistance in the microscope lab. We also thank Alan Jay Kaufman, Ganqing Jiang, Shuhai Xiao, Xianguo Lang, Kang-Jun Huang, and Maciej Śliwiński for helpful comments. This paper was improved by constructive reviews by David Fike and an anonymous reviewer. We thank Keith Putirka (editor) and Aaron Cavosie (associate editor) for handling this manuscript.

Contributions

H.C. designed research; F.Z. provided samples; H.C. and K.K. performed SIMS analysis at J.W.V.'s WiscSIMS lab; H.C. and J.H.F. performed SEM and EPMA analyses; H.C. interpreted the data with contributions from all coauthors. H.C. wrote the manuscript with significant input from J.W.V. All authors contributed to discussion and manuscript revision.

References cited

Alonso-Azcarate, R., Bottrell, R., and Velasco, M. (1999) Pathways and distances of fluid flow during low-grade metamorphism: evidence from pyrite deposits of the Cameros Basin, Spain. Journal of Metamorphic Geology, 17, 339–348. https://doi.org/10.1046/j.1525-1314.1999.00202.x

Armstrong, J.T. (1988) Quantitative analysis of silicate and oxide minerals: comparison of Monte Carlo, ZAF and phi-rho-z procedures. Microbeam Analysis, 23, 239–246.

Basuki, N.I., Taylor, B.E., and Spooner, E.T.C. (2008) Sulfur isotope evidence for thermochemical reduction of dissolved sulfate in Mississippi valley-type zinc-lead mineralization, Bongara area, northern Peru. Economic Geology, 103, 783–799. https://doi.org/10.2113/gsecongeo.103.4.783.

Bergmann, K.D. (2013) Constraints on the carbon cycle and climate during the early evolution of animals, 398 p. Ph.D. dissertation, California Institute of Technology, Pasadena.

Berner, R.A. (1984) Sedimentary pyrite formation: An update. Geochimica et Cosmochimica Acta, 48, 605–615. https://doi.org/10.1016/0016-7037(84)90089-9.

——— (1989) Biogeochemical cycles of carbon and sulfur and their effect on atmospheric oxygen over phanerozoic time. Palaeogeography, Palaeoclimatology, Palaeoecology, 75, 97–122. https://doi.org/10.1016/0031-0182(89)90186-7.

Biehl, B.C., Reuning, L., Schoenherr, J., Lüders, V., and Kukla, P.A. (2016) Impacts of hydrothermal dolomitization and thermochemical sulfate reduction on secondary porosity creation in deeply buried carbonates: A case study from the Lower Saxony Basin, northwest Germany. AAPG Bulletin, 100, 597–621. https://doi.org/10.1306/01141615055.

Bond, D.P.G., and Wignall, P.B. (2010) Pyrite framboid study of marine Permian–Triassic boundary sections: A complex anoxic event and its relationship to contemporaneous mass extinction. Geological Society of America Bulletin, 122, 1265–1279. https://doi.org/10.1130/b30042.1.

Borowski, W.S., Hoehler, T.M., Alperin, M.J., Rodriguez, N.M., and Paull, C.K. (2000) Significance of anaerobic methane oxidation in methane-rich sediments overlying the Blake Ridge gas hydrates. In C.K. Paull, R. Matsumoto, P.J. Wallace, and W.P. Dillon, Eds., Proceedings of the Ocean Drilling Program, Scientific Results, 164, 87–99.

Böttcher, M.E. (2011) Sulfur isotopes. In J. Reitner and V. Thiel, Eds., Encyclopedia of Geobiology, 864–866. Springer Netherlands.

Böttcher, M.E., Smock, A.M., and Cypionka, H. (1998) Sulfur isotope fractionation during experimental precipitation of iron(II) and manganese(II) sulfide at room temperature. Chemical Geology, 146, 127–134. https://doi.org/10.1016/S0009-2541(98)00004-7.

Bowles, M.W., Mogollón, J.M., Kasten, S., Zabel, M., and Hinrichs, K.-U. (2014) Global rates of marine sulfate reduction and implications for sub–sea-floor metabolic activities. Science, 344, 889–891. https://doi.org/10.1126/science.1249213.

Bradley, A.S., Leavitt, W.D., Schmidt, M., Knoll, A.H., Girguis, P.R., and Johnston, D.T. (2016) Patterns of sulfur isotope fractionation during microbial sulfate reduction. Geobiology, 14, 91–101. https://doi.org/10.1111/gbi.12149.

Cai, C., Hu, W., and Worden, R.H. (2001) Thermochemical sulphate reduction in Cambro–Ordovician carbonates in Central Tarim. Marine and Petroleum Geology, 18, 729–741. https://doi.org/10.1016/S0264-8172(01)00028-9.

Cai, C., Worden, R.H., Bottrell, S.H., Wang, L., and Yang, C. (2003) Thermochemical sulphate reduction and the generation of hydrogen sulphide and thiols (mercaptans) in Triassic carbonate reservoirs from the Sichuan Basin, China. Chemical Geology, 202, 39–57. https://doi.org/10.1016/S0009-2541(03)00209-2.

Cai, C., Xie, Z., Worden, R.H., Hu, G., Wang, L., and He, H. (2004) Methane-dominated thermochemical sulphate reduction in the Triassic Feixianguan Formation East Sichuan Basin, China: towards prediction of fatal H_2S concentrations. Marine and Petroleum Geology, 21, 1265–1279. https://doi.org/10.1016/j.marpetgeo.2004.09.003.

Cai, Y., Hua, H., Xiao, S., Schiffbauer, J.D., and Li, P. (2010) Biostratinomy of the late Ediacaran pyritized Gaojiashan Lagerstätte from southern Shaanxi, South China: Importance of event deposits. PALAIOS, 25, 487–506. https://doi.org/10.2110/palo.2009.p09-133r.

Cai, C., Hu, G., Li, H., Jiang, L., He, W., Zhang, B., Jia, L., and Wang, T. (2015) Origins and fates of H_2S in the Cambrian and Ordovician in Tazhong area: Evidence from sulfur isotopes, fluid inclusions and production data. Marine and Petroleum Geology, 67, 408–418. https://doi.org/10.1016/j.marpetgeo.2015.05.007.

Calver, C.R., Crowley, J.L., Wingate, M.T.D., Evans, D.A.D., Raub, T.D., and Schmitz, M.D. (2013) Globally synchronous Marinoan deglaciation indicated by U-Pb geochronology of the Cottons Breccia, Tasmania, Australia. Geology, 41, 1127–1130. https://doi.org/10.1130/g34568.1.

Canfield, D.E. (2001a) Biogeochemistry of sulfur isotopes. Reviews in Mineralogy and Geochemistry, 43, 607–636.

——— (2001b) Isotope fractionation by natural populations of sulfate-reducing bacteria. Geochimica et Cosmochimica Acta, 65, 1117–1124. https://doi.org/10.1016/S0016-7037(00)00584-6.

——— (2004) The evolution of the Earth surface sulfur reservoir. American Journal of Science, 304, 839–861. https://doi.org/10.2475/ajs.304.10.839.

Canfield, D.E., and Farquhar, J. (2012) The Global Sulfur Cycle. In A.H. Knoll, D.E. Canfield, and K.O. Konhauser, Eds., Fundamentals of Geobiology, p. 49–64. Wiley.

Canfield, D.E., and Teske, A. (1996) Late Proterozoic rise in atmospheric oxygen concentration inferred from phylogenetic and sulphur-isotope studies. Nature, 382, 127–132. https://doi.org/10.1038/382127a0.

Canfield, D.E., and Thamdrup, B. (1994) The production of ^{34}S-depleted sulfide during bacterial disproportionation of elemental sulfur. Science, 266, 1973–1975. https://doi.org/10.1126/science.11540246.

Canfield, D.E., Farquhar, J., and Zerkle, A.L. (2010) High isotope fractionations during sulfate reduction in a low-sulfate euxinic ocean analog. Geology, 38, 415–418. https://doi.org/10.1130/g30723.1.

Cao, H., Kaufman, A.J., Shan, X., Cui, H., and Zhang, G. (2016) Sulfur isotope constraints on marine transgression in the lacustrine Upper Cretaceous Songliao Basin,

northeastern China. Palaeogeography, Palaeoclimatology, Palaeoecology, 451, 152–163. https://doi.org/10.1016/j.palaeo.2016.02.041.
Chambers, L.A., Trudinger, P.A., Smith, J.W., and Burns, M.S. (1975) Fractionation of sulfur isotopes by continuous cultures of *Desulfovibrio desulfuricans*. Canadian Journal of Microbiology, 21, 1602–1607. https://doi.org/10.1139/m75-234.
Chen, D., and Chen, X. (1992) Geological and geochemical characteristics of Songtan hydrothermal sedimentary manganese deposits, Guizhou. Acta Sedimentologica Sinica, 10, 35–43 (in Chinese with English abstract).
Chen, X., Li, D., Ling, H.-F., and Jiang, S.-Y. (2008) Carbon and sulfur isotopic compositions of basal Datangpo Formation, northeastern Guizhou, South China: Implications for depositional environment. Progress in Natural Science, 18, 421–429. https://doi.org/10.1016/j.pnsc.2007.10.008.
Chen, Z., Zhou, C., Meyer, M., Xiang, K., Schiffbauer, J.D., Yuan, X., and Xiao, S. (2013) Trace fossil evidence for Ediacaran bilaterian animals with complex behaviors. Precambrian Research, 224, 690–701. https://doi.org/10.1016/j.precamres.2012.11.004.
Chen, Z., Zhou, C., Xiao, S., Wang, W., Guan, C., Hua, H., and Yuan, X. (2014) New Ediacara fossils preserved in marine limestone and their ecological implications. Scientific Reports, 4, 4180. https://doi.org/10.1038/srep04180.
Chen, D., Zhou, X., Fu, Y., Wang, J., and Yan, D. (2015) New U–Pb zircon ages of the Ediacaran–Cambrian boundary strata in South China. Terra Nova, 27, 62–68. https://doi.org/10.1111/ter.12134.
Chu, X., Li, R., and Ohmoto, H. (1998) Sulfur isotope geochemistry of the late Proterozoic in Southern China. Chinese Science Bulletin, 43, Supplement 1, 27–27. https://doi.org/10.1007/bf02891401.
Chu, X., Li, R., Zhang, T., and Zhang, Q. (2001) Implication of ultra-high $\delta^{34}S$ values of pyrite in manganese mineralization beds of Datangpo stage. Bulletin of Mineralogy, Petrology and Geochemistry, 20, 320–322 (in Chinese with English abstract).
Chu, X., Zhang, Q., Zhang, T., and Feng, L. (2003) Sulfur and carbon isotopic variations in Neoproterozoic sedimentary rocks from southern China. Progress in Natural Science, 13, 875–880. https://doi.org/10.1080/10020070312331344580.
Claypool, G.E. (2004) Ventilation of marine sediments indicated by depth profiles of pore water sulfate and $\delta^{34}S$. In R.J. Hill, J. Leventhal, Z. Aizenshtat, M.J. Baedecker, G. Claypool, R. Eganhouse, M. Goldhaber, and K. Peters, Eds., The Geochemical Society Special Publications, 9, 59–65. Elsevier.
Condon, D., Zhu, M., Bowring, S., Wang, W., Yang, A., and Jin, Y. (2005) U–Pb ages from the Neoproterozoic Doushantuo Formation, China. Science, 308, 95–98. https://doi.org/10.1126/science.1107765.
Cooke, D.R., Bull, S.W., Large, R.R., and McGoldrick, P.J. (2000) The importance of oxidized brines for the formation of Australian Proterozoic stratiform sediment-hosted Pb-Zn (Sedex) deposits. Economic Geology, 95, 1–18. https://doi.org/10.2113/gsecongeo.95.1.1.
Crowe, S.A., Paris, G., Katsev, S., Jones, C., Kim, S.-T., Zerkle, A.L., Nomosatryo, S., Fowle, D.A., Adkins, J.F., and Sessions, A.L. (2014) Sulfate was a trace constituent of Archean seawater. Science, 346, 735–739. https://doi.org/10.1126/science.1258966.
Cui, H. (2015) Authigenesis, biomineralization, and carbon–sulfur cycling in the Ediacaran Ocean, 181 p. Ph.D. dissertation, University of Maryland, College Park, Maryland.
Cui, H., Grazhdankin, D.V., Xiao, S., Peek, S., Rogov, V.I., Bykova, N.V., Sievers, N.E., Liu, X.-M., and Kaufman, A.J. (2016a) Redox-dependent distribution of early macro-organisms: Evidence from the terminal Ediacaran Khatyspyt Formation in Arctic Siberia. Palaeogeography, Palaeoclimatology, Palaeoecology, 461, 122–139. https://doi.org/10.1016/j.palaeo.2016.08.015.
Cui, H., Kaufman, A.J., Xiao, S., Peek, S., Cao, H., Min, X., Cai, Y., Siegel, Z., Liu, X.M., Peng, Y., Schiffbauer, J.D., and Martin, A.J. (2016b) Environmental context for the terminal Ediacaran biomineralization of animals. Geobiology, 14, 344–363. https://doi.org/10.1111/gbi.12178.
Cui, H., Kaufman, A.J., Xiao, S., Zhou, C., and Liu, X.-M. (2017) Was the Ediacaran Shuram Excursion a globally synchronized early diagenetic event? Insights from methane-derived authigenic carbonates in the uppermost Doushantuo Formation, South China. Chemical Geology, 450, 59–80. https://doi.org/10.1016/j.chemgeo.2016.12.010.
Cui, H., Kitajima, K., Spicuzza, M.J., Fournelle, J.H., Ishida, A., Brown, P.E., and Valley, J.W. (2018) Searching for the Great Oxidation Event in North America: A reappraisal of the Huronian Supergroup by SIMS sulfur four-isotope analysis. Astrobiology, 18, 519–538. https://doi.org/10.1089/ast.2017.1722
Ding, T., Valkiers, S., Kipphardt, H., De Bièvre, P., Taylor, P.D.P., Gonfiantini, R., and Krouse, R. (2001) Calibrated sulfur isotope abundance ratios of three IAEA sulfur isotope reference materials and V-CDT with a reassessment of the atomic weight of sulfur. Geochimica et Cosmochimica Acta, 65, 2433–2437. https://doi.org/10.1016/S0016-7037(01)00611-1.
Donovan, J.J., Kremser, D., Fournelle, J., and Goemann, K. (2018) Probe for Windows User's Guide and Reference, Enterprise Edition. Probe Software, Inc., Eugene, Oregon.
Drake, H., Astrom, M.E., Heim, C., Broman, C., Astrom, J., Whitehouse, M., Ivarsson, M., Siljestrom, S., and Sjovall, P. (2015) Extreme ^{13}C depletion of carbonates formed during oxidation of biogenic methane in fractured granite. Nature Communications, 6, 7020. https://doi.org/10.1038/ncomms8020.
Drake, H., Heim, C., Roberts, N.M.W., Zack, T., Tillberg, M., Broman, C., Ivarsson, M., Whitehouse, M.J., and Åström, M.E. (2017) Isotopic evidence for microbial production and consumption of methane in the upper continental crust throughout the Phanerozoic eon. Earth and Planetary Science Letters, 470, 108–118. https://doi.org/10.1016/j.epsl.2017.04.034.
Duda, J.-P., Zhu, M., and Reitner, J. (2015) Depositional dynamics of a bituminous carbonate facies in a tectonically induced intra-platform basin: the Shibantan Member (Dengying Formation, Ediacaran Period). Carbonates and Evaporites, 31, 87–99. https://doi.org/10.1007/s13146-015-0243-8.
Eldridge, C.S., Walshe, J.L., Compston, W., Williams, I.S., Both, R.A., and Ohmoto, H. (1989) Sulfur isotope variability in sediment-hosted massive sulfide deposits as determined using the ion microprobe SHRIMP: I. An example from the Rammelsberg orebody—A reply. Economic Geology, 84, 453–457. https://doi.org/10.2113/gsecongeo.84.2.453.
Feng, L., Chu, X., Huang, J., Zhang, Q., and Chang, H. (2010) Reconstruction of paleoredox conditions and early sulfur cycling during deposition of the Cryogenian Datangpo Formation in South China. Gondwana Research, 18, 632–637. https://doi.org/10.1016/j.gr.2010.02.011.
Ferrini, V., Fayek, M., De Vito, C., Mignardi, S., and Pignatti, J. (2010) Extreme sulphur isotope fractionation in the deep Cretaceous biosphere. Journal of the Geological Society, 167, 1009–1018. https://doi.org/10.1144/0016-76492009-161.
Fike, D.A., Bradley, A.S., and Rose, C.V. (2015) Rethinking the ancient sulfur cycle. Annual Review of Earth and Planetary Sciences, 43, 593–622. https://doi.org/10.1146/annurev-earth-060313-054802.
Fike, D.A., and Grotzinger, J.P. (2008) A paired sulfate–pyrite $\delta^{34}S$ approach to understanding the evolution of the Ediacaran–Cambrian sulfur cycle. Geochimica et Cosmochimica Acta, 72, 2636–2648. https://doi.org/10.1016/j.gca.2008.03.021.
——— (2010) A $\delta^{34}S_{SO4}$ approach to reconstructing biogenic pyrite burial in carbonate–evaporite basins: An example from the Ara Group, Sultanate of Oman. Geology, 38, 371–374. https://doi.org/10.1130/g30230.1.
Fike, D.A., Grotzinger, J.P., Pratt, L.M., and Summons, R.E. (2006) Oxidation of the Ediacaran ocean. Nature, 444, 744–747. https://doi.org/10.1038/nature05345.
Fischer, W.W., Fike, D.A., Johnson, J.E., Raub, T.D., Guan, Y., Kirschvink, J.L., and Eiler, J.M. (2014) SQUID–SIMS is a useful approach to uncover primary signals in the Archean sulfur cycle. Proceedings of the National Academy of Sciences, 111, 5468–5473. https://doi.org/10.1073/pnas.1322577111.
Friedman, I., and O'Neil, J.R. (1977) Data of geochemistry: Compilation of stable isotope fractionation factors of geochemical interest. Geological Survey Professional Paper 440, Chapter KK, p. KK1–KK12.
Fu, Y., van Berk, W., and Schulz, H.-M. (2016) Hydrogen sulfide formation, fate, and behavior in anhydrite-sealed carbonate gas reservoirs: A three-dimensional reactive mass transport modeling approach. AAPG Bulletin, 100, 843–865. https://doi.org/10.1306/12111514206.
Gadd, M.G., Layton-Matthews, D., Peter, J.M., Paradis, S., and Jonasson, I.R. (2017) The world-class Howard's Pass SEDEX Zn-Pb district, Selwyn Basin, Yukon. Part II: the roles of thermochemical and bacterial sulfate reduction in metal fixation. Mineralium Deposita, 52, 405–419. https://doi.org/10.1007/s00126-016-0672-x.
Ghazban, F., Schwarcz, H.P., and Ford, D.C. (1990) Carbon and sulfur isotope evidence for in situ reduction of sulfate, Nanisivik lead-zinc deposits, Northwest Territories, Baffin Island, Canada. Economic Geology, 85, 360–375. https://doi.org/10.2113/gsecongeo.85.2.360.
Goldhaber, M., and Kaplan, I. (1975) Controls and consequences of sulfate reduction rates in recent marine sediments. Soil Science, 119, 42–55.
———(1980) Mechanisms of sulfur incorporation and isotope fractionation during early diagenesis in sediments of the Gulf of California. Marine Chemistry, 9, 95–143. https://doi.org/10.1016/0304-4203(80)90063-8.
Goldstein, T.P., and Aizenshtat, Z. (1994) Thermochemical sulfate reduction: A review. Journal of Thermal Analysis, 42, 241–290. https://doi.org/10.1007/bf02547004.
Gomes, M.L., and Hurtgen, M.T. (2015) Sulfur isotope fractionation in modern euxinic systems: Implications for paleoenvironmental reconstructions of paired sulfate–sulfide isotope records. Geochimica et Cosmochimica Acta, 157, 39–55. https://doi.org/10.1016/j.gca.2015.02.031.
Gomes, M.L., Fike, D.A., Bergmann, K.D., Jones, C., and Knoll, A.H. (2018) Environmental insights from high-resolution (SIMS) sulfur isotope analyses of sulfides in Proterozoic microbialites with diverse mat textures. Geobiology, 16, 17–34. https://doi.org/10.1111/gbi.12265.
Gorjan, P., Veevers, J.J., and Walter, M.R. (2000) Neoproterozoic sulfur-isotope variation in Australia and global implications. Precambrian Research, 100, 151–179. https://doi.org/10.1016/s0301-9268(99)00073-x.
Gorjan, P., Walter, M.R., and Swart, R. (2003) Global Neoproterozoic (Sturtian) postglacial sulfide-sulfur isotope anomaly recognised in Namibia. Journal of African Earth Sciences, 36, 89–98. https://doi.org/10.1016/S0899-5362(03)00002-2.
Graham, U., and Ohmoto, H. (1994) Experimental study of formation mechanisms of hydrothermal pyrite. Geochimica et Cosmochimica Acta, 58, 2187–2202. https://doi.org/10.1016/0016-7037(94)90004-3.
Habicht, K.S., Gade, M., Thamdrup, B., Berg, P., and Canfield, D.E. (2002) Calibration of sulfate levels in the Archean ocean. Science, 298, 2372–2374. https://doi.org/10.1126/science.1078265.
Halverson, G.P., and Hurtgen, M.T. (2007) Ediacaran growth of the marine sulfate reservoir. Earth and Planetary Science Letters, 263, 32–44. https://doi.org/10.1016/j.epsl.2007.08.022.
Halverson, G.P., and Shields-Zhou, G. (2011) Chemostratigraphy and the Neoprotero-

zoic glaciations. In E. Arnaud, G.P. Halverson, and G. Shields-Zhou, Eds. The Geological Record of Neoproterozoic Glaciations. Geological Society, London, Memoirs, 36, 51–66.
Halverson, G.P., Hurtgen, M.T., Porter, S.M., and Collins, A.S. (2009) Neoproterozoic–Cambrian biogeochemical evolution. Neoproterozoic-Cambrian Tectonics, Global Change and Evolution: A Focus on Southwestern Gondwana. Developments in Precambrian Geology, 16, 351–365. https://doi.org/10.1016/s0166-2635(09)01625-9.
Halverson, G.P., Wade, B.P., Hurtgen, M.T., and Barovich, K.M. (2010) Neoproterozoic chemostratigraphy. Precambrian Research, 182, 337–350. https://doi.org/10.1016/j.precamres.2010.04.007.
Hao, F., Guo, T., Zhu, Y., Cai, X., Zou, H., and Li, P. (2008) Evidence for multiple stages of oil cracking and thermochemical sulfate reduction in the Puguang gas field, Sichuan Basin, China. AAPG Bulletin, 92, 611–637.
Harrison, A., and Thode, H. (1958) Mechanism of the bacterial reduction of sulfate from isotope fractionation studies. Transactions of the Royal Faraday Society, 54, 84–92. https://doi.org/10.1039/tf9585400084.
Hayes, J.M., Lambert, I.B., and Strauss, H. (1992) The sulfur-isotopic record. In J.W. Schopf and C. Klein, Eds., The Proterozoic Biosphere: A Multidisciplinary Study, p. 129–132. Cambridge University Press.
He, Z., Yang, R., Gao, J., Cheng, W., and Wen, G. (2013a) The structure character of manganese ore deposit of Datangpo-period of Neoproterozoic in Songtao of Guizhou. China's Manganese Industry, 31, 5–16 (in Chinese with English abstract).
He, Z., Yang, R., Gao, J., Cheng, W., Zhang, R., and Zhang, P. (2013b) Sedimentary geochemical characteristics of manganese deposits in Xixibao, Songtao County, Guizhou Province. Geochimica, 42, 576–588 (in Chinese with English abstract).
Heydari, E., and Moore, C.H. (1989) Burial diagenesis and thermochemical sulfate reduction, Smackover Formation, southeastern Mississippi salt basin. Geology, 17, 1080–1084.
Hoffman, P.F., and Li, Z.-X. (2009) A palaeogeographic context for Neoproterozoic glaciation. Palaeogeography, Palaeoclimatology, Palaeoecology, 277, 158–172. https://doi.org/10.1016/j.palaeo.2009.03.013.
Hoffman, P.F., and Schrag, D.P. (2002) The snowball Earth hypothesis: testing the limits of global change. Terra Nova, 14, 129–155. https://doi.org/10.1046/j.1365-3121.2002.00408.x.
Hoffman, P.F., Kaufman, A.J., Halverson, G.P., and Schrag, D.P. (1998) A Neoproterozoic Snowball Earth. Science, 281, 1342–1346. https://doi.org/10.1126/science.281.5381.1342.
Hoffman, P.F., Abbot, D.S., Ashkenazy, Y., Benn, D.I., Brocks, J.J., Cohen, P.A., Cox, G.M., Creveling, J.R., Donnadieu, Y., Erwin, D.H., and others. (2017) Snowball Earth climate dynamics and Cryogenian geology–geobiology. Science Advances, 3, e1600983. https://doi.org/10.1126/sciadv.1600983.
Hurtgen, M.T., Arthur, M.A., Suits, N.S., and Kaufman, A.J. (2002) The sulfur isotopic composition of Neoproterozoic seawater sulfate: implications for a snowball Earth? Earth and Planetary Science Letters, 203, 413–429. https://doi.org/10.1016/s0012-821x(02)00804-x.
Hurtgen, M.T., Arthur, M.A., and Halverson, G.P. (2005) Neoproterozoic sulfur isotopes, the evolution of microbial sulfur species, and the burial efficiency of sulfide as sedimentary pyrite. Geology, 33, 41–44. https://doi.org/10.1130/g20923.1.
Jia, L., Cai, C., Yang, H., Li, H., Wang, T., Zhang, B., Jiang, L., and Tao, X. (2015) Thermochemical and bacterial sulfate reduction in the Cambrian and Lower Ordovician carbonates in the Tazhong Area, Tarim Basin, NW China: evidence from fluid inclusions, C, S, and Sr isotopic data. Geofluids, 15, 421–437. https://doi.org/10.1111/gfl.12105.
Jiang, G., Sohl, L.E., and Christie-Blick, N. (2003) Neoproterozoic stratigraphic comparison of the Lesser Himalaya (India) and Yangtze block (south China): Paleogeographic implications. Geology, 31, 917–920. https://doi.org/10.1130/g19790.1.
Jiang, G., Kaufman, A.J., Christie-Blick, N., Zhang, S., and Wu, H. (2007) Carbon isotope variability across the Ediacaran Yangtze platform in South China: Implications for a large surface-to-deep ocean $\delta^{13}C$ gradient. Earth and Planetary Science Letters, 261, 303–320. https://doi.org/10.1016/j.epsl.2007.07.009.
Jiang, G., Shi, X., Zhang, S., Wang, Y., and Xiao, S. (2011) Stratigraphy and paleogeography of the Ediacaran Doushantuo Formation (ca. 635–551 Ma) in South China. Gondwana Research, 19, 831–849. https://doi.org/10.1016/j.gr.2011.01.006.
Jiang, L., Worden, R.H., and Cai, C.F. (2014) Thermochemical sulfate reduction and fluid evolution of the Lower Triassic Feixianguan Formation sour gas reservoirs, northeast Sichuan Basin, China. AAPG Bulletin, 98, 947–973. https://doi.org/10.1306/10171312220.
Jiang, L., Worden, R.H., and Cai, C. (2015) Generation of isotopically and compositionally distinct water during thermochemical sulfate reduction (TSR) in carbonate reservoirs: Triassic Feixianguan Formation, Sichuan Basin, China. Geochimica et Cosmochimica Acta, 165, 249–262. https://doi.org/10.1016/j.gca.2015.05.033.
Jiang, L., Worden, R.H., and Yang, C. (2018) Thermochemical sulphate reduction can improve carbonate petroleum reservoir quality. Geochimica et Cosmochimica Acta, 223, 127–140. https://doi.org/10.1016/j.gca.2017.11.032.
Johnson, J.E., Webb, S.M., Thomas, K., Ono, S., Kirschvink, J.L., and Fischer, W.W. (2013) Manganese-oxidizing photosynthesis before the rise of cyanobacteria. Proceedings of the National Academy of Sciences, 110, 11238–11243. https://doi.org/10.1073/pnas.1305530110.
Johnston, D.T., Wing, B.A., Farquhar, J., Kaufman, A.J., Strauss, H., Lyons, T.W., Kah, L.C., and Canfield, D.E. (2005) Active microbial sulfur disproportionation in the Mesoproterozoic. Science, 310, 1477–1479. https://doi.org/10.1126/science.1117824.
Jones, D., Hartley, J., Frisch, G., Purnell, M., and Darras, L. (2012) Non-destructive, safe removal of conductive metal coatings from fossils: a new solution. Palaeontologia Electronica, 15, 4T.
Jørgensen, B.B., and Kasten, S. (2006) Sulfur cycling and methane oxidation. In H.D. Schulz and M. Zabel, Eds., Marine Geochemistry, p. 271–309. Springer-Verlag.
Jørgensen, B.B., Isaksen, M.F., and Jannasch, H.W. (1992) Bacterial sulfate reduction above 100 °C in deep-sea hydrothermal vent sediments. Science, 258, 1756–1757. https://doi.org/10.1126/science.258.5089.1756.
Jørgensen, B.B., Böttcher, M.E., Lüschen, H., Neretin, L.N., and Volkov, I.I. (2004) Anaerobic methane oxidation and a deep H_2S sink generate isotopically heavy sulfides in Black Sea sediments 1. Geochimica et Cosmochimica Acta, 68, 2095–2118. https://doi.org/10.1016/j.gca.2003.07.017.
Kah, L.C., and Bartley, J.K. (2011) Protracted oxygenation of the Proterozoic biosphere. International Geology Review, 53, 1424–1442. https://doi.org/10.1080/00206814.2010.527651.
Kah, L.C., Lyons, T.W., and Frank, T.D. (2004) Low marine sulphate and protracted oxygenation of the Proterozoic biosphere. Nature, 431, 834–838. https://doi.org/10.1038/nature02974.
Kaplan, I.R., and Rafter, T.A. (1958) Fractionation of stable isotopes of sulfur by Thiobacilli. Science, 127, 517–518. https://doi.org/10.1126/science.127.3297.517.
Kaplan, I.R., and Rittenberg, S.C. (1964) Microbiological fractionation of sulphur isotopes. Microbiology, 34, 195–212. https://doi.org/10.1099/00221287-34-2-195.
Kelley, K.D., Dumoulin, J.A., and Jennings, S. (2004a) The Anarraaq Zn-Pb-Ag and Barite Deposit, Northern Alaska: Evidence for Replacement of Carbonate by Barite and Sulfides. Economic Geology, 99, 1577–1591. https://doi.org/10.2113/gsecongeo.99.7.1577.
Kelley, K.D., Leach, D.L., Johnson, C.A., Clark, J.L., Fayek, M., Slack, J.F., Anderson, V.M., Ayuso, R.A., and Ridley, W.I. (2004b) Textural, compositional, and sulfur isotope variations of sulfide minerals in the Red Dog Zn-Pb-Ag deposits, Brooks Range, Alaska: Implications for ore formation. Economic Geology, 99, 1509–1532. https://doi.org/10.2113/gsecongeo.99.7.1509.
King, H.E., Walters, C.C., Horn, W.C., Zimmer, M., Heines, M.M., Lamberti, W.A., Kliewer, C., Pottorf, R.J., and Macleod, G. (2014) Sulfur isotope analysis of bitumen and pyrite associated with thermal sulfate reduction in reservoir carbonates at the Big Piney–La Barge production complex. Geochimica et Cosmochimica Acta, 134, 210–220. https://doi.org/10.1016/j.gca.2013.11.005.
Kirschvink, J.L. (1992) Late Proterozoic low-latitude global glaciation: the Snowball Earth. In J.W. Schopf, C. Klein, and D. Des Maris, Eds., The Proterozoic Biosphere: A Multidisciplinary Study, 51–52. Cambridge University Press.
Kiyosu, Y. (1980) Chemical reduction and sulfur-isotope effects of sulfate by organic matter under hydrothermal conditions. Chemical Geology, 30, 47–56. https://doi.org/10.1016/0009-2541(80)90115-1.
Kiyosu, Y., and Krouse, H.R. (1990) The role of organic acid in the abiogenic reduction of sulfate and the sulfur isotope effect. Geochemical Journal, 24, 21–27. https://doi.org/10.2343/geochemj.24.21.
Kohn, M.J., Riciputi, L.R., Stakes, D., and Orange, D.L. (1998) Sulfur isotope variability in biogenic pyrite: Reflections of heterogeneous bacterial colonization? American Mineralogist, 83, 1454–1468. https://doi.org/10.2138/am-1997-11-1234.
Krouse, H.R., Viau, C.A., Eliuk, L.S., Ueda, A., and Halas, S. (1988) Chemical and isotopic evidence of thermochemical sulphate reduction by light hydrocarbon gases in deep carbonate reservoirs. Nature, 333, 415–419. https://doi.org/10.1038/333415a0.
Kunzmann, M., Bui, T.H., Crockford, P.W., Halverson, G.P., Scott, C., Lyons, T.W., and Wing, B.A. (2017) Bacterial sulfur disproportionation constrains timing of Neoproterozoic oxygenation. Geology, 45, 207–210. https://doi.org/10.1130/g38602.1.
Lan, Z., Li, X.-H., Zhang, Q., and Li, Q.-L. (2015a) Global synchronous initiation of the 2nd episode of Sturtian glaciation: SIMS zircon U–Pb and O isotope evidence from the Jiangkou Group, South China. Precambrian Research, 267, 28–38. https://doi.org/10.1016/j.precamres.2015.06.002.
Lan, Z., Li, X.-H., Zhu, M., Zhang, Q., and Li, Q.-L. (2015b) Revisiting the Liantuo Formation in Yangtze Block, South China: SIMS U–Pb zircon age constraints and regional and global significance. Precambrian Research, 263, 123–141. https://doi.org/10.1016/j.precamres.2015.03.012.
Lang, X. (2016) The Process of Nanhua Glaciation and the Synglacial Evolution of Marine Geochemistry in the South China Block, China. Ph.D. dissertation (in Chinese with English abstract), Peking University, Beijing, China, 108 p.
Lang, X., Shen, B., Peng, Y., Zhou, C., and Huang, K. (2016) A new pathway of sulfur cycling in the Cryogenian Ocean. Geological Society of America Abstracts with Programs, vol. 48, no. 7, p. 48, Denver, Colorado.
Leavitt, W.D. (2014) On the mechanisms of sulfur isotope fractionation during microbial sulfate reduction, 242 p. Ph.D. dissertation, Harvard University, Cambridge, Massachusetts.
Leavitt, W.D., Bradley, A.S., Halevy, I., and Johnston, D.T. (2013) Influence of sulfate reduction rates on the Phanerozoic sulfur isotope record. Proceedings of the National Academy of Sciences, 110, 11244–11249. https://doi.org/10.1073/pnas.1218874110.
Li, Z.-X. (2011) Breakup of Rodinia. In J. Reitner and V. Thiel, Eds., Encyclopedia of Geobiology, p. 206–210. Springer.
Li, R., Zhang, S., Lei, J., Shen, Y., Chen, J., and Chu, X. (1996) Temporal and spacial variation in $\delta^{34}S$ values of pyrite from Sinian strata discussion on relationship be-

tween Yangtze Block and the late Proterozoic supercontinent. Scientia Geologica Sinica, 31, 209–217 (in Chinese with English abstract).
Li, R., Chen, J., Zhang, S., Lei, J., Shen, Y., and Chen, X. (1999a) Spatial and temporal variations in carbon and sulfur isotopic compositions of Sinian sedimentary rocks in the Yangtze platform, South China. Precambrian Research, 97, 59–75. https://doi.org/10.1016/s0301-9268(99)00022-4.
Li, Z., Li, X., Kinny, P., and Wang, J. (1999b) The breakup of Rodinia: did it start with a mantle plume beneath South China? Earth and Planetary Science Letters, 173, 171–181. https://doi.org/10.1016/S0012-821X(99)00240-X.
Li, C., Love, G.D., Lyons, T.W., Scott, C.T., Feng, L., Huang, J., Chang, H., Zhang, Q., and Chu, X. (2012) Evidence for a redox stratified Cryogenian marine basin, Datangpo Formation, South China. Earth and Planetary Science Letters, 331–332, 246–256. https://doi.org/10.1016/j.epsl.2012.03.018.
Li, Z.-X., Evans, D.A.D., and Halverson, G.P. (2013) Neoproterozoic glaciations in a revised global palaeogeography from the breakup of Rodinia to the assembly of Gondwanaland. Sedimentary Geology, 294, 219–232. https://doi.org/10.1016/j.sedgeo.2013.05.016.
Lin, Q., Wang, J., Algeo, T.J., Sun, F., and Lin, R. (2016a) Enhanced framboidal pyrite formation related to anaerobic oxidation of methane in the sulfate-methane transition zone of the northern South China Sea. Marine Geology, 379, 100–108. https://doi.org/10.1016/j.margeo.2016.05.016.
Lin, Z., Sun, X., Peckmann, J., Lu, Y., Xu, L., Strauss, H., Zhou, H., Gong, J., Lu, H., and Teichert, B.M.A. (2016b) How sulfate-driven anaerobic oxidation of methane affects the sulfur isotopic composition of pyrite: A SIMS study from the South China Sea. Chemical Geology, 440, 26–41. https://doi.org/10.1016/j.chemgeo.2016.07.007.
Lin, Z., Sun, X., Lu, Y., Strauss, H., Xu, L., Gong, J., Teichert, B.M.A., Lu, R., Lu, H., Sun, W., and Peckmann, J. (2017) The enrichment of heavy iron isotopes in authigenic pyrite as a possible indicator of sulfate-driven anaerobic oxidation of methane: Insights from the South China Sea. Chemical Geology, 449, 15–29. https://doi.org/10.1016/j.chemgeo.2016.11.032.
Liu, A.G. (2016) Framboidal pyrite shroud confirms the 'death mask' model for moldic preservation of Ediacaran soft-bodied organisms. Palaios, 31, 259–274. https://doi.org/10.2110/palo.2015.095.
Liu, T.-B., Maynard, J.B., and Alten, J. (2006) Superheavy S isotopes from glacier-associated sediments of the Neoproterozoic of south China: Oceanic anoxia or sulfate limitation? Geological Society of America Memoirs, 198, 205–222. https://doi.org/10.1130/2006.1198(12).
Liu, Q., Zhu, D., Jin, Z., Liu, C., Zhang, D., and He, Z. (2016) Coupled alteration of hydrothermal fluids and thermal sulfate reduction (TSR) in ancient dolomite reservoirs—An example from Sinian Dengying Formation in Sichuan Basin, southern China. Precambrian Research, 285, 39–57. https://doi.org/10.1016/j.precamres.2016.09.006.
Logan, G.A., Hayes, J., Hieshima, G.B., and Summons, R.E. (1995) Terminal Proterozoic reorganization of biogeochemical cycles. Nature, 376, 53–56. https://doi.org/10.1038/376053a0.
Love, L., and Amstutz, G. (1969) Framboidal pyrite in two andesites. Neues Jahrbuch für Mineralogie Monatshefte, 3, 97–108.
Lu, M., Zhu, M., Zhang, J., Shields-Zhou, G., Li, G., Zhao, F., Zhao, X., and Zhao, M. (2013) The DOUNCE event at the top of the Ediacaran Doushantuo Formation, South China: Broad stratigraphic occurrence and non-diagenetic origin. Precambrian Research, 225, 86–109. https://doi.org/10.1016/j.precamres.2011.10.018.
Machel, H.-G. (1987) Saddle dolomite as a by-product of chemical compaction and thermochemical sulfate reduction. Geology, 15, 936–940.
——— (2001) Bacterial and thermochemical sulfate reduction in diagenetic settings—old and new insights. Sedimentary Geology, 140, 143–175. https://doi.org/10.1016/s0037-0738(00)00176-7.
Machel, H.G., and Buschkuehle, B.E. (2008) Diagenesis of the Devonian Southesk-Cairn Carbonate Complex, Alberta, Canada: marine cementation, burial dolomitization, thermochemical sulfate reduction, anhydritization, and squeegee fluid flow. Journal of Sedimentary Research, 78, 366–389. https://doi.org/10.2110/jsr.2008.037.
Machel, H.G., Krouse, H.R., and Sassen, R. (1995) Products and distinguishing criteria of bacterial and thermochemical sulfate reduction. Applied Geochemistry, 10, 373–389. https://doi.org/10.1016/0883-2927(95)00008-8.
Machel, H.G., Riciputi, L.R., and Cole, D.R. (1997) Ion microprobe investigation of diagenetic carbonates and sulfides in the Devonian Nisku Formation, Alberta, Canada. In I.P. Montañez, J.M. Gregg, and K.L. Shelton, Eds., Basin-Wide Diagenetic Patterns: Integrated Petrologic, Geochemical and Hydrologic Considerations, SEPM Special Publication 57. Society for Sedimentary Geology.
Marin-Carbonne, J., Remusat, L., Sforna, M.C., Thomazo, C., Cartigny, P., and Philippot, P. (2018) Sulfur isotope's signal of nanopyrites enclosed in 2.7 Ga stromatolitic organic remains reveal microbial sulfate reduction. Geobiology, 16, 121–138. https://doi.org/10.1111/gbi.12275
Marini, L., Moretti, R., and Accornero, M. (2011) Sulfur isotopes in magmatic-hydrothermal systems, melts, and magmas. Reviews in Mineralogy and Geochemistry, 73, 423–492.
McFadden, K.A., Huang, J., Chu, X., Jiang, G., Kaufman, A.J., Zhou, C., Yuan, X., and Xiao, S. (2008) Pulsed oxidation and biological evolution in the Ediacaran Doushantuo Formation. Proceedings of the National Academy of Sciences, 105, 3197–3202. https://doi.org/10.1073/pnas.0708336105.
McKibben, M.A., and Riciputi, L.R. (1998) Sulfur isotopes by ion microprobe. In M.A. McKibben, W.C. Shanks III, and W.I. Ridley, Eds., Applications of Microanalytical Techniques to Understanding Mineralizing Processes. Reviews in Economic Geology, vol. 7, p. 121–139. Society of Economic Geologists, Littleton, Colorado.
McLoughlin, N., Grosch, E.G., Kilburn, M.R., and Wacey, D. (2012) Sulfur isotope evidence for a Paleoarchean subseafloor biosphere, Barberton, South Africa. Geology, 40, 1031–1034. https://doi.org/10.1130/g33313.1.
Meyer, N.R., Zerkle, A.L., and Fike, D.A. (2017) Sulphur cycling in a Neoarchaean microbial mat. Geobiology, 15, 353–365. https://doi.org/10.1111/gbi.12227.
Narbonne, G.M., Xiao, S., Shields, G.A., and Gehling, J.G. (2012) The Ediacaran Period. In F.M. Gradstein, J.G. Ogg, M.D. Schmitz, and G.M. Ogg, Eds., The Geologic Time Scale, p. 413–435. Elsevier.
Och, L.M., and Shields-Zhou, G.A. (2012) The Neoproterozoic oxygenation event: Environmental perturbations and biogeochemical cycling. Earth-Science Reviews, 110, 26–57. https://doi.org/10.1016/j.earscirev.2011.09.004.
Oduro, H., Harms, B., Sintim, H.O., Kaufman, A.J., Cody, G., and Farquhar, J. (2011) Evidence of magnetic isotope effects during thermochemical sulfate reduction. Proceedings of the National Academy of Sciences, 108, 17635–17638. https://doi.org/10.1073/pnas.1108112108.
Ohfuji, H., and Rickard, D. (2005) Experimental syntheses of framboids—a review. Earth-Science Reviews, 71, 147–170. https://doi.org/10.1016/j.earscirev.2005.02.001.
Ohmoto, H. (1986) Stable isotope geochemistry of ore deposits. Reviews in Mineralogy, 16, 491–559.
Ohmoto, H., and Goldhaber, M.B. (1997) Sulfur and carbon isotopes. In H.L. Barnes, Ed., Geochemistry of Hydrothermal Ore Deposits, 3rd ed., p. 517–611. Wiley.
Ohmoto, H., and Lasaga, A.C. (1982) Kinetics of reactions between aqueous sulfates and sulfides in hydrothermal systems. Geochimica et Cosmochimica Acta, 46, 1727–1745. https://doi.org/10.1016/0016-7037(82)90113-2.
Ohmoto, H., Watanabe, Y., Lasaga, A.C., Naraoka, H., Johnson, I., Brainard, J., and Chorney, A. (2014) Oxygen, iron, and sulfur geochemical cycles on early Earth: Paradigms and contradictions. Geological Society of America Special Papers, 504, 55–95.
Olanipekun, B.J., and Azmy, K. (2018) In situ geochemical characterization of pyrite crystals in burial dolomites of St. George Group carbonates. Canadian Journal of Earth Sciences, in press. https://doi.org/10.1139/cjes-2016-0152.
Orr, W.L. (1974) Changes in sulfur content and isotopic ratios of sulfur during petroleum maturation—Study of Big Horn Basin paleozoic oils. AAPG Bulletin, 58, 2295–2318.
——— (1977) Geologic and geochemical controls on the distribution of hydrogen sulfide in natural gas. In R. Campos, and J. Goni, Eds., Advances in Organic Geochemistry, Proceedings, 1975, 50, 571–597. Pergamon.
Ostwald, J., and England, B.M. (1979) The relationship between euhedral and framboidal pyrite in base-metal sulphide ores. Mineralogical Magazine, 43, 297–300.
Pan, W., Zhuo, X., Chen, X., Yang, S., and Zhao, S. (2016) Geochemical characteristics of manganese bearing rock series in black shale basins of Northest Guizhou, China. Acta Sedimentologica Sinica, 34, 868–880 (in Chinese with English abstract). https://doi.org/10.14027/j.cnki.cjxb.2016.05.006.
Parnell, J., and Boyce, A.J. (2017) Microbial sulphate reduction during Neoproterozoic glaciation, Port Askaig Formation, UK. Journal of the Geological Society, 174, 850–854. https://doi.org/10.1144/jgs2016-147.
Pasquier, V., Sansjofre, P., Rabineau, M., Revillon, S., Houghton, J., and Fike, D.A. (2017) Pyrite sulfur isotopes reveal glacial-interglacial environmental changes. Proceedings of the National Academy of Sciences, 114, 5941–5945. https://doi.org/10.1073/pnas.1618245114.
Paytan, A., and Gray, E.T. (2012) Sulfur isotope stratigraphy. In F.M. Gradstein, J.G. Ogg, M.D. Schmitz, and G.M. Ogg, Eds., The Geologic Time Scale, chapter 9, p. 167–180. Elsevier.
Peevler, J., Fayek, M., Misra, K.C., and Riciputi, L.R. (2003) Sulfur isotope microanalysis of sphalerite by SIMS: constraints on the genesis of Mississippi valley-type mineralization, from the Mascot-Jefferson City district, East Tennessee. Journal of Geochemical Exploration, 80, 277–296. https://doi.org/10.1016/s0375-6742(03)00195-x.
Peng, X., Guo, Z., Chen, S., Sun, Z., Xu, H., Ta, K., Zhang, J., Zhang, L., Li, J., and Du, M. (2017) Formation of carbonate pipes in the northern Okinawa Trough linked to strong sulfate exhaustion and iron supply. Geochimica et Cosmochimica Acta, 205, 1–13. https://doi.org/10.1016/j.gca.2017.02.010.
Peterson, K.J., Lyons, J.B., Nowak, K.S., Takacs, C.M., Wargo, M.J., and McPeek, M.A. (2004) Estimating metazoan divergence times with a molecular clock. Proceedings of the National Academy of Sciences, 101, 6536–6541. https://doi.org/10.1073/pnas.0401670101.
Popa, R., Kinkle, B.K., and Badescu, A. (2004) Pyrite framboids as biomarkers for iron-sulfur systems. Geomicrobiology Journal, 21, 193–206. https://doi.org/10.1080/01490450490275497.
Powell, T.G., and Macqueen, R.W. (1984) Precipitation of sulfide ores and organic matter: sulfate reactions at Pine Point, Canada. Science, 224, 63–67. https://doi.org/10.1126/science.224.4644.63.
Qin, Y., An, Z., Wang, J., and Li, D. (2013) The discovery and geological characteristics of the super-large sized Daotuo manganese deposit in Songtao, Guizhou. Mineral Exploration, 345–355 (in Chinese with English abstract).
Raiswell, R. (1982) Pyrite texture, isotopic composition and the availability of

iron. American Journal of Science, 282, 1244–1263. https://doi.org/10.2475/ajs.282.8.1244.
Randell, R.N., and Anderson, G.M. (1996) Geology of the Polaris Zn-Pb deposit and surrounding area, Canadian Arctic Archipelago. In D.F. Sangster, Ed., Carbonate-Hosted Lead-Zinc Deposits, vol. 4, p. 307–319. 75th Anniversary, Society of Economic Geology, Special Publication.
Riciputi, L.R., Cole, D.R., and Machel, H.G. (1996) Sulfide formation in reservoir carbonates of the Devonian Nisku Formation, Alberta, Canada: An ion microprobe study. Geochimica et Cosmochimica Acta, 60, 325–336. https://doi.org/10.1016/0016-7037(96)83133-4.
Ries, J.B., Fike, D.A., Pratt, L.M., Lyons, T.W., and Grotzinger, J.P. (2009) Superheavy pyrite ($\delta^{34}S_{pyr} > \delta^{34}S_{CAS}$) in the terminal Proterozoic Nama Group, southern Namibia: A consequence of low seawater sulfate at the dawn of animal life. Geology, 37, 743–746. https://doi.org/10.1130/g25775a.1.
Rooney, A.D., Strauss, J.V., Brandon, A.D., and Macdonald, F.A. (2015) A Cryogenian chronology: Two long-lasting synchronous Neoproterozoic glaciations. Geology, 43, 459–462. https://doi.org/10.1130/g36511.1.
Runnegar, B. (1982) A molecular-clock date for the origin of the animal phyla. Lethaia, 15, 199–205. https://doi.org/10.1111/j.1502-3931.1982.tb00645.x.
Rust, G.W. (1935) Colloidal primary copper ores at Cornwall mines, southeastern Missouri. The Journal of Geology, 43, 398–426. https://doi.org/10.1086/624318.
Rye, R.O., and Ohmoto, H. (1974) Sulfur and carbon isotopes and ore genesis: A review. Economic Geology, 69, 826–842. https://doi.org/10.2113/gsecongeo.69.6.826.
Schallreuter, R. (1984) Framboidal pyrite in deep-sea sediments. In W.W. Hay and J.-C. Sibuet, Eds., Initial Reports of the Deep Sea Drilling Project, 75, p. 875–891. U.S. Government Printing Office.
Scheller, E.L., Dickson, A.J., Canfield, D.E., Korte, C., Kristiansen, K.K., and Dahl, T.W. (2018) Ocean redox conditions between the Snowballs—geochemical constraints from Arena Formation, East Greenland. Precambrian Research, in press. https://doi.org/10.1016/j.precamres.2017.12.009.
Schieber, J. (2011) Iron sulfide formation. In J. Reitner and V. Thiel, Eds., Encyclopedia of Geobiology, p. 486–502. Springer.
Schmitz, M.D. (2012) Radiometric ages used in GTS2012. In F.M. Gradstein, J.G. Ogg, M.D. Schmitz, and G.M. Ogg, Eds., The Geologic Time Scale, p. 1045–1082. Elsevier.
Scott, R.J., Meffre, S., Woodhead, J., Gilbert, S.E., Berry, R.F., and Emsbo, P. (2009) Development of framboidal pyrite during diagenesis, low-grade regional metamorphism, and hydrothermal alteration. Economic Geology, 104, 1143–1168. https://doi.org/10.2113/gsecongeo.104.8.1143.
Seal, R.R. (2006) Sulfur isotope geochemistry of sulfide minerals. Reviews in Mineralogy and Geochemistry, 61, 633–677.
Shen, Y., Buick, R., and Canfield, D.E. (2001) Isotopic evidence for microbial sulphate reduction in the early Archaean era. Nature, 410, 77–81. https://doi.org/10.1038/35065071.
Shields-Zhou, G., and Och, L. (2011) The case for a Neoproterozoic Oxygenation Event: Geochemical evidence and biological consequences. GSA Today, 21, 4–11. https://doi.org/10.1130/gsatg102a.1.
Shields-Zhou, G.A., Hill, A.C., and Macgabhann, B.A. (2012) The Cryogenian Period. In F.M. Gradstein, J.G. Ogg, M.D. Schmitz, and G.M. Ogg, Eds., The Geologic Time Scale, p. 393–411. Elsevier.
Siegmund, H., and Erdtmann, B.-D. (1994) Facies and diagenesis of some Upper Proterozoic dolomites of South China. Facies, 31, 255–263. https://doi.org/10.1007/bf02536942.
Sim, M.S., Bosak, T., and Ono, S. (2011a) Large sulfur isotope fractionation does not require disproportionation. Science, 333, 74–77. https://doi.org/10.1126/science.1205103.
Sim, M.S., Ono, S., Donovan, K., Templer, S.P., and Bosak, T. (2011b) Effect of electron donors on the fractionation of sulfur isotopes by a marine Desulfovibrio sp. Geochimica et Cosmochimica Acta, 75, 4244–4259. https://doi.org/10.1016/j.gca.2011.05.021.
Sim, M.S., Ono, S., and Bosak, T. (2012) Effects of iron and nitrogen limitation on sulfur isotope fractionation during microbial sulfate reduction. Applied and Environmental Microbiology, 78, 8368–8376. https://doi.org/10.1128/AEM.01842-12.
Song, G., Wang, X., Shi, X., and Jiang, G. (2017) New U-Pb age constraints on the upper Banxi Group and synchrony of the Sturtian glaciation in South China. Geoscience Frontiers, 8, 1161–1173. https://doi.org/10.1016/j.gsf.2016.11.012.
Soœnicka, M., and Lüders, V. (2018) Super-deep, TSR-controlled Phanerozoic MVT type Zn-Pb deposits hosted by Zechstein reservoir carbonate, Lower Saxony Basin, Germany. Chemical Geology, in press. https://doi.org/10.1016/j.chemgeo.2018.04.025.
Sunagawa, I., Endo, Y., and Nakai, N. (1971) Hydrothermal synthesis of framboidal pyrite. Society of Mining Geologists of Japan, Special Issue, Proceedings of the IMA-IAGOD meetings '70, Joint Symposium, 1, 10–14.
Tang, S. (1990) Isotope geological study of manganese deposit in Minle area, Hunan Province. Acta Sedimentologica Sinica, 8, 77–84 (in Chinese with English abstract).
Tang, S., and Liu, T. (1999) Origin of the early Sinian Minle manganese deposit, Hunan Province, China. Ore Geology Reviews, 15, 71–78. https://doi.org/10.1016/S0169-1368(99)00015-3.
Tompkins, L.A., Rayner, M.J., Groves, D.I., and Roche, M.T. (1994) Evaporites: In situ sulfur source for rhythmically banded ore in the Cadjebut Mississippi Valley-type Zn-Pb deposit, Western Australia. Economic Geology, 89, 467–492. https://doi.org/10.2113/gsecongeo.89.3.467.
Ushikubo, T., Williford, K.H., Farquhar, J., Johnston, D.T., Van Kranendonk, M.J., and Valley, J.W. (2014) Development of in situ sulfur four-isotope analysis with multiple Faraday cup detectors by SIMS and application to pyrite grains in a Paleoproterozoic glaciogenic sandstone. Chemical Geology, 383, 86–99. https://doi.org/10.1016/j.chemgeo.2014.06.006.
Valley, J.W., and Kita, N.T. (2009) In situ oxygen isotope geochemistry by ion microprobe. In M. Fayek, Ed., Secondary Ion Mass Spectrometry in the Earth Sciences—Gleaning the Big Picture from a Small Spot, 41, p. 19–63. Mineralogical Association of Canada Short Course 41.
Wacey, D., McLoughlin, N., Whitehouse, M.J., and Kilburn, M.R. (2010) Two coexisting sulfur metabolisms in a ca. 3400 Ma sandstone. Geology, 38, 1115–1118. https://doi.org/10.1130/g31329.1.
Wacey, D., Kilburn, M.R., Saunders, M., Cliff, J.B., Kong, C., Liu, A.G., Matthews, J.J., and Brasier, M.D. (2015) Uncovering framboidal pyrite biogenicity using nano-scale CN_{org} mapping. Geology, 43, 27–30. https://doi.org/10.1130/g36048.1.
Walter, M.R., Veevers, J.J., Calver, C.R., Gorjan, P., and Hill, A.C. (2000) Dating the 840–544 Ma Neoproterozoic interval by isotopes of strontium, carbon, and sulfur in seawater, and some interpretative models. Precambrian Research, 100, 371–433. https://doi.org/10.1016/s0301-9268(99)00082-0.
Wang, J., and Li, Z.-X. (2003) History of Neoproterozoic rift basins in South China: implications for Rodinia break-up. Precambrian Research, 122, 141–158. https://doi.org/10.1016/s0301-9268(02)00209-7.
Wang, Y., Wang, L., and Zhu, S. (1985) The Stratigraphy, Sedimentary Environment and Manganese-Forming Process of the Datangpo Formation in Eastern Guizhou, 92 p. People's Publishing House of Guizhou, Guiyang (in Chinese).
Wang, L., Liu, C., and Zhang, H. (2013) Tectonic and sedimentary settings of evaporites in the Dengying Formation, South China Block: Implications for the potential of potash formation. Acta Geoscientica Sinica, 34, 585–593 (in Chinese with English abstract).
Wang, P., Zhou, Q., Du, Y., Yu, W., Xu, Y., Qi, L., and Yuan, L. (2016) Characteristics of pyrite sulfur isotope of Mn deposit from datangpo formation in Songtao area, East Guizhou Province and its geological significance. Earth Science—Journal of China University of Geosciences, 41, 2031–2040 (in Chinese with English abstract). https://doi.org/10.3799/dqkx.2016.142.
Wang, P., Du, Y., Algeo, T.J., Yu, W., Zhou, Q., Xu, Y., and Yuan, L. (2017) Post-sturtian sulfur isotope anomalies in the Nanhua Basin, South China related to upward H_2S Migration. Geological Society of America Abstracts with Programs, vol. 49, no. 6.
Watanabe, Y., Farquhar, J., and Ohmoto, H. (2009) Anomalous fractionations of sulfur isotopes during thermochemical sulfate reduction. Science, 324, 370–373. https://doi.org/10.1126/science.1169289.
Wilkin, R., and Barnes, H. (1997) Formation processes of framboidal pyrite. Geochimica et Cosmochimica Acta, 61, 323–339. https://doi.org/10.1016/s0016-7037(96)00320-1.
Wilkin, R.T., Barnes, H.L., and Brantley, S.L. (1996) The size distribution of framboidal pyrite in modern sediments: An indicator of redox conditions. Geochimica et Cosmochimica Acta, 60, 3897–3912. https://doi.org/10.1016/0016-7037(96)00209-8.
Williford, K.H., Van Kranendonk, M.J., Ushikubo, T., Kozdon, R., and Valley, J.W. (2011) Constraining atmospheric oxygen and seawater sulfate concentrations during Paleoproterozoic glaciation: In situ sulfur three-isotope microanalysis of pyrite from the Turee Creek Group, Western Australia. Geochimica et Cosmochimica Acta, 75, 5686–5705. https://doi.org/10.1016/j.gca.2011.07.010.
Williford, K.H., Ushikubo, T., Lepot, K., Kitajima, K., Hallmann, C., Spicuzza, M.J., Kozdon, R., Eigenbrode, J.L., Summons, R.E., and Valley, J.W. (2016) Carbon and sulfur isotopic signatures of ancient life and environment at the microbial scale: Neoarchean shales and carbonates. Geobiology, 14, 105–128. https://doi.org/10.1111/gbi.12163.
Wing, B.A., and Halevy, I. (2014) Intracellular metabolite levels shape sulfur isotope fractionation during microbial sulfate respiration. Proceedings of the National Academy of Sciences, 111, 18116–18125. https://doi.org/10.1073/pnas.1407502111.
Worden, R.H., and Smalley, P.C. (1996) H_2S-producing reactions in deep carbonate gas reservoirs: Khuff Formation, Abu Dhabi. Chemical Geology, 133, 157–171. https://doi.org/10.1016/S0009-2541(96)00074-5.
Worden, R.H., Smalley, P.C., and Oxtoby, N.H. (1995) Gas souring by thermochemical sulfate reduction at 140 °C. AAPG Bulletin, 79, 854–863.
Worden, R.H., Smalley, P.C., and Cross, M.M. (2000) The influence of rock fabric and mineralogy on thermochemical sulfate reduction: Khuff Formation, Abu Dhabi. Journal of Sedimentary Research, 70, 1210–1221. https://doi.org/10.1306/110499701210.
Wortmann, U.G., Bernasconi, S.M., and Böttcher, M.E. (2001) Hypersulfidic deep biosphere indicates extreme sulfur isotope fractionation during single-step microbial sulfate reduction. Geology, 29, 647–650.
Wu, C., Cheng, Y., Zhang, Z., Xiao, J., Fu, Y., Shao, S., Zheng, C., and Yao, J. (2015a) Geological implications of ultra-high $\delta^{34}S$ values of pyrite in manganese deposits of Nanhua Period in eastern Guizhou and adjacent areas, China. Geochimica, 44, 213–224 (in Chinese with English abstract).
Wu, N., Farquhar, J., and Fike, D.A. (2015b) Ediacaran sulfur cycle: Insights from sulfur isotope measurements ($\Delta^{33}S$ and $\delta^{34}S$) on paired sulfate–pyrite in the Huqf Supergroup of Oman. Geochimica et Cosmochimica Acta, 164, 352–364. https://doi.org/10.1016/j.gca.2015.05.031.

Wu, C., Zhang, Z., Xiao, J., Fu, Y., Shao, S., Zheng, C., Yao, J., and Xiao, C. (2016) Nanhuan manganese deposits within restricted basins of the southeastern Yangtze Platform, China: Constraints from geological and geochemical evidence. Ore Geology Reviews, 75, 76–99. https://doi.org/10.1016/j.oregeorev.2015.12.003.

Xi, X. (1987) Characteristic and Environments of Sinian Evaporite in Southern Sichuan, China. In T.M. Peryt, Ed., Lecture Notes in Earth Sciences: Evaporite Basins, 23–29. Springer-Verlag Berlin Heidelberg, Berlin.

Xiao, S. (2014) Oxygen and early animal evolution. In H.D. Holland and K.K. Turekian, Eds., Treatise on Geochemistry (2nd ed.), vol. 6, The Atmosphere—History, p. 231–250. Elsevier.

Xiao, S., Zhou, C., and Zhu, M. (2014) International Symposium and Field Workshop on Ediacaran and Cryogenian Stratigraphy. Episodes, 37, 218–221.

Xiao, S., Narbonne, G.M., Zhou, C., Laflamme, M., Grazhdankin, D.V., Moczydłowska-Vidal, M., and Cui, H. (2016) Toward an Ediacaran time scale: Problems, protocols, and prospects. Episodes, 39, 540–555. https://doi.org/10.18814/epiiugs/2016/v39i4/103886.

Xie, Q.-L., Chen, D.-F., and Chen, X.-P. (1999) Characteristics of sedimentary organic matter in Songtao manganese deposits, Guizhou. Acta Sedimentologica Sinica, 17, 280–284 (in Chinese with English abstract).

Xie, X.-F., Qin, Y., Wen, G.-G., and Xie, X.-Y. (2014) Relation between Datangpo Formation and manganese mineralization in Songtao manganese mining area of Tongren in Guizhou. Guizhou Geology, 31, 32–37 (in Chinese with English abstract).

Xu, X., Huang, H., and Liu, B. (1990) Manganese deposits of the Proterozoic Datangpo Formation, South China: genesis and palaeogeography. In J. Parnell, L. Ye, and C. Chen, Eds., Sediment-Hosted Mineral Deposits, 11, p. 39–50. The International Association of Sedimcntologists, Blackwell, Oxford, U.K.

Yang, R., Ouyang, Z., Zhu, L., Wang, S., Jiang, L., Zhang, W., and Gao, H. (2002) A new understanding of manganese carbonate deposits in early Sinian Datangpo Stage. Acta Mineralogica Sinica, 22, 329–334 (in Chinese with English abstract).

Yin, C., Wang, Y., Tang, F., Wan, Y., Wang, Z., Gao, L., Xing, Y., and Liu, P. (2006) SHRIMP II U-Pb zircon date from the Nanhuan Datangpo Formation in Songtao County, Guizhou Province. Acta Geologica Sinica, 80, 273–278 (in Chinese with English abstract).

Yu, W., Algeo, T.J., Du, Y., Zhou, Q., Wang, P., Xu, Y., Yuan, L., and Pan, W. (2017) Newly discovered Sturtian cap carbonate in the Nanhua Basin, South China. Precambrian Research, 293, 112–130. https://doi.org/10.1016/j.precamres.2017.03.011.

Yuan, Y.-S., Ma, Y.-S., Hu, S.-B., Guo, T.-L., and Fu, X.-Y. (2006) Present-day geothermal characteristics in South China. Chinese Journal of Geophysics, 49, 1005–1014. https://doi.org/10.1002/cjg2.922.

Zhang, F. (2014) The formation mechanism of Datangpo Manganese Ore Deposits during Nanhua Period in South China and the paleo-redox conditions of Nanhua Marine Basin. Master's thesis (in Chinese with English abstract), Chinese Academy of Geological Sciences, Beijing, 121 p.

Zhang, S., Jiang, G., and Han, Y. (2008) The age of the Nantuo Formation and Nantuo glaciation in South China. Terra Nova, 20, 289–294. https://doi.org/10.1111/j.1365-3121.2008.00819.x.

Zhang, F., Zhu, X., Gao, Z., Cheng, L., Peng, Q., and Yang, D. (2013) Implications of the precipitation mode of manganese and ultra-high $\delta^{34}S$ values of pyrite in Mn-carbonate of Xixibao Mn ore deposit in Northeastern Guizhou Province. Geological Review, 59, 274–286 (in Chinese with English abstract).

Zhang, M., Konishi, H., Xu, H., Sun, X., Lu, H., Wu, D., and Wu, N. (2014) Morphology and formation mechanism of pyrite induced by the anaerobic oxidation of methane from the continental slope of the NE South China Sea. Journal of Asian Earth Sciences, 92, 293–301. https://doi.org/10.1016/j.jseaes.2014.05.004.

Zhou, C., Tucker, R., Xiao, S., Peng, Z., Yuan, X., and Chen, Z. (2004) New constraints on the ages of Neoproterozoic glaciations in south China. Geology, 32, 437–440. https://doi.org/10.1130/g20286.1.

Zhou, Q., Du, Y.-S., Wang, J.-S., and Peng, J.-Q. (2007) Characteristics and significance of the cold seep carbonates from the Datangpo Formation of the Nanhua series in the northeast Guizhou. Earth Science—Journal of China University of Geosciences, 32, 339–346 (in Chinese with English abstract). https://doi.org/10.3321/j.issn:1000-2383.2007.03.006.

Zhou, Q., Du, Y., and Qin, Y. (2013) Ancient natural gas seepage sedimentary-type manganese metallogenic system and ore-forming model: A case study of Datangpo type manganese deposits formed in rift basin of Nanhua Period along Guizhou-Hunan-Chongqing border area. Mineral Deposits, 32, 457–466 (in Chinese with English abstract). https://doi.org/10.16111/j.0258-7106.2013.03.001.

Zhu, G., Zhang, S., Liang, Y., and Li, Q. (2007a) The genesis of H_2S in the Weiyuan Gas Field, Sichuan Basin and its evidence. Chinese Science Bulletin, 52, 1394–1404. https://doi.org/10.1007/s11434-007-0185-1.

Zhu, G., Zhao, W., Zhang, S., Liang, Y., and Wang, Z. (2007b) Discussion of gas enrichment mechanism and natural gas origin in marine sedimentary basin, China. Chinese Science Bulletin, 52, 62–76. https://doi.org/10.1007/s11434-007-6016-6.

Zhu, X., Peng, Q., Zhang, R., An, Z., Zhang, F., Yan, B., Li, J., Gao, Z., Tan, Y., and Pan, W. (2013) Geological and geochemical characteristics of the Daotuo super-large manganese ore deposit at Songtao County in Guizhou Province. Acta Geologica Sinica, 87, 1335–1348 (in Chinese with English abstract).

Zhu, G., Wang, T., Xie, Z., Xie, B., and Liu, K. (2015) Giant gas discovery in the Precambrian deeply buried reservoirs in the Sichuan Basin, China: Implications for gas exploration in old cratonic basins. Precambrian Research, 262, 45–66. https://doi.org/10.1016/j.precamres.2015.02.023.

Wu, C., Zhang, Z., Xiao, J., Fu, Y., Shao, S., Zheng, C., Yao, J., Xiao, C., 2016. Nanhuan manganese deposits within restricted basins of the southeastern Yangtze Platform, China: Constraints from geological and geochemical evidence. Ore Geology Reviews, 75, 76–99. http://doi.org/10.1016/j.oregeorev.2015.12.003.

Manuscript received January 31, 2018
Manuscript accepted May 16, 2018
Manuscript handled by Aaron Cavosie

Endnote:

[1]Deposit item AM-18-96489, Supplemental Material. Deposit items are free to all readers and found on the MSA web site, via the specific issue's Table of Contents (go to http://www.minsocam.org/MSA/AmMin/TOC/2018/Sep2018_data/Sep2018_data.html).